

LOCALIZED CO₂ CORROSION IN HORIZONTAL WET GAS FLOW

A dissertation presented to
the faculty of the
Fritz J. and Dolores H. Russ
College of Engineering and Technology
Ohio University

In partial fulfillment
of the requirements for the degree
Doctor of Philosophy

Yuhua Sun

June 2003

This dissertation entitled

LOCALIZED CO₂ CORROSION IN HORIZONTAL WET GAS FLOW

BY

YUHUA SUN

has been approved for

the Department of Chemical Engineering

and the Russ College of Engineering and Technology by

Srdjan Nesic

Professor of Chemical Engineering

Dennis Irwin

Dean, Russ College of Engineering and Technology

SUN, YUHUA. Ph.D. June 2003. Chemical Engineering

Localized CO₂ Corrosion in Horizontal Wet Gas Flow (178pp.)

Director of Dissertation: Srdjan Nesic

This study investigates localized CO₂ corrosion on carbon steels in wet gas services both experimentally and theoretically. A 100 mm I.D., 40 meter long flow loop is employed to perform the corrosion studies along the top and the bottom of the pipe under stratified and annular flow conditions. Various corrosion monitoring techniques, including ER, LPR, and WL, and surface analysis techniques, including SEM/EDS, MM, XRD, and XPS are used during the experiments and for post-test analysis.

The parametric study involves the systematic investigation for the effect of temperature, CO₂ partial pressure, flow (including gas and liquid phase flow rates and flow regimes), pH, Cl⁻, and oil on localized corrosion and formation of corrosion product films. When there is a very protective film or the surface is film free, localized corrosion does not occur; it only occurs when a partially protective film is formed.

In the present study, localized corrosion is found only at high temperature (90°C). It occurs in both Cl⁻ containing and Cl⁻ free solutions (with different pitting density). It also occurs at lower pH (4.5~6.0) while at pH 6.2 very protective films form and no localized corrosion is identified. CO₂ partial pressure affects film formation and thus the localized corrosion when a partially protective film is formed. Higher pressure, higher liquid and gas flow rate cause higher corrosion rate under film free conditions and also lead to annular flow, where the corrosion behavior on the top of the pipe is similar to the bottom. The presence of a hydrocarbon phase exhibits a favorable effect on preventing

localized corrosion allowing acceptably high gas flow rates even in non-inhibited environments.

The theoretical study presents here includes the development of a solution super saturation model and a scaling tendency model, which are good tools for predicting localized corrosion. It is found that localized corrosion occurs when the solution is only slightly above the saturation point and when the scaling tendency is between 0.3 and 3.0.

Approved: Srdjan Nesic

Professor of Chemical Engineering

ACKNOWLEDGEMENTS

The author would like to express her sincere gratitude and deep appreciation to her academic advisor, Dr. Srdjan Nestic for his expert guidance, steady support, and continuous encouragement during the completion of this dissertation. Under his supervision, the author was able to turn her last year's study into a successful, intellectually challenging, and enjoyable journey.

The author would like to specially thank her industry mentor, Dr. Yves Gunaltun from TotalFinaElf, for his industry oriented education, support and encouragement especially during a most critical time of this study.

The author would also like to thank Dr. Chuck Alexander for his mentoring during his interim directorship of the Institute for Corrosion and Multiphase Technology.

Great thanks also go to Dr. Christoph Bosch for his supervision and friendship during the most difficult days in author's study. Thanks also go to Dr. Tao Hong for his supervision during the first part of this project.

The support and helpful discussions from/with Dr. Martin Kordesch, Dr. David Ingram, Dr. Khairul Alam, Dr. Howard Dewald, Dr. Daniel Gulino, and Dr. Valerie Young are also greatly appreciated.

The author would like to extend her gratitude to the technical staff at the Institute for Corrosion and Multiphase Technology, including Mr. Al Schubert, Mr. Bruce Brown, and Mr. John Geottge, for their expertise in designing, building, troubleshooting, and maintaining the flow loop and equipment.

Last but not least, the author thanks her fellow graduate students, especially Mr. Keith George, Dr. Frederic Vitse for their support and friendship throughout the whole project. Special mention to Dr. Shihuai Wang for his support, daily care, and unselfish love during the author's study and Mr. Rick Castrop for his tremendous help, friendship, overall life philosophy, and far-reaching impact on her.

TABLE OF CONTENTS

ACKNOWLEDGEMENTS	5
LIST OF TABLES	10
LIST OF FIGURES	11
LIST OF FIGURES	11
CHAPTER 1: INTRODUCTION	18
CHAPTER 2: LITERATURE REVIEW	22
2.1 CO ₂ Corrosion and Environmental Factors	22
2.1.1 Temperature	23
2.1.2 Pressure	24
2.1.3 pH.....	25
2.1.4 Flow	27
2.1.5 Oil/water ratio	29
2.2 Corrosion Product Film Formation and Their Surface Morphology	30
2.2.1 Identification of Corrosion Product Film.....	30
2.2.2 Super Saturation and Scaling Tendency	31
2.2.3 The Characteristics of Corrosion Product Films.....	32
2.3 Localized Attack in CO ₂ Wet Gas Corrosion	34
2.3.1 Cl ⁻ Effect on Localized Corrosion	35
2.3.2 The Role of Corrosion Product Films.....	36
2.3.3 Steel Microstructure Effect	38
2.4 CO ₂ Corrosion Models.....	38
2.4.1 de Waard Model (1975, 1991, 1993,and 1995)	40
2.4.2 Netic Model (1996, 2001, and 2002).....	42
CHAPTER 3: RESEARCH OBJECTIVES AND TEST MATRIX.....	43
3.1 Research Objectives.....	43
3.2 Test Matrix.....	44
CHAPTER 4: EXPERIMENTAL SETUP & PROCEDURE	46
4.1 Description of The Flow Loop.....	46

	8
4.2 Description of The Test Section	48
4.3 Experimental Procedure.....	50
4.4 Corrosion Monitoring Techniques.....	52
4.4.1 Uniform corrosion measurements.....	52
4.4.2 Localized corrosion measurements.....	59
4.5 Corrosion Product Film Morphology Studies.....	61
4.5.1 Surface morphology and microstructure.....	61
4.5.2 Surface composition analysis.....	61
4.5.3 Cross-sectional analysis.....	65
4.6 Difficulties, Solutions, and Lessons to Be Learned.....	65
CHAPTER 5: EXPERIMENTAL RESULTS AND DISCUSSIONS.....	72
5.1 Baseline Test Establishment And Validation	72
5.1.1 Objectives	72
5.1.2 Results and Discussions.....	73
5.1.3 Surface Analysis	76
5.2 The Effect of Temperature in Wet Gas Flow	78
5.3 The Effect of Cl ⁻ Ions in Wet Gas Flow	83
5.3.1 Results On The Effect Of Cl ⁻	83
5.3.2 Discussions Of The Effect Of Cl ⁻	92
5.3.3 Summary For The Effect of Cl ⁻	98
5.4 The Effect of CO ₂ Partial Pressure in Wet Gas Flow	99
5.4.1 At 40°C	99
5.4.2 At 90°C	102
5.4.3 Summary On The Effect Of CO ₂ Partial Pressure.....	122
5.5 The Effect of pH in Wet Gas Flow	123
5.6 The Effect of Flow in Wet Gas.....	128
5.6.1 The Effect of Flow Velocity at 40°C	128
5.6.2 The Effect of Flow Velocity at High Temperature of 90°C	130
5.6.3 The Effect of Flow Regime.....	136
5.7 The Effect of Oil in Wet Gas Flow.....	138

	9
5.7.1 Results on The Effect of Oil	138
5.7.2 Discussion on the Effect of Oil	144
CHAPTER 6: PHYSICO-CHEMICAL MODEL DEVELOPMENT	147
6.1 Introduction.....	147
6.2 Super Saturation (SS) Level And Localized Corrosion.....	148
6.3 Scaling Tendency (ST) And Localized Corrosion.....	152
CHAPTER 7: CONCLUSIONS AND RECOMMENDATIONS	155
7.1 Conclusions.....	155
7.2 Recommendations.....	157
REFERENCES	158
APPENDIX A: SPECIMEN ETCHING PROCEDURE FOR MICROSTRUCTURE IDENTIFICATION.....	165
APPENDIX B: EXPERIMENTAL UNCERTAINTY ANALYSIS	166

LIST OF TABLES

Table 1.1 The statistics data of 15 years of natural gas pipeline explosion.....	18
Table 3.1 Test Matrix.....	44
Table 4.1 Chemical composition of type C-1010 carbon steel (wt.%).....	53
Table 4.2 Chemical Composition of Type C-1018 Carbon Steel (wt.%).....	56
Table 4.3 Chemical Composition of 5LX65 Steel (wt.%).....	56
Table 5.1.1 Test matrix for baseline experiment	73
Table 5.3.1 Test matrix for the effect of Cl ⁻ on localized corrosion.	83
Table 5.3. 2 Super-saturation (SS) table and the estimated pitting density for Cl ⁻ series test.	95
Table 5.4. 1 Natural pH and super saturation (SS) level at various CO ₂ partial pressures.	99
Table 5.4. 2 The test matrix for the series of test on the effect of CO ₂ partial pressure.	102
Table 5.7.1 The test matrix for the effect of oil on corrosion.....	138

LIST OF FIGURES

Figure 1.1 Typical flow patterns observed in wet gas pipelines.....	19
Figure 2.1 Solubility of iron carbonate as a function of pH at 2 bar CO ₂ partial pressure and 40°C (Dugstad, 1992).	26
Figure 2.2 A typical flow regime map for gas/liquid two-phase flow in horizontal pipes (Lee, 1993).....	28
Figure 2.3 A typical flow regime map for gas/oil/water three-phase flow in horizontal pipes (Lee, 1993).	29
Figure 2.4 Parameters affecting CO ₂ corrosion design (Kermani and Smith, 1997).....	39
Figure 4.1 A schematic sketch of the test loop.	46
Figure 4.2 A photograph of the flow loop.	47
Figure 4.3 A schematic sketch of the test section.	48
Figure 4.4 A photograph of the test section.	49
Figure 4.5 A photograph of pH measurement apparatus.	50
Figure 4.6 Retractable flush element electrical resistance probe (www.metalsamples.com).....	53
Figure 4.7 The diagram of the specimen.	55
Figure 4.8 The optical microstructure of type C1018 material (500x).	55
Figure 4.9 The optical microstructure of 5LX65 material (500x).	55
Figure 4.10 (a) Four coupon holder; (b) Coupon holder probe.	56
Figure 4.11 Replaceable flush-mount element of LPR probe.....	58
Figure 4.12 A steel plate under XRD.....	63
Figure 4.13 A blank specimen with aluminum holder under XRD.	63
Figure 4.14 A blank specimen with plastic holder under XRD.....	64
Figure 4.15 Moyno-“Tri phase system” multiphase progressive cavity pump.....	66
Figure 4.16 Parts of the gas pump. (a) gear ball; (b) suction housing; (c) connecting rod.	67
Figure 4.17 A stator failure in the gas pump.	70

Figure 5.1.1 The change of corrosion rate with time for the single-phase flow test in the wet gas system with 1% NaCl at T = 40°C, P = 4.45 bar (P _{co2} = 4.38 bar), and V _{sl} = 1 m/s.	74
Figure 5.1.2 Measured and predicted corrosion rate using different techniques from two flow loops with 1% NaCl at T = 40°C, P = 4.45 bar (P _{co2} = 4.38 bar), and V _{sl} = 1 m/s.	75
Figure 5.1.3 XRD analysis on the specimen without film after the baseline test with 1% NaCl at T = 40°C, P = 4.45 bar (P _{co2} = 4.38 bar), and V _{sl} = 1 m/s.	76
Figure 5.1.4 XRD analysis on a specimen with film after the baseline test with 1% NaCl at T = 40°C, P = 4.45 bar (P _{co2} = 4.38 bar), and V _{sl} = 1 m/s.	77
Figure 5.2.1 The effect of temperature on wet gas corrosion at V _{sl} = 0.1 m/s, V _{sg} = 10 m/s, and P _{total} = 4.5 bar (P _{co2} = 3.8 bar) with D.I. water only.	78
Figure 5.2.2 SEM surface morphology for 90°C bottom C1018 specimen at V _{sl} = 0.1 m/s, V _{sg} = 10 m/s, and P _{total} = 4.5 bar (P _{co2} = 3.8 bar) with D.I. water only..	79
Figure 5.2.3 SEM surface morphology for blank C1018 specimen without exposure to corrosion.	80
Figure 5.2.4 XRD spectrum for 90°C bottom C1018 specimen at V _{sl} = 0.1 m/s, V _{sg} = 10 m/s, and P _{total} = 4.5 bar (P _{co2} = 3.8 bar) with D.I. water only.	80
Figure 5.3.1 The change of bulk pH and Fe ²⁺ with time for 0.0% Cl ⁻ solution at V _{sg} = 10 m/s, V _{sl} = 0.1 m/s, T = 90°C, and P = 4.5 bar (P _{co2} = 3.8 bar).....	84
Figure 5.3.2 The change in corrosion rate with time for 0.0% Cl ⁻ solution at V _{sg} = 10 m/s, V _{sl} = 0.1 m/s, T = 90°C, and P = 4.5 bar (P _{co2} = 3.8 bar).....	85
Figure 5.3.3 Average and localized corrosion rate (LC) from different methods for the.	86
Figure 5.3.4 Cross sections for 0.0% Cl ⁻ solutions at V _{sg} = 10 m/s, V _{sl} = 0.1 m/s, T = 90°C, and P = 4.5 bar (P _{co2} = 3.8 bar). left: bottom C1018; right: bottom X-65.	86
Figure 5.3.5 The change of pH and Fe ²⁺ with time for 0.1% NaCl solutions at V _{sg} = 10 m/s, V _{sl} = 0.1 m/s, T = 90°C, and P = 4.5 bar (P _{co2} = 3.8 bar).....	88
Figure 5.3.6 The change of corrosion rate with Time for 0.1% NaCl solutions at V _{sg} = 10 m/s, V _{sl} = 0.1 m/s, T = 90°C, and P = 4.5 bar (P _{co2} = 3.8 bar).....	88

Figure 5.3.7 Average and localized corrosion rate (LC) from different methods for 0.1% NaCl solutions at $V_{sg} = 10$ m/s, $V_{sl} = 0.1$ m/s, $T = 90^{\circ}\text{C}$, and $P = 4.5$ bar ($P_{\text{co}_2} = 3.8$ bar).	89
Figure 5.3.8 Cross sections for 0.1% NaCl solutions at $V_{sg} = 10$ m/s, $V_{sl} = 0.1$ m/s, $T = 90^{\circ}\text{C}$, and $P = 4.5$ bar ($P_{\text{co}_2} = 3.8$ bar). (a) top C1018; (b) top X-65; (c) bottom C1018; (d) bottom X-65.	89
Figure 5.3.9 The change of pH and Fe^{2+} with time for 1% NaCl solutions at $V_{sg} = 10$ m/s, $V_{sl} = 0.1$ m/s, $T = 90^{\circ}\text{C}$, and $P = 4.5$ bar ($P_{\text{co}_2} = 3.8$ bar).	90
Figure 5.3.10 The change of corrosion rate with time for 1% NaCl solutions at $V_{sg} = 10$ m/s, $V_{sl} = 0.1$ m/s, $T = 90^{\circ}\text{C}$, and $P = 4.5$ bar ($P_{\text{co}_2} = 3.5$ bar).	91
Figure 5.3.11 Average and localized corrosion rate (LC) from different methods for 1% NaCl solutions at $V_{sg} = 10$ m/s, $V_{sl} = 0.1$ m/s, $T = 90^{\circ}\text{C}$, and $P = 4.5$ bar ($P_{\text{co}_2} = 3.8$ bar).	91
Figure 5.3.12 Cross sections for 1% NaCl solutions at $V_{sg} = 10$ m/s, $V_{sl} = 0.1$ m/s, $T = 90^{\circ}\text{C}$, and $P = 4.5$ bar ($P_{\text{co}_2} = 3.8$ bar). (a) top C1018; (b) top X-65; (c) bottom ER C1010; (d) bottom X-65.	92
Figure 5.3.13 The effect of NaCl concentration on bottom corrosion for different materials from WL method at $V_{sg} = 10$ m/s, $V_{sl} = 0.1$ m/s, $T = 90^{\circ}\text{C}$, and $P = 4.5$ bar ($P_{\text{co}_2} = 3.8$ bar).	93
Figure 5.3.14 The effect of Cl^- concentration on localized corrosion at $V_{sg} = 10$ m/s, $V_{sl} = 0.1$ m/s, $T = 90^{\circ}\text{C}$, and $P = 4.5$ bar ($P_{\text{co}_2} = 3.8$ bar) (note: 0.0001% Cl^- concentration is used to approximate no Cl^- condition to facilitate the graphical illustration).	94
Figure 5.3.15 The relationship between the super-saturation level and pitting density for the bottom at $V_{sg} = 10$ m/s, $V_{sl} = 0.1$ m/s, $T = 90^{\circ}\text{C}$, and $P = 4.5$ bar ($P_{\text{co}_2} = 3.8$ bar).	95
Figure 5.3.16 The effect of NaCl concentration on the average corrosion rate by ER measurements at $V_{sg} = 10$ m/s, $V_{sl} = 0.1$ m/s, $T = 90^{\circ}\text{C}$, and $P = 4.5$ bar ($P_{\text{co}_2} = 3.8$ bar).	96

Figure 5.3.17 SEM micrographs for 0.1% NaCl solutions at $V_{sg} = 10$ m/s, $V_{sl} = 0.1$ m/s, $T = 90^{\circ}\text{C}$, and $P = 4.5$ bar ($P_{\text{CO}_2} = 3.8$ bar). (a) top C1018; (b) top X-65; (c) bottom C1018; (d) bottom X65.	98
Figure 5.4.1 The effect of CO_2 partial pressure on both the top and the bottom corrosion rate at $V_{sl} = 0.1$ m/s, $T = 40^{\circ}\text{C}$ with D.I. water only.	100
Figure 5.4.2 The effect of CO_2 partial pressure on both the top and the bottom corrosion rate at $V_{sl} = 0.2$ m/s, $V_{sg} = 10$ m/s, $T = 40^{\circ}\text{C}$ with D.I. water only.	100
Figure 5.4.3 The pH and Fe^{2+} measurements with time for 1% NaCl at $V_{sg} = 10$ m/s, $V_{sl} = 0.1$ m/s, $T = 90^{\circ}\text{C}$, and $P = 11.3$ bar ($P_{\text{CO}_2} = 10.6$ bar).	103
Figure 5.4.4 The change of corrosion rate with time for 1% NaCl at $V_{sg} = 10$ m/s, $V_{sl} = 0.1$ m/s, $T = 90^{\circ}\text{C}$, $P = 11.3$ bar ($P_{\text{CO}_2} = 10.6$ bar), and $\text{pH} = 5.2$	104
Figure 5.4.5 The average and localized corrosion rate from different methods for 1% NaCl at $V_{sg} = 10$ m/s, $V_{sl} = 0.1$ m/s, $T = 90^{\circ}\text{C}$, $P = 11.3$ bar ($P_{\text{CO}_2} = 10.6$ bar), and $\text{pH} = 5.2$	105
Figure 5.4.6 SEM micrographs for 1% NaCl at $V_{sg} = 10$ m/s, $V_{sl} = 0.1$ m/s, $T = 90^{\circ}\text{C}$, $P = 11.3$ bar ($P_{\text{CO}_2} = 10.6$ bar), and $\text{pH} = 5.2$. (a) top C1018; (b) top X-65; (c) bottom C1018; (d) bottom X65.	107
Figure 5.4.7 Cross sections for 1% NaCl at $V_{sg} = 10$ m/s, $V_{sl} = 0.1$ m/s, $T = 90^{\circ}\text{C}$, $P = 11.3$ bar ($P_{\text{CO}_2} = 10.6$ bar), and $\text{pH} = 5.2$. (a) top C1018; (b) top X-65; (c) bottom C1018; (d) bottom X65.	108
Figure 5.4.8 The pH measurement with time for 1% NaCl at $V_{sg} = 10$ m/s, $V_{sl} = 0.1$ m/s, $T = 90^{\circ}\text{C}$, and $P = 4.5$ bar ($P_{\text{CO}_2} = 3.8$ bar).	109
Figure 5.4.9 The change of corrosion rate with time for 1% NaCl at $V_{sg} = 10$ m/s, $V_{sl} = 0.1$ m/s, $T = 90^{\circ}\text{C}$, $P = 4.5$ bar ($P_{\text{CO}_2} = 3.8$ bar), and $\text{pH} = 6.2\sim 6.3$	110
Figure 5.4.10 Average corrosion rate from different methods for 1% NaCl at $V_{sg} = 10$ m/s, $V_{sl} = 0.1$ m/s, $T = 90^{\circ}\text{C}$, $P = 4.5$ bar ($P_{\text{CO}_2} = 3.8$ bar), and $\text{pH} = 6.2\sim 6.3$	111
Figure 5.4.11 SEM micrographs for 1% NaCl solution at $V_{sg} = 10$ m/s, $V_{sl} = 0.1$ m/s, $T = 90^{\circ}\text{C}$, $P = 4.5$ bar ($P_{\text{CO}_2} = 3.8$ bar), and $\text{pH} = 6.2\sim 6.3$. (a) top C1018; (b) top X-65; (c) bottom C1018; (d) bottom X65.	112

Figure 5.4.12 Cross sections for 1% NaCl solution at $V_{sg} = 10$ m/s, $V_{sl} = 0.1$ m/s, $T = 90$ °C, $P = 4.5$ bar ($P_{CO_2} = 3.8$ bar), and $pH = 6.2\sim 6.3$. (a) top C1018; (b) top X-65; (c) bottom C1018; (d) bottom X65.....	113
Figure 5.4.13 The pH measurement with time for 1% NaCl at $V_{sg} = 10$ m/s, $V_{sl} = 0.1$ m/s, $T = 90$ °C, and $P = 11.3$ bar ($P_{CO_2} = 10.6$ bar).....	114
Figure 5.4.14 The change of corrosion rate with time for 1% NaCl at $V_{sg} = 10$ m/s, $V_{sl} = 0.1$ m/s, $T = 90$ °C, $P = 11.3$ bar ($P_{CO_2} = 10.6$ bar), and $pH = 6.2$	115
Figure 5.4.15 Average corrosion rate from different methods for 1% NaCl at $V_{sg} = 10$ m/s, $V_{sl} = 0.1$ m/s, $T = 90$ °C, $P = 11.34$ bar ($P_{CO_2} = 10.64$ bar), and $pH = 6.2$	115
Figure 5.4.16 SEM micrographs for 1% NaCl at $V_{sg} = 10$ m/s, $V_{sl} = 0.1$ m/s, $T = 90$ °C, $P = 11.3$ bar ($P_{CO_2} = 10.6$ bar), and $pH = 6.2$. (a) top C1018; (b) top X-65; (c) bottom C1018; (d) bottom X65.....	116
Figure 5.4.17 Cross sections for 1% NaCl at $V_{sg} = 10$ m/s, $V_{sl} = 0.1$ m/s, $T = 90$ °C, $P = 11.34$ bar ($P_{CO_2} = 10.6$ bar), and $pH = 6.2$. (a) top C1018; (b) top X-65; (c) bottom C1018; (d) bottom X65.....	117
Figure 5.4.18 The effect of CO_2 partial pressure on the corrosion rate at low $pH (\leq 5.2)$ from WL X65 steel at $V_{sl} = 0.1$ m/s, $V_{sg} = 10$ m/s, $T = 90^\circ C$ with 1% NaCl solution.....	118
Figure 5.4.19 The effect of CO_2 partial pressure on stabilized corrosion rate at low $pH (\leq 5.2)$ from ER technique at $V_{sl} = 0.1$ m/s, $V_{sg} = 10$ m/s, $T = 90^\circ C$ with 1% NaCl solution.	119
Figure 5.4.20 The effect of CO_2 partial pressure on the corrosion rate at high $pH (6.2\sim 6.3)$ from different measurement techniques at $V_{sl} = 0.1$ m/s, $V_{sg} = 10$ m/s, $T = 90^\circ C$ with 1% NaCl solution.	121
Figure 5.4.21 The effect of CO_2 partial pressure on stabilized corrosion rate at high $pH (6.2\sim 6.3)$ from ER technique at $V_{sl} = 0.1$ m/s, $V_{sg} = 10$ m/s, $T = 90^\circ C$ with 1% NaCl solution.	121

Figure 5.5.1 The effect of pH on the average and localized corrosion rate from WL X65 for 1% NaCl at $V_{sl} = 0.1$ m/s, $V_{sg} = 10$ m/s, $T = 90^{\circ}\text{C}$, and $P = 4.5$ bar ($P_{\text{co}_2} = 3.8$ bar).	123
Figure 5.5.2 The effect of pH on the stabilized corrosion rate from ER method for 1% NaCl at $V_{sl} = 0.1$ m/s, $V_{sg} = 10$ m/s, $T = 90^{\circ}\text{C}$, and $P = 4.5$ bar ($P_{\text{co}_2} = 3.8$ bar).	124
Figure 5.5.3 The effect of pH on average and localized corrosion rate from WL X65 for 1% NaCl at $V_{sl} = 0.1$ m/s, $V_{sg} = 10$ m/s, $T = 90^{\circ}\text{C}$, and $P = 11.3$ bar ($P_{\text{co}_2} = 10.6$ bar).	124
Figure 5.5.4 The effect of pH on stabilized corrosion rate from ER method for 1% NaCl at $V_{sl} = 0.1$ m/s, $V_{sg} = 10$ m/s, $T = 90^{\circ}\text{C}$, and $P = 11.3$ bar ($P_{\text{co}_2} = 10.6$ bar).	125
Figure 5.6.1 The effect of superficial velocities on corrosion at 40°C with 100% water cut under CO_2 partial pressure of 3.8 bar.	128
Figure 5.6.2 The effect of superficial velocities on corrosion at 40°C with 100% water cut under CO_2 partial pressure of 7.8 bar.	129
Figure 5.6.3 The change of corrosion rate with time for 1% NaCl at $V_{sl} = 0.1$ m/s, $V_{sg} = 5$ m/s, $T = 90^{\circ}\text{C}$, $P = 11.3$ bar ($P_{\text{co}_2} = 10.6$ bar), and $\text{pH} = 5.2$.	131
Figure 5.6.4 The average and localized corrosion rate from different methods for 1% NaCl at $V_{sg} = 5$ m/s, $V_{sl} = 0.1$ m/s, $T = 90^{\circ}\text{C}$, $P = 11.3$ bar ($P_{\text{CO}_2} = 10.6$ bar), and $\text{pH} = 5.2$.	132
Figure 5.6.5 SEM micrographs for 1% NaCl at $V_{sg} = 5$ m/s, $V_{sl} = 0.1$ m/s, $T = 90^{\circ}\text{C}$, $P = 11.34$ bar ($P_{\text{CO}_2} = 10.64$ bar), and $\text{pH} = 5.2$. (a) top C1018; (b) top X-65; (c) bottom C1018; (d) bottom X65.	133
Figure 5.6.6 Cross sections for 1% NaCl at $V_{sg} = 5$ m/s, $V_{sl} = 0.1$ m/s, $T = 90^{\circ}\text{C}$, $P = 11.3$ bar ($P_{\text{CO}_2} = 10.6$ bar), and $\text{pH} = 5.2$. (a) top C1018; (b) top X-65; (c) bottom C1018; (d) bottom X65.	134
Figure 5.6.7 The effect of superficial gas velocity on the corrosion rate from different measurement techniques at $\text{pH} = 5.2$ for 1% NaCl at $V_{sl} = 0.1$ m/s, $T = 90^{\circ}\text{C}$, and $P = 11.3$ bar ($P_{\text{CO}_2} = 10.6$ bar).	135

Figure 5.6.8 The schematic flow pattern transitions with superficial velocities and system pressure.	137
Figure 5.7.1 The change of corrosion rate with time from ER measurement at 80% water cut with $V_{sl} = 0.05$ m/s, $T = 90^{\circ}\text{C}$, and $P = 4.5$ bar ($P_{\text{co}_2} = 3.8$ bar).	139
Figure 5.7.2 Average corrosion rate from WL measurement at 80% water cut with $V_{sl} = 0.05$ m/s, $T = 90^{\circ}\text{C}$, and $P = 4.5$ bar ($P_{\text{co}_2} = 3.8$ bar).	140
Figure 5.7.3 SEM micrographs for coupons at $V_{sl} = 0.05$ m/s, $T = 90^{\circ}\text{C}$ and $P = 4.5$ bar ($P_{\text{co}_2} = 3.8$ bar). (a) $V_{sg} = 15$ m/s bottom; (b) $V_{sg} = 15$ m/s top; (c) $V_{sg} = 20$ m/s bottom; (d) $V_{sg} = 20$ m/s top.	141
Figure 5.7.4 XPS spectrum for bottom coupons at $V_{sl} = 0.05$ m/s, $V_{sg} = 20$ m/s, $T = 90^{\circ}\text{C}$ and $P = 4.5$ bar ($P_{\text{co}_2} = 3.8$ bar).	143
Figure 5.7.5 Cross sections for coupons at $V_{sl} = 0.05$ m/s, $T = 90^{\circ}\text{C}$ and $P = 4.5$ bar ($P_{\text{co}_2} = 3.8$ bar). (a) $V_{sg} = 15$ m/s bottom; (b) $V_{sg} = 15$ m/s top; (c) $V_{sg} = 20$ m/s bottom; (d) $V_{sg} = 20$ m/s top.	144
Figure 5.7.6 The effect of oil on the stabilized corrosion rate from ER method in pure water and water/oil system with different velocities at 90°C and $P = 4.5$ bar ($P_{\text{co}_2} = 3.8$ bar).	145
Figure 6.1 The graphical illustration of the three hypotheses related to localized corrosion.	147
Figure 6.2 The relationship between the super saturation level and the pitting factor for all the experiments.	149
Figure 6.3 The relationship between the super saturation level and the pitting density for all the experiments.	150
Figure 6.4 The magnified display of Figure 6.3 around the saturation line.	150
Figure 6.5 The relationship between the scaling tendency and pitting factor for all the experiments.	154

CHAPTER 1: INTRODUCTION

In the natural gas production industry, mild steel is extensively used for pipeline construction for economical reasons even though it has a relatively poor corrosion resistance. Natural gas does not emerge from the reservoir “pure” and is always accompanied by various amounts of oil, water, carbon dioxide, hydrogen sulfide or organic acids. These substances combined give rise to a very aggressive environment where the survival of mild steel is not guaranteed.

Every year, natural gas pipeline explosion takes people’s life away, causes injuries, millions or even billions of dollars of property damage, as reported by the U.S. office of pipeline safety (Table 1.1). The majority of the accidents are due to the internal corrosion of the pipeline.

Table 1.1 The statistics data of 15 years of natural gas pipeline explosion.

FIFTEEN YEARS OF EXPLOSIONS				
Number of deaths from natural gas pipeline explosions through June 30:				
Year	Accidents	Deaths	Injuries	Property Damage
1986	83	6	20	\$11,166,262
1987	70	0	15	\$4,720,466
1988	89	2	11	\$9,316,078
1989	103	22	28	\$20,458,939
1990	89	0	17	\$11,302,316
1991	71	0	12	\$11,931,238
1992	74	3	15	\$24,578,165
1993	95	1	17	\$23,035,268
1994	81	0	22	\$45,170,293
1995	64	2	10	\$9,957,750
1996	77	1	5	\$13,078,474
1997	73	1	5	\$12,078,117
1998	99	1	11	\$29,749,310
1999	54	2	8	\$17,695,937
2000	40	1	13	\$6,861,214
Totals	1,162	42	209	\$251,099,827
The Associated Press				
Source: U.S. Office of Pipeline Safety.				

The multi-phase mixtures of gaseous and liquid hydrocarbons, water, CO₂ and H₂S moves through gas pipelines in a variety of complicated flow patterns such as annular, mist, slug and stratified flow, depending on the terrain topography and the individual phase flow rates. Stratified flow is the most common flow regime found in practice, where the liquid phase (mixture of water and condensed hydrocarbons) is transported along the bottom of the pipe, while the gaseous phase (a mixture of gaseous hydrocarbons, CO₂ and H₂S) is transported in the upper portion of the pipe with some liquid droplets entrained in the gas phase. In annular flow, the liquid phase contacts the pipe wall's entire perimeter with a gas core in the middle. This flow usually occurs when either the pipeline is in a vertical orientation, such as a riser, or when the gas velocity is high. At very high gas velocities and low liquid contents, a mist flow can be achieved. The most common flow patterns observed in wet gas pipelines are shown in Figure 1.1 (Vedapuri et al., 2000).

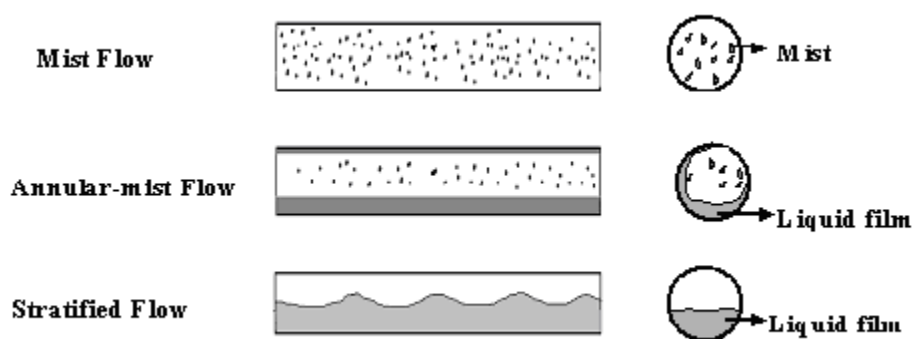


Figure 1.1 Typical flow patterns observed in wet gas pipelines.

It is well known that flow can accelerate corrosion of mild steel by increasing the mass transfer of corrosive species and/or by damaging the protective films on the steel surface (Nesic et al., 2001). In wet-gas pipelines, the typical flow patterns mentioned above enhance the internal corrosion for both the top and the bottom of the pipe.

In the oil and gas industry, significant progress has been achieved in understanding uniform CO₂ corrosion of mild steel in the past 20 years, (de Waard and Milliams, 1975, Dugstad et al., 1994, Vuppu and Jepson, 1993, Bhongale, 1995, Nesic and Lunde, 1994, Palacios and Shadley, 1991). However, localized corrosion is still not well understood even though research has been done in this field. Localized corrosion is much more dangerous in service, since most of the failures in lines are caused by localized attack, which is more difficult to predict or detect than uniform corrosion.

In the field of wet gas corrosion research, there are only a handful of studies that relate to field experience, some focusing on corrosion management (Kapusta et al., 1999) and control (Gunaltun and Belghazi, 2001), others reporting actual case histories (Gunaltun et al., 1999). In most studies the focus was on top-of-line corrosion (Gunaltun and Larrey, 2000, Pots and Hendriksen, 2000) where high uniform corrosion and sometimes, localized attack, were associated with rapid condensation of water by external cooling. There are no studies reported in the open literature, which investigate the nature and magnitude of the attack in wet gas transport in the presence of low condensation rates, typical for well-insulated pipelines.

Previous studies reported in the open literature covering localized CO₂ corrosion of carbon steels have all been conducted in single-phase water flow (Xia et al., 1989,

Schmitt et al., 1996, 1999, 2000, Nyborg, 1998). The apparatus used in those studies were the rotating cylinder electrode, jet impingement, autoclaves, and small diameter flow loops. These experimental systems have the advantage of providing easy and inexpensive testing under controlled conditions. However, they do not take into account the effect of multiphase flow and the presence of various flow regimes encountered in oil/water/gas pipelines. Obviously, there is a gap between the single-phase flow laboratory corrosion studies and the multi-phase flow field application, which needs to be closed.

The present research was performed in an industrial-scale research facility - a 100 mm ID multiphase corrosion flow loop. The effect of various parameters on wet gas corrosion was systematically investigated, including temperature, pressure, solution composition, pH, flow, and water cut. The most important parameters in the onset of localized attack of mild steel in wet gas transportation were also identified. A physico-chemical model was then developed based on the experimental findings. The results have improved the fundamental understanding and raised the awareness for localized corrosion in wet gas transportation.

CHAPTER 2: LITERATURE REVIEW

Corrosion is a potential hazard associated with oil and gas production and transportation facilities. In fact, CO₂ corrosion, or the so called “sweet corrosion”, is by far the most prevalent form of attack encountered in oil and gas production and is a major concern in the application of carbon and low alloy steels, which are still the principle construction materials used for the majority of facilities in oil and gas production offering economy, availability and strength (Kermani and Smith, 1997, Gunaltun, 1997). In practice, localized corrosion is the most frequent mode of attack and results in very high corrosion rates. However, little attention has been paid to understand and predict localized CO₂ corrosion though significant progress has been achieved in the past decades for uniform corrosion.

2.1 CO₂ Corrosion and Environmental Factors

The basic CO₂ corrosion reactions have been understood and well accepted through the work in the past few decades. The major chemical reactions include CO₂ dissolution and hydration to form a weak carbonic acid,



which then dissociates into bicarbonate and carbonate ions through two steps:



When the concentration of Fe^{2+} and CO_3^{2-} ions exceed the solubility limit, they combine to form solid iron carbonate films (which is often called the corrosion product film) according to:



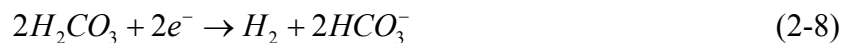
The electrochemical reactions at the steel surface include the anodic reaction of iron dissolution:



and two cathodic reactions. One of the reactions is the hydrogen evolution reaction:



and the other is direction reduction of carbonic acid:



Having stated the above mechanism with CO_2 corrosion, one can understand that a number of environmental factors, such as solution chemistry, flow velocity, temperature, pressure, and pH etc., affect the uniform CO_2 corrosion rate of mild steel. The following paragraphs will discuss the effect of some of the important factors on CO_2 corrosion in the oil and gas industry.

2.1.1 Temperature

Temperature has two major effects on corrosion. On the one hand, higher temperature allows for increased reaction rates (in this case it would be the corrosion rate); on the other hand, the increased temperature also accelerates the kinetics of corrosion product precipitation. In CO_2 services, the corrosion product, iron carbonate

precipitates out of solution and deposits on the metal surface after its solubility limit is achieved. de Waard and Milliams (1975) reported that the corrosion rate increases with temperature from 30°C to 60°C, reaches a maximum between 60°C and 70°C, and thereafter decreases until 90°C, which corresponded with FeCO₃ precipitation. Echoing this, Dugstad et al (1994) found increased corrosion rates with increasing temperature that reached a maximum corrosion rate between 60°C and 90°C. However, all this work has been done under single-phase flow test conditions. In multi-phase flow conditions, similar results from full pipe (oil/water) flow conditions were obtained with the appearance of maximum corrosion rate at 90°C (Vuppu and Jepson, 1993). Meanwhile, a different trend in temperature was observed in slug flow where no maximum corrosion rate was achieved at any temperature between 40°C and 90°C (Bhongale, 1995). Instead, the corrosion rate continued to increase with temperature.

However, there is no research showing the effect of temperature in wet gas conditions, let alone the impact on localized corrosion.

2.1.2 Pressure

The total pressure may/will change the fluid properties such as the gas density and viscosity. From a corrosion point of view, the partial pressure of CO₂ (or the fugacity of CO₂ under extreme high pressures) is a major concern due to its high solubility in aqueous water and hydrocarbons. The general understanding of the effect of CO₂ partial pressure in corrosion had been expressed in the early deWaard-Milliams “worst case” corrosion prediction model (1975). An increase in CO₂ partial pressure will lead to an increase in corrosion rate. This seems to have been well accepted through out the

industry. Most published research (Dugstad et al., 1994, de Waard and Lotz, 1993) agrees that the corrosion rate is proportional to the CO₂ partial pressure to the power of approximate 0.7. This might be true at low pressure without the control of pH, where the main function of CO₂ pressure is the contribution to the pH. However, when other conditions are favorable for formation of iron carbonate film, increased CO₂ partial pressure may help to facilitate the film formation, and the actual corrosion rate might behave differently compared to film-free corrosion (Nesic et al., 2002). Once again, no published work has reported the impact of CO₂ partial pressure on localized corrosion in wet gas flow conditions.

2.1.3 pH

pH indicates the concentration of protons in solution, which is the major species involved in cathodic reaction in corrosion process. Early research has found the following correlation:

$$\log i_c = -A pH + B \quad (2-9)$$

where, i_c is the corrosion current. deWaard and Milliams (1975) gave A a value of 1.3 in their early work. But the mechanism for the cathodic reaction was explained to be the direct reduction of carbonic acid, and the reduction of protons was ignored. Other researchers (Nesic et al., 1996) indicated different mechanisms with different pHs. At low pH (pH<4.5) and low CO₂ partial pressure (≤ 1 bar), a flow sensitive H⁺ reduction dominates the cathodic reaction while the amount of dissolved CO₂ controls the cathodic reaction rate at higher pH (pH>5) and higher CO₂ partial pressure (≥ 1 bar).

In addition to the effects on the electrochemical reaction rates, pH also has a dominant effect on the formation of iron carbonate films due to its effect on the solubility of iron carbonate, as illustrated in Figure 2.1.

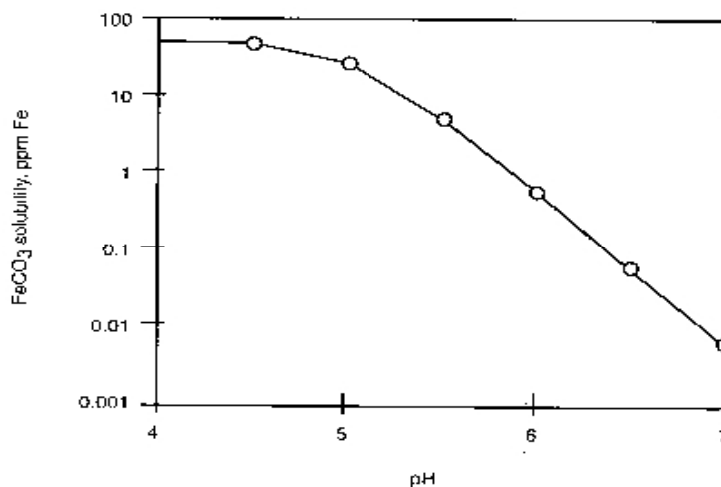


Figure 2.1 Solubility of iron carbonate as a function of pH at 2 bar CO₂ partial pressure and 40°C (Dugstad, 1992).

It has been seen that the solubility of iron carbonate is reduced with the increase in pH. Thus, a higher pH results in an increased super saturation (which is defined as the ratio of the product of $[\text{Fe}^{2+}]$ and $[\text{CO}_3^{2-}]$ to the solubility of FeCO_3) of iron carbonate and subsequent acceleration in precipitation and deposition of the corrosion product scale on the steel surface. This has been confirmed both experimentally (Dugstad, 1992) and computationally (Nesic et al., 2001). However, no work has ever addressed the pH effect on localized corrosion.

2.1.4 Flow

Multiphase flow can be simply described by the flow rate and the flow regime. Fluid flow affects corrosion mainly through the mass transport process involved in the corrosion mechanism. This type of corrosion is often called flow affected or flow accelerated corrosion (FAC).

Generally, higher flow rates are directly associated with higher turbulence and more effective mixing in the solution. It affects not only the corrosion rate but also the precipitation rate of iron carbonate (Nesic et al., 2002). Both effects contribute to less protective films being formed at higher velocities. Under extremely high velocities, flow can even mechanically remove corrosion product films and cause erosion corrosion. Hara et al. (2000) studied the effect of flow velocity on CO₂ corrosion behavior in an oil and gas environment. No corrosion films were formed in their tests above a flow velocity of 2 m/s, even up to 120°C. Thus they concluded that the corrosion rate of carbon steel is velocity dependent and increases with an increase in the Reynolds number or temperature.

Flow regime becomes a very important factor for corrosion when multiphase flow exists. Figure 2.2 and Figure 2.3 show the typical flow regime maps for a gas/liquid two phase and a gas/oil/liquid three phase flow obtained in a 100 mm I.D. flow loop.

Each type of flow regime contributes differently to the corrosion rate. For example, if the flow is in a stratified regime, the top of the line is very likely to have a different corrosion rate from the bottom of the line due to the different water chemistry. A specific top of line (TOL) corrosion can take place in wet gas pipelines as the fresh condensing water is very corrosive (Olsen and Dugstad, 1991) and also due to the

unavailability of corrosion inhibitors on the top of the line (Gunaltun et al., 2000). In wet gas transportation, stratified and annular flow are the two predominant flow regimes occurring in pipelines. No research has been reported in these two flow regimes.

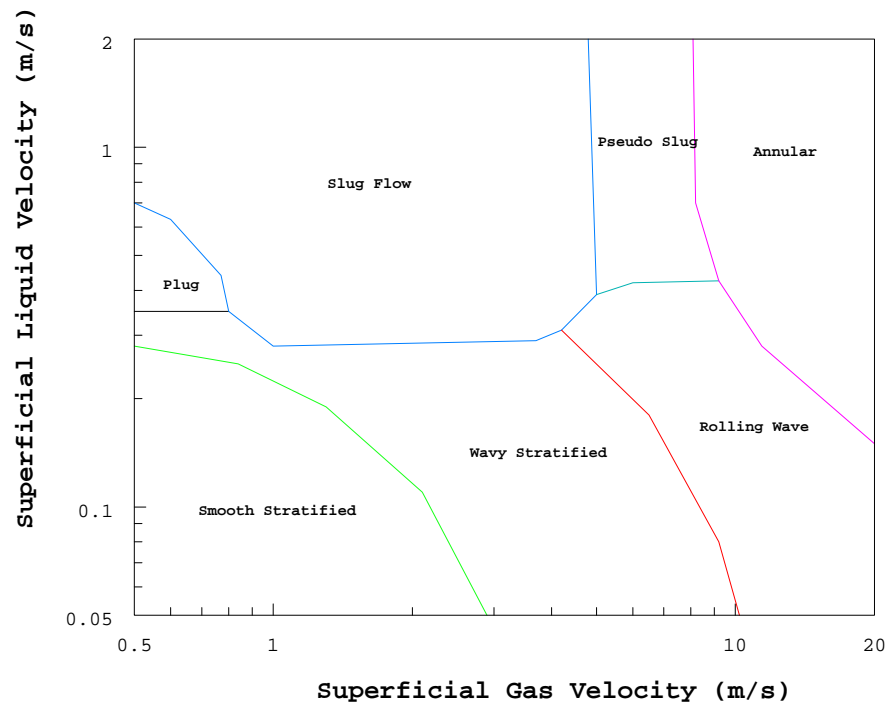


Figure 2.2 A typical flow regime map for gas/liquid two-phase flow in horizontal pipes (Lee, 1993).

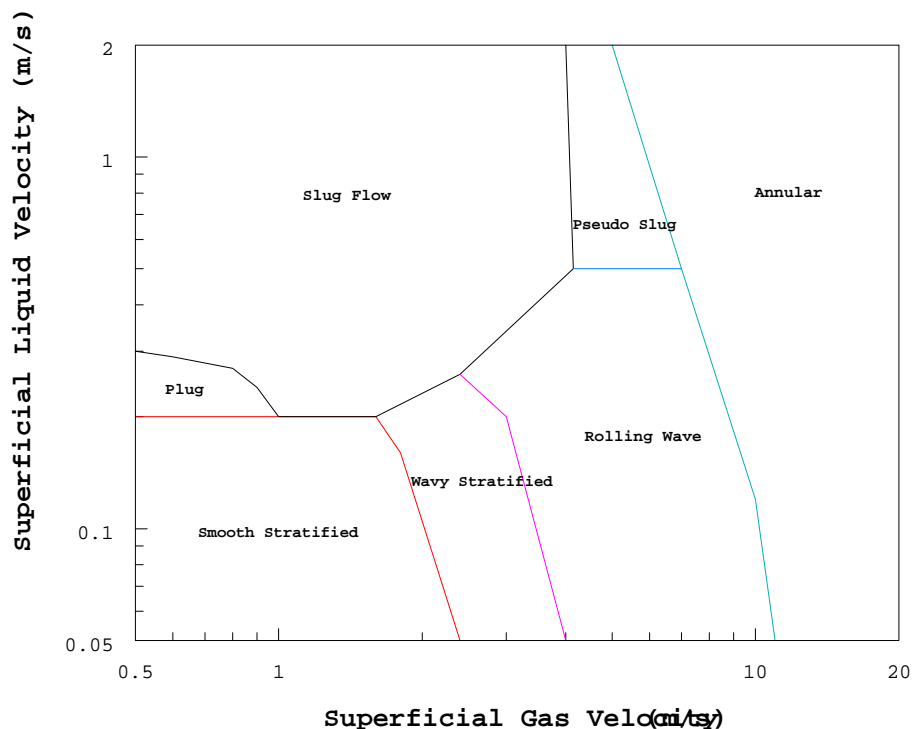


Figure 2.3 A typical flow regime map for gas/oil/water three-phase flow in horizontal pipes (Lee, 1993).

2.1.5 Oil/water ratio

For CO₂ corrosion to occur, there must be water present in contact with the steel surface. The severity of the CO₂ corrosion attack is proportional to the time that the steel surface is wetted by the water phase (Kermani and Smith, 1997). Thus the water cut is an important factor. However, the effect of the water cut cannot be separated from the flow velocity and the flow regime. The investigation of such an effect cannot be completed without a multiphase flow loop. During the past 10 years, significant efforts had been put into the multiphase flow studies, but the focus were on either oil/water full pipe flow

(Shi, 2001, Hong, 2000 etc.) or on slug flow (Wang, 2001, Wang, 2001). No research on the effect of oil has been done with wet gas flow.

The aforementioned parameters are the major ones affecting uniform CO₂ corrosion in the absence of corrosion product films and have received a lot of attention in the past. One might have noticed that almost all the parameters discussed above affect CO₂ corrosion differently depending on whether the steel surface is film (scale) free or if there is formation of an iron carbonate film. Therefore, the corrosion product films became the focus of attention because it can retard corrosion. The following section is dedicated to the overview of literature about the formation of corrosion product films.

2.2 Corrosion Product Film Formation and Their Surface Morphology

2.2.1 Identification of Corrosion Product Film

The identification of corrosion products on the surface is a very important approach to the understanding of various corrosion processes (Fu, 1994). Most of the research relating to CO₂ corrosion of mild steel concluded that iron carbide (Fe₃C) and iron carbonate (FeCO₃) are the two major corrosion products. FeCO₃ is formed when the concentration of Fe²⁺ in the solution exceeds the super saturation level of FeCO₃ (Dugstad, 1992, Heuer and Stubbins, 1998). FeCO₃ films usually have protective properties and reduce the corrosion rate by offering greater resistance to diffusion of species involved in the electrochemical reactions and/or by simply blocking the reaction surface (Nesic and Lunde, 1994). In contrast, iron carbide is a non-protective film and can even accelerate corrosion through a galvanic effect (Crolet, 1998, Nesic, 1994).

Strictly speaking, iron carbide is not a reaction product from the corrosion process. Instead, it is formed as iron corrodes and the alloy elements/impurities leach out. Fe_3C might be seen as a “skeleton” of the metal that remains after the corrosion process. It is often labeled as the “uncorroded portion of the metal.” Such films are very porous and non-protective (Jasinski, 1986).

2.2.2 Super Saturation and Scaling Tendency

Two important papers in the literature (van Hunnik et al, 1996, Pots and Hendriksen, 2000) approached the iron carbonate film formation quantitatively and thereafter implemented by other researchers computationally (Nesic et al., 2002). A brief review of the iron super saturation level and its relationship to scaling tendency is given in this section.

It is well known that the iron super saturation level SS is defined as follows:

$$SS = \frac{[Fe^{2+}][CO_3^{2-}]}{K_{sp}} \quad (2-10)$$

where, K_{sp} is the solubility product of iron carbonate, which is the function of temperature and solution ionic strength; $[Fe^{2+}]$ and $[CO_3^{2-}]$ represent the equilibrium concentrations of ferrous ion and carbonate ion. If SS is equal to one, the solution is at saturation; if SS is larger than one, then super saturation is achieved; an under saturated solution exists if SS is less than one.

When a solution reaches a super saturation level, iron carbonate precipitates out of the solution and deposits on the metal surface. The precipitation kinetics of iron carbonate proposed by van Hunnik et al. (1996) is as follows:

$$[Fe^{2+}]_{prec} = k_r \frac{A}{V} K_{sp} (S-1)(1-S^{-1}) \quad (2-11)$$

Where, k_r is the temperature dependent rate constant, and A/V is the metal surface area/solution volume ratio. The rate constant k_r was experimentally determined as:

$$k_r = e^{A - \frac{B}{RT}} \quad (2-12)$$

where A, B are constants and have the values of 52.4 and 119800, respectively.

In the same paper (van Hunnik et al., 1996), the authors proposed a so-called “scaling tendency” concept to describe protective film formation. The scaling tendency is defined as the ratio of the scale precipitation rate to the corrosion rate expressed in the same units. When the scaling tendency exceeds around 0.5, a protective film is considered to form and is no longer undermined by corrosion.

2.2.3 The Characteristics of Corrosion Product Films

Apparently, the formation of corrosion products and their surface morphology are strongly dependent upon the flow conditions, solution chemistry, flow geometry factors, pH, CO₂ partial pressure, and temperature (Palacios and Shadley, 1991). These parameters influence the corrosion mechanism and, therefore, the resulting corrosion rate and the corrosion products formed vary accordingly. For example, Palacios and Shadley (1991) found that in CO₂ saturated NaCl brine, FeCO₃ scales were very brittle and, under some conditions, can be removed easily from the metal surface. They observed two types of scales: the “primary” scale, formed directly on the corroding metal surface, and the “secondary” scale, formed on the top of the primary scale. They also indicated that the

primary scales were densely packed and uniform and were thicker than the secondary ones.

Nesic and Lunde (1994) performed experiments on CO₂ corrosion in gas and water two-phase flow. They found that iron carbide was the dominant species at low temperatures (e.g., 20°C). As the temperature was raised to 80°C and the solution became supersaturated, the formation of an iron carbonate film became more pronounced. The protective films formed in their tests appeared very robust and resistive to severe flow conditions. Localized corrosion was initiated and then developed into a pit-like attack when protective film formed quickly.

Heuer and Stubbins (2000) characterized iron carbonate films using X-ray photoelectron spectroscopy (XPS) to aid in the identification of potentially passive films on specimens exposed to CO₂ corrosion. The examination revealed that FeCO₃ is stable in the ripened form (Ostwald ripened for 48 hours at 75°C) and does not alter its structure with extended exposure to dry air. In the unripened form, however, FeCO₃ is unstable and quickly decomposes into Fe₂O₃ in air.

Olsen and Dugstad (1991) carried out experiments under water condensing conditions to study the CO₂ corrosion of carbon steel. Without a corrosion inhibitor, they found a black corrosion film consisting primarily of Fe₃C and FeCO₃. At high temperature (70°C), the films were thin, difficult to remove, and resulted in a reduction of the corrosion rate.

From scanning electron microscopy (SEM), Dugstad (1992) found that at low temperature (20 and 40°C) mainly iron carbide was formed. But protective films were formed at 80°C after 20~40 hours. In these tests, the corrosion rate would increase with

temperature and reached a maximum in the temperature range 60~90°C. The phenomena was attributed to the higher precipitation rates of iron carbonate at elevated temperatures.

De Moraes et al. (2000) studied FeCO_3 scales formed in a flow loop under various CO_2 corrosion conditions. SEM examinations showed two main types of scale development. One type of scale was a thin (less than 30 μm), very compact and adherent scale that was always related to a pronounced reduction in the corrosion rate. This very protective scale was present only at high temperature (93°C) and high pH (pH>5.0). Another type, usually a thick (~100 μm) and porous scale, showed only a partial ability to reduce the corrosion rate.

Although extensive investigation has been conducted on the corrosion product films in the past 20 years, none of the studies above discussed the properties of the corrosion product film and corrosion behavior in annular or stratified flow wet gas conditions.

2.3 Localized Attack in CO_2 Wet Gas Corrosion

In practice, pipeline failure is rarely caused by uniform corrosion, but rather by localized corrosion, such as pitting, mesa type corrosion, and erosion-corrosion. When localized corrosion exists, it is usually much more serious and dangerous than uniform attack. Even one pit can penetrate the pipe wall, cause leaks and subsequent failure. The stainless steels and nickel alloys with chromium depend on a passive film for corrosion resistance and are especially susceptible to pitting by local breakdown of the film at

isolated sites (Jones, 1996). Carbon steel is considered to be a material usually suffering general corrosion and received much less attention when it comes to localized corrosion.

2.3.1 Cl⁻ Effect on Localized Corrosion

Most work in the area of localized corrosion focused on the pitting corrosion of stainless steel (or passive metals) in the presence of chlorides or other halides (Jones, 1996). This is due to most failures in stainless alloys occurring in neutral to acid solutions with chloride ions or ions containing chlorine. Such conditions are of importance in the marine and chemical process industries among others. Little research has been dedicated to carbon steel localized corrosion and what is mostly focused on the wastewater and nuclear industry. For example, Brossia and Cragolino (2000) studied the effect of environmental variables on localized corrosion of carbon steel in alkaline solutions. They found that a number of environmental factors, such as pH, [Cl⁻], temperature, and steel corrosion potential play important roles in determining the corrosion behavior of carbon steels. Two critical environmental variables acted as enabling parameters for localized corrosion of carbon steel: a pH_{crit} of 9.3 to 9.6, above which localized corrosion of carbon steel took place and below which general corrosion was observed; and a [Cl⁻]_{crit} between 0.12 mM and 1.2 mM, below which localized corrosion of carbon steel did not take place in pH 11 solutions.

In a CO₂ environment, Schmitt and Feinen (2000) addressed the effect of anions and cations on the pit initiation of iron and steel. They observed pitting corrosion in both Cl⁻ and Cl⁻-free solutions in an autoclave. The effect of Cl⁻ concentration was also

investigated. It was found that Cl^- could inhibit pitting at low concentrations (10^{-4}M) but facilitate pitting at high concentrations.

2.3.2 The Role of Corrosion Product Films

Previous studies in the open literature covering localized CO_2 corrosion of carbon steels have all been conducted in single-phase water flow. The corrosion product film, iron carbonate, was found to play an essential role in this process.

Ikeda et al. (1984) found that the CO_2 corrosion mechanism of carbon steel is related to the temperature dependence of FeCO_3 film formation. They suggested that corrosion can be classified into three types according to temperature: below 60°C , the first type of general corrosion is observed; above 150°C , the third type of self-arresting corrosion is observed by forming a protective FeCO_3 film to prevent further attack; while in the intermediate temperature of approximately 100°C , deep pitting and ringworm corrosion are observed. The authors explained that the corrosion process at this temperature would create a coarse, porous, thick film of FeCO_3 on the substrate. Part of the metal that is not covered by the film act as anodic sites in the corrosion process, where many deep pits could initiate and develop into ringworm corrosion.

Xia et al. (1989) studied pitting corrosion of carbon steel at room temperature and atmospheric pressure in a 1000 mL electrolytic cell and suggested that galvanic couples were responsible for initiation and development of pits. The primary corrosion product was identified as $\text{Fe}(\text{HCO}_3)_2$, which formed a tight, adherent film on the metal surface. Longer exposures transformed $\text{Fe}(\text{HCO}_3)_2$ into FeCO_3 in the form of a porous, non-adherent and non-protective layer.

Schmitt et al. (1996, 1999) performed numerous experiments and concluded that the onset of localized attack was related to high near-wall levels of turbulence and the intrinsic growth stresses in the corrosion product scale. Defects created in protective scales result in localized metal dissolution at the sites of scale defects and are further reinforced by flow, which was named as flow induced localized corrosion (FILC).

Nyborg (1998) investigated initiation and growth of mesa attack by video recordings in flow loop experiments performed at 80°C and pH 5.8. He proposed a mechanism that a mesa attack results from several small local attacks that start at about the same time and then grow into one large attack. The small local corrosion occurs first beneath a partially protective film, and the flow can tear away the remaining lid of corrosion films. A galvanic cell can be set up between the film-free corroding metal in the bottom of the mesa attack and the film-covered metal outside the mesa attack. The author proposed that a prerequisite for mesa attack is that a partially protective corrosion film is formed first.

Actually, the common underlying theme in all these studies is that localized attack in CO₂ corrosion of mild steel is always associated with the formation and breakdown of protective iron carbonate films. However, it needs to be stressed again that there are no studies on localized corrosion conducted under wet gas flow conditions simulating gas production lines in the field. Errors could result from applying those small-scale and single phase laboratory test results to multiphase field applications.

2.3.3 Steel Microstructure Effect

From the viewpoint of CO₂ corrosion, steel microstructure can be described in terms of its chemical composition and heat treatment (Al-Hassan, 1998). The corrosion product film protective properties and its adherence to the substrate can vary greatly for carbon steels with apparently the same composition and microstructure. Dugstad et al. (2001) studied the effect of tempering temperature and the size and distribution of the carbides on the corrosion rate and the adherence of the corrosion product film. They found that both the general corrosion rate and the susceptibility of localized attack were significantly affected by steel microstructure. Besides this, most researchers (Ikeda, 1984, Al-Hassan, 1998, Dugstad, 2001) concluded that increasing the chromium content in the alloy enhances the corrosion resistance. Thus the steel's chemical composition and microstructure should always be specified in corrosion research.

2.4 CO₂ Corrosion Models

The oil and gas industry still relies heavily on the extensive use of carbon and low alloy steels. Thus there is a need to predict the severity of CO₂ corrosion of these materials, and this becomes more important in the design stage for the production equipment and transportation facilities.

In the past 30 years, various models including empirical (de Waard and Milliams, 1975, Dugstad et al., 1994, and Gunaltun, 1996, etc.), semi-empirical (de Waard et al., 1995, etc.), and mechanistic models (Pots, 1995, Zhang, 1997, Dayalan et al., 1998, and Nesic et al., 2001, etc.) have been developed for CO₂ corrosion. Without exception, these

models have more or less taken the important parameters reviewed in the previous three sections into consideration. These parameters are summarized in Figure 2.4 on the perspective of CO₂ corrosion design.

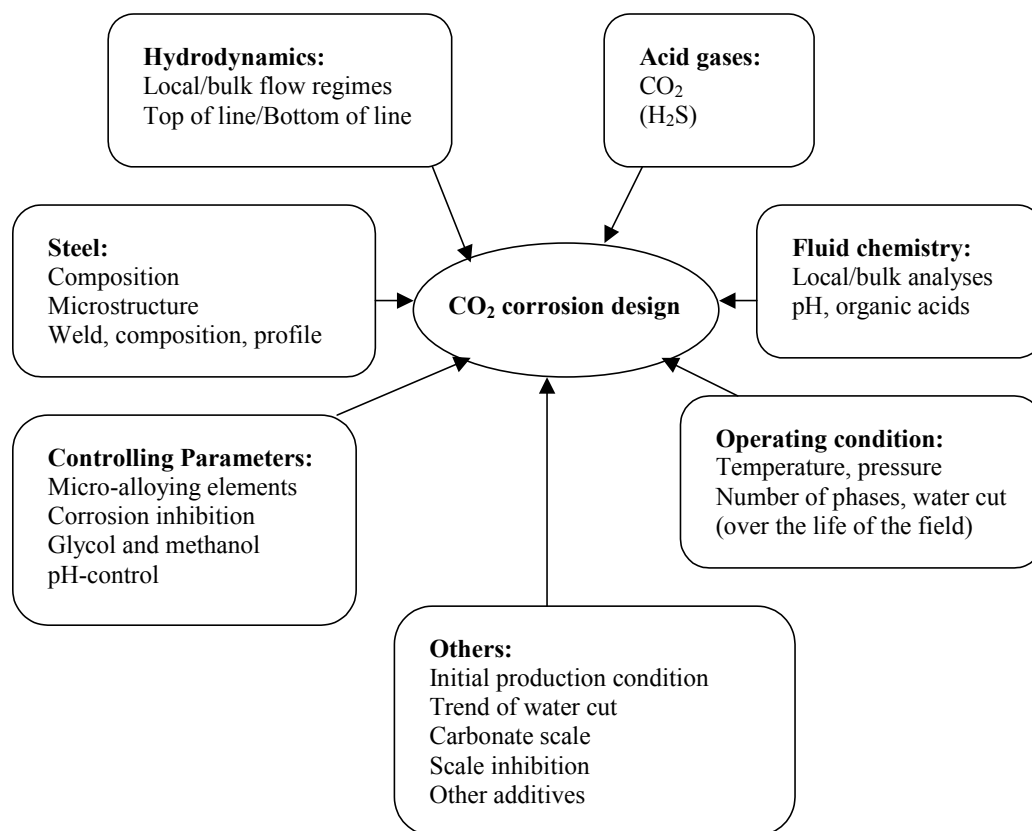


Figure 2.4 Parameters affecting CO₂ corrosion design (Kermani and Smith, 1997).

Nyborg (2002) performed a detail overview and performance evaluation for 16 CO₂ corrosion prediction models. It was found that the models differ considerably in how they predict the effect of protective corrosion films and the effect of oil wetting on CO₂ corrosion. These two factors account for the most pronounced difference between the various models. Generally, the models with a very strong effect of protective films

predict low corrosion rates and do not consider localized attack possible. The models with a weak effect of corrosion films predict higher corrosion rates and assume limited protection from the corrosion product film. The protective properties of corrosion product films are not well integrated into these models.

In fact, the success of a prediction model depends to a large degree on whether it is able to predict the presence or absence of protective films as well as localized attack reliably, rather than the ability to predict the general corrosion rate with certain accuracy. A couple of models that should be considered to be milestone contributions in CO₂ corrosion model development are reviewed in this section.

2.4.1 de Waard Model (1975, 1991, 1993, and 1995)

The model developed by de Waard and his coworkers is a semi-empirical model based on the correlation of the theoretical equations with experimental data. For many years, this model has been the most widely accepted CO₂ corrosion model in the oil and gas industry. The so-called “worst case” corrosion rate prediction model developed in 1975 only included the effects of temperature and partial CO₂ pressure, as described in the following equation:

$$\log V_{\text{nomo}} = 5.8 - \frac{1710}{T} + 0.67 \log(p_{\text{CO}_2}) \quad (2-13)$$

where V_{nomo} is the nomogram corrosion rate in mm/yr, T is the temperature in °K, and P_{CO_2} is the partial pressure of CO₂ in bar.

A later version, further referred to as the 1991 model, added different correction factors into the original equation, to account for pH, corrosion product films, total pressure, oil wetting, top of line corrosion, and inhibitors, etc. Some of the correction

factors were revised in the 1993 version, where the framework for a new model with effect of fluid velocity was proposed. The 1995 version took the effect of mass transport and fluid velocity into account and developed a so-called “resistance model” as follows:

$$\frac{1}{V_{cor}} = \frac{1}{V_r} + \frac{1}{V_m} \quad (2-14)$$

where V_{cor} is corrosion rate, V_r is the charge transfer controlled reaction rate, that is, when mass transfer is infinitely fast, and V_m is the highest possible mass transfer rate of the corrosive species. The units for each item are mm/yr. V_r and V_m are defined as

$$\log(V_r) = 4.93 - \frac{1119}{T} + 0.58 \log(p_{co_2}) - 0.34(pH_{actual} - pH_{co_2}) \quad (2-15)$$

$$V_m = 2.45 \frac{U^{0.8}}{d^{0.2}} p_{co_2} \quad (2-16)$$

where U is the flow velocity in m/s, d is the pipe diameter in m, pH_{co_2} is the pH of pure water and CO_2 system, and pH_{actual} is the actual measured pH.

Like all the other semi-empirical models, this model allows good interpolation since it is the best fit of the experimental data, but extreme care should be taken when the application is extrapolated outside the experiment range due to its uncertainty. In addition, predictions are believed to be worst-case as only limited credit can be taken for the protection by a corrosion product layer through a correction factor of f_{film} , especially at high temperature or high pH. Without the correction factors, the model has no capability to predict corrosion product films and the corresponding corrosion rates under film forming environments.

2.4.2 Netic Model (1996, 2001, and 2002)

This is a mechanistic model. The 1996 version is an electrochemical model with simplified mass transfer and chemical reactions. It was then developed to a complete model with electrochemical reactions, mass transport, and chemical reactions in 2001. The most recent development added iron carbonate film growth in 2002. Thus the model can simulate electrochemical reactions at the steel surface, chemical reactions in the liquid phase, diffusion of species to and from the bulk phase (the corrosion process leads to concentration gradients of species between the bulk and the steel surface), diffusion through porous corrosion films, and precipitation of iron carbonate in the corrosion film. The film growth makes the model unique in its kind.

Although the model has been successfully calibrated against some experimental data, it is still just a uniform corrosion model and cannot predict localized attack. In fact, localized corrosion prediction of mild steel in CO₂ service remains almost untouched in the open literature. Only Gunaltun (1996) proposed a localized corrosion prediction model by applying a turbulence factor to the general corrosion rate. Flow was assumed to be the main parameter to initiate localized attack. Obviously, there is not a fundamental understanding on localized corrosion, and this might be the reason that localized corrosion is very often described as a stochastic process.

CHAPTER 3: RESEARCH OBJECTIVES AND TEST MATRIX

3.1 Research Objectives

The present research is aimed at finding out when, why, and how localized corrosion occurs on carbon steels in CO₂ wet gas transportation. This includes:

- 1) Investigation of the effects of carbon dioxide partial pressure, temperature, pH, gas and liquid velocities, water chemistry (mainly the Cl⁻ concentration), flow regime, and oil/water ratio on the corrosion rate (both uniform and localized corrosion) along the top and the bottom of the line under low condensation rates wet gas conditions.
- 2) Investigation of the localized corrosion behavior of different mild steels (X-65 and C1018).
- 3) Development of a physico-chemical model to predict the likelihood or the risk of localized corrosion for both the top and the bottom of pipe in wet gas transportation conditions.

This physico-chemical model will be integrated into the existing OU Corrosion in Multiphase Flow modeling software package, in which the kernel is the Nesic (2001 and 2002) mechanistic CO₂ corrosion model. The model generated in this research will add the capability of predicting localized CO₂ corrosion risk of carbon steels into the software. The research also improves the fundamental understanding of localized corrosion, which is missing in the literature.

3.2 Test Matrix

The test matrix was designed to find the effect of each important parameter reviewed in chapter 2. The majority of experiments were conducted in a water-CO₂ system. The preliminary tests investigating various oil/water ratios were also covered.

Table 3.1 shows the experiment parameters and conditions.

Table 3.1 Test Matrix

Liquid phase	D.I. water with 0, 0.1, and 1% NaCl LVT 200 oil
Gas phase	CO ₂
Total pressure, bar	4.5, 7.9, 11.3, 14.8, 18.2
CO ₂ partial pressure, bar	3.8, 7.8, 10.6, 14.8, 18.2
Temperature, °C	40, 90
Water cut, %	100, 80
Superficial gas velocity (V _{sg}), m/s	5, 10, 15, 20
Superficial liquid velocity (V _{sl}), m/s	0.05, 0.1, 0.2
Flow regime	Stratified flow, annular flow
pH	as is, 5.2, and 6.2
Material tested	C1010, C1018, X65
Measurement techniques	ER, LPR, EIS, WL

It needs to be made clear that not all the combinations of parameters in Table 3.1 were covered. In order to identify how each parameter affects localized corrosion, only one parameter was varied at a time while keeping all the others at their reference values. The test matrix included several experimental series that were dedicated to the effect of temperature, pressure, Cl⁻, pH, flow, material, and oil presence on localized corrosion. Since various monitoring techniques were employed in the experiments, the comparison between the techniques will be given.

On the other hand, the test matrix was also designed to cover the conditions where corrosion product film is more or less likely to form. These conditions were selected

based on the literature data and the current understanding of CO₂ corrosion and through the interactions with the oil and gas industry, represented by the members of the advisory board of the Institute for Corrosion and Multiphase Technology at Ohio University.

CHAPTER 4: EXPERIMENTAL SETUP & PROCEDURE

In order to achieve the objectives set out in the previous chapter, a pilot scale flow loop was employed to simulate corrosion in gas production lines, which can generate different flow rates and regimes. The corrosion rates (both uniform and localized corrosion) were monitored and analyzed along both the top and the bottom of the line by using various monitoring and surface analysis techniques. This chapter is dedicated to the detail discussion of the experimental setup and procedures.

4.1 Description of The Flow Loop

A schematic diagram of this system is shown in Figure 4.1 and the flow loop photograph is shown in Figure 4.2 .

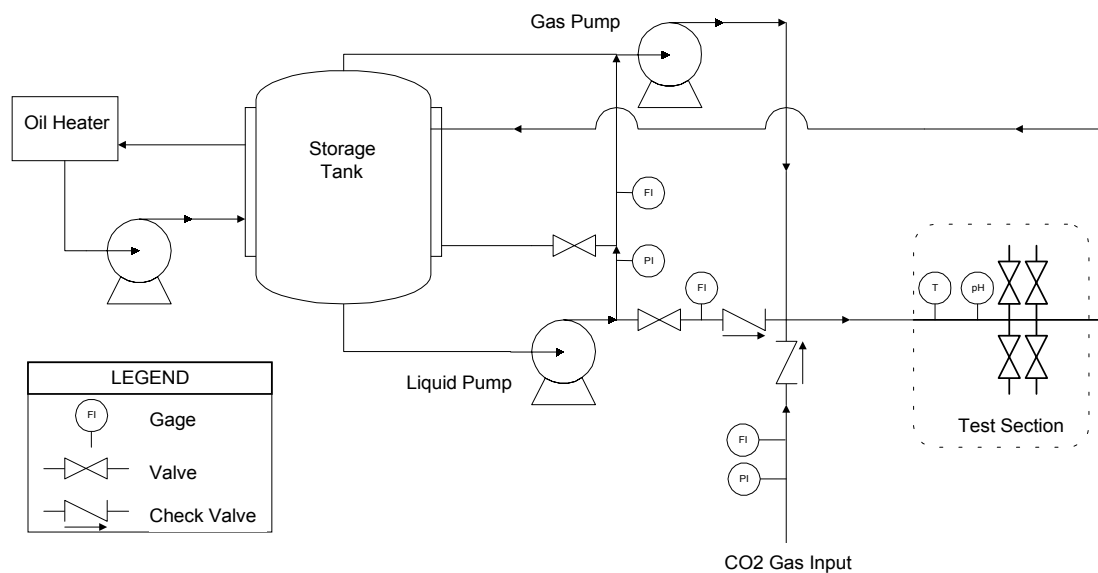


Figure 4.1 A schematic sketch of the test loop.



Figure 4.2 A photograph of the flow loop.

The flow loop is a 18-m long, 100-mm inner diameter, high pressure, high temperature, inclinable system. The entire flow loop is made from 316 stainless steel. A predetermined amount of liquid phase is stored in a 1.4 m³ tank which serves as a storage tank as well as a separation unit for the multiphase gas/oil/water mixture. The tank has a heating jacket and two 3 kW immersion heaters. Heating oil is heated in a separate heating tank using four 3.7 kW heaters and pumped through the heating jacket to heat the contents of the storage tank. Liquid is moved through this system by a stainless steel centrifugal pump. The flow rate is controlled within a range of 0 to 100 m³/hr with the variable speed pump controller in conjunction with a recycling stream. Liquid is also pumped through a 1-inch (2.54 cm) bleed line to the progressive cavity gas pump (PCP) for “lubrication.” This eventually flows back to the flow loop together with the gas. The flow rates in both the main line and the bypass line are metered with two inline turbine

meters. Manual controlled valves are installed in each stream so that they can be adjusted when needed.

A gas feed line at 2 MPa pressure supplies carbon dioxide gas from a 20,000 kg storage tank. In normal operation, gas is continuously circulated through the system at desired speeds by a PCP, driven by a variable speed motor through a reduction gear system. A cooling jacket was installed in the gas line inlet to allow the temperature control during the normal operation. An exhaust line with a “knock-out” drum is used to vent gas from the system when required.

4.2 Description of The Test Section

The test section is a 100 mm inner diameter, 2 m long schedule 80 stainless steel pipe. A schematic of the section is given in Figure 4.3, and a photograph is shown in Figure 4.4 .

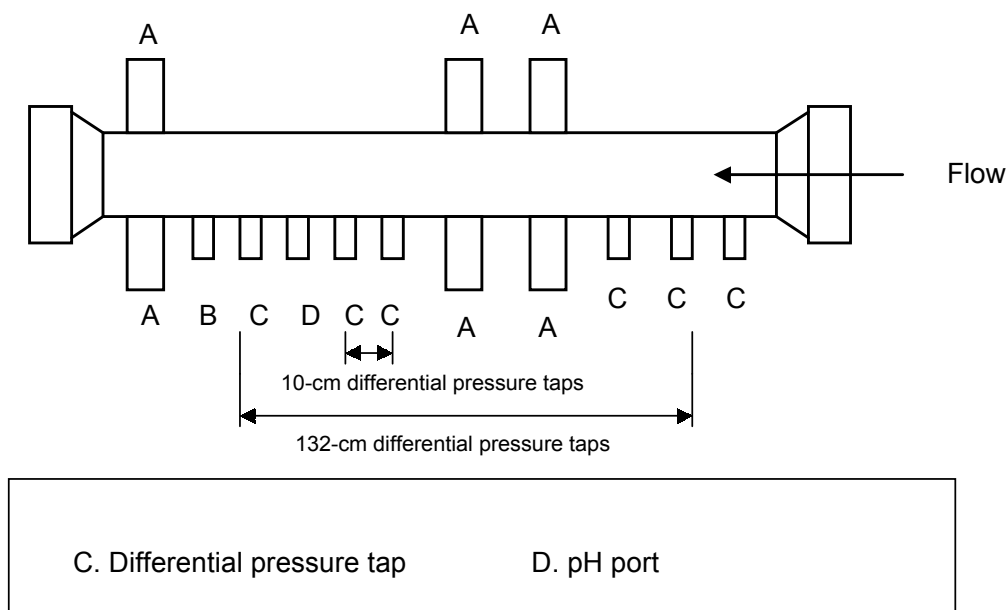


Figure 4.3 A schematic sketch of the test section.



Figure 4.4 A photograph of the test section.

Referring to Figure 4.3, three pairs of ports (A) at the top and at the bottom are used to insert flush-mounted electrical resistance (ER), linear polarization resistance (LPR), and weight loss (WL) probes for corrosion rate measurements. The pressure taps (C) are connected to pressure transducers and are used to measure the pressure drop for flow regime determination. The differential transducer taps were set up 7.0 m apart on the bottom of the pipe in this research. There are also ports for inserting a pH probe (D), a sampling tube (C) and a thermocouple (B). Upstream, 12 meters away from the test section, there is another thermocouple port. This construction allows the average condensation rate to be calculated. Half way through this research program, the original pH probe port was redesigned to enable simultaneous use of two pH probes side by side

in order to detect any possible drift. The new pH port configuration is shown in Figure 4.5 .



Figure 4.5 A photograph of pH measurement apparatus.

4.3 Experimental Procedure

The experimental system was filled with 300 gallons of deionized water or a NaCl solution (NaCl was in analytical grade). If LVT 200 oil was used in the test, the water cut was adjusted until the desired concentration was achieved. The system was then deoxygenated by flushing carbon dioxide through the system until the levels of dissolved oxygen were below 20 ppb. The system was then heated to the desired test temperature and pressurized with CO₂ to the test pressure. The liquid and gas pumps were then turned

on and the required flow rates were set separately. The pH was then adjusted by adding either NaHCO_3 or HCl (analytical grade) into the flow loop (the amount of chemicals needed were calculated by a self developed program). The gas and liquid flow settled for 16 meters before entering the test section where the corrosion measurements were performed and were then returned to the storage tank where the mixture was separated.

Before mounting the probes in the test section, all the coupon surfaces were prepared by wet grinding with silicon carbide paper up to 600 grit, rinsing with isopropyl alcohol, and then air-drying. The specimens earmarked for weight loss analysis were weighed and numbered. The coupons were introduced into the pressurized system and flush mounted into the test section under pressure and temperature without interrupting the steady state loop operation.

The tests lasted from a few hours for low temperature 40°C tests up to 200 hours for high temperature 90°C tests, and this was aimed at establishing a stabilized general corrosion rate in the presence of surface films. ER probes were used with an automatic data logging system for observing the data trends. At the same time, a model CK-3 Portable Corrosometer from Rohrback Corporation was also used for acquiring the data. LPR and electrochemical impedance spectroscopy (EIS) were measured by using a Gamry[®] CMS 300 corrosion monitoring system. The EIS technique was used only to measure and compensate for solution resistance. The weight loss specimens were weighed using a model 100 A XE series electronic balance from the Denver Instrument Company[®]. The pressure drop was measured by using a differential pressure transducer and recorded by in-house developed software. The pH was measured by an OAKTON[®]

pH 500 economy pH/mV/°C benchtop meter. The oxygen and dissolved iron levels were periodically monitored by using CHEMets® dissolved oxygen and iron test kits.

After each experimental run, the liquid and gas pumps were shut down and the system was depressurized gradually to 15 psig (~2 bar) in half an hour. The ER, LPR, and WL probes were then taken out of the test section and immediately rinsed with isopropyl alcohol. The probe surfaces were then examined visually and recorded by using an Olympus® D-600L digital camera. For weight loss measurement studies, the specimens were pickled in an inhibited 10% hydrochloric acid (10 g/l Hexamethylenetetramine in 10% HCl solution) to remove the scale, then neutralized in alkali, rinsed with distilled water and alcohol, air dried, and weighed to measure mass loss. The specimen was then examined under a Metallurgical Microscope (MM) for localized attack measurements.

For morphology studies, the specimens were examined using a scanning electron microscope/energy dispersive spectrometer (SEM/EDS) and X-ray diffraction (XRD). Some specimens were prepared for cross section analysis to examine the corrosion product film thickness and morphology. A metallurgical microscope or SEM was used to generate photographs of the cross section.

4.4 Corrosion Monitoring Techniques

4.4.1 Uniform corrosion measurements

Electrical Resistance(ER) Technique.

The ER technique is essentially a metal loss measurement method. Thus it is applicable to virtually all types of corrosive environments. The working principle of the

ER probe is that the electrical resistance of the metal element is inversely proportional to its thickness. The electrical resistance of a metal or alloy element is given by:

$$R = r \cdot \frac{L}{A} \quad (4-1)$$

where: L = element length; A = cross sectional area, and r = specific resistance. Therefore, the reduction (metal loss) in the element's cross section due to corrosion will be accompanied by a proportionate increase in the element's electrical resistance (Jones, 1996).

The ER probe used in this research was manufactured by Metal Samples[®], and the configuration of the probe is shown in Figure 4.6. The material was made from C1010 steel, and the composition of this material is given in Table 4.1.

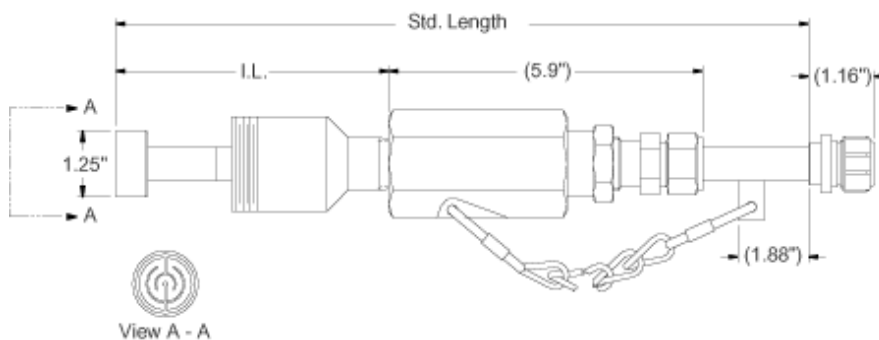


Figure 4.6 Retractable flush element electrical resistance probe (www.metalsamples.com).

Table 4.1 Chemical composition of type C-1010 carbon steel (wt.%) (Fe is in balance).

Al	As	B	C	Ca	Co	Cr	Cu	Mn	Mo	Nb
0.053	0.004	0.0009	0.13	0.003	0.002	0.016	0.010	0.27	0.003	<0.001
Ni	P	Pb	S	Sb	Si	Sn	Ta	Ti	V	Zr
0.013	0.006	<0.001	0.008	0.001	0.023	0.001	0.006	0.002	0.002	0.001

Three different sensitivity probes, S-20, S-10 and S-5, were used in this work. They represent element thicknesses of 20, 10, and 5 mils, respectively with the useful probe life of 10, 5, and 2.5 mils corresponding to 0.254, 0.127, and 0.0635 mm. The following relationship (mainly the unit conversion) was given to calculate the corrosion rate with the readings obtained from the probe:

$$CR\left(\frac{mm}{y}\right) = \frac{\Delta probe\ reading \times 24 \times 365 \times probe\ span(mils)}{\Delta Time(hrs.) \times 1000 \times 40} \quad (4-2)$$

where probe span = 2.5 for S-5 probe
 = 5 for S-10 probe
 = 10 for S-20 probe

The selection of the probe size is a compromise between the sensitivity and the probe life. The latter is dependent upon the corrosion rate. The S-5 probe has the highest sensitivity but the shortest life span, thus it was used when the corrosion rate was expected to be low; the S-20 probe has the longest life span but the lowest sensitivity, and it was used when the corrosion rate was expected to be very high.

Coupon Weight Loss (WL) Technique.

The specimens used in the experiments were circular coupons with a diameter of 11.6 mm and a thickness of 3.2 mm as indicated in Figure 4.7 . Two types of carbon steel were used in the tests: typical construction grade 1018 carbon steel (microstructure after etching shown in Figure 4.8) and 5L X-65 low carbon steel, which is frequently used in the oil and gas industry as principle pipeline steel (microstructure after etching shown in Figure 4.9). The chemical composition for each material is shown in Table 4.2 and Table 4.3.

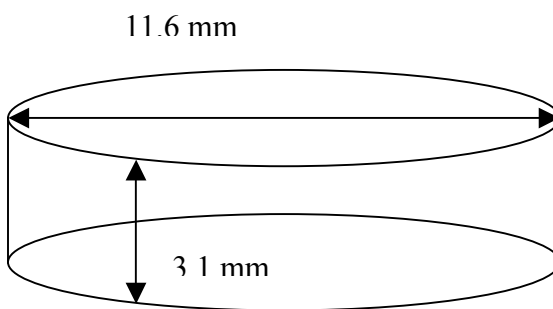


Figure 4.7 The diagram of the specimen.

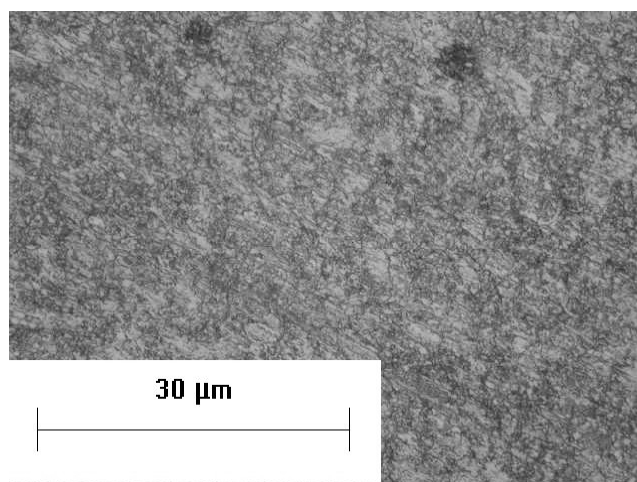


Figure 4.8 The optical microstructure of type C1018 material (500x).

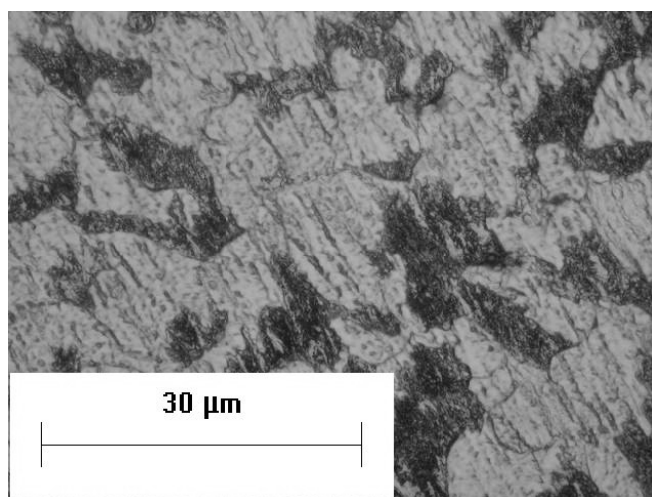


Figure 4.9 The optical microstructure of 5LX65 material (500x).

Table 4.2 Chemical Composition of C-1018 Carbon Steel (wt.%) (Fe is in balance).

Al	As	B	C	Ca	Co	Cr	Cu	Mn	Mo	Nb
0.08	0.006	0.0009	0.20	0.001	0.011	0.061	0.028	0.90	0.018	0.014
Ni	P	Pb	S	Sb	Si	Sn	Ta	Ti	V	Zr
0.044	0.017	0.032	0.012	<0.001	0.044	0.011	0.023	0.005	0.004	0.007

Table 4.3 Chemical Composition of 5LX65 Steel (wt.%) (Fe is in balance).

Al	As	B	C	Ca	Co	Cr	Cu	Mn	Mo	Nb
0.001	0.01	0.0007	0.16	0.001	0.019	0.017	0.062	0.80	0.016	0.010
Ni	P	Pb	S	Sb	Si	Sn	Ta	Ti	V	Zr
0.025	0.014	0.017	0.026	0.017	0.055	0.006	0.013	<0.001	0.002	0.006

The coupon holder can hold four coupons at a time, as shown in Figure 4.10 .

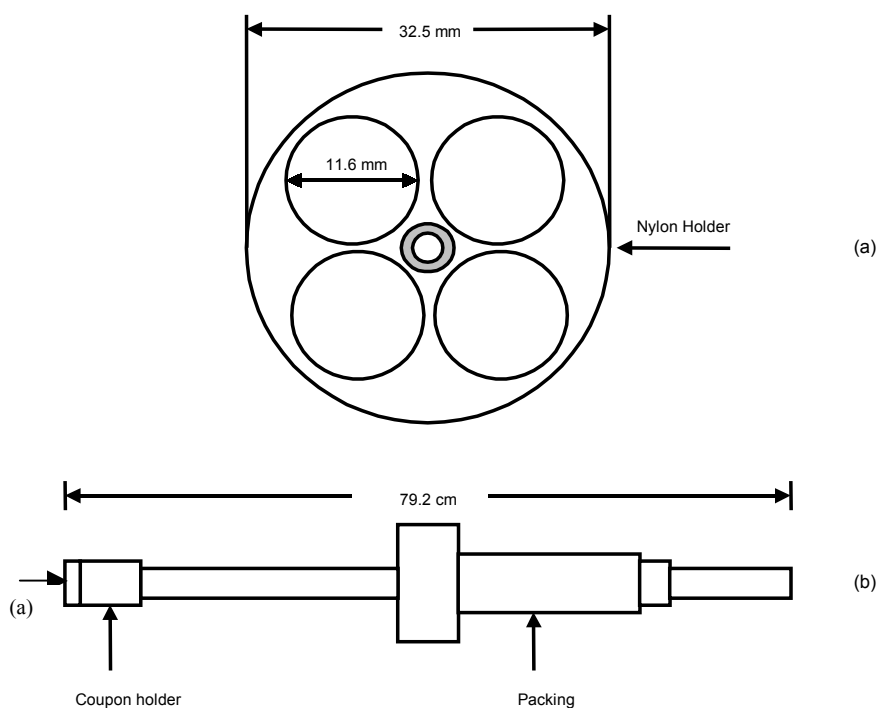


Figure 4.10 (a) Four coupon holder; (b) Coupon holder probe.

After the experiments, the coupons were removed from the system, cleaned, and then subjected to further analysis. It should be noted that the *in-situ* WL corrosion rate measurement is not possible. The corrosion rate from WL indicates the average corrosion rate over the exposure time. The corrosion rate from a weight loss coupon method is determined as follows:

$$CR_{aver} = \frac{(WL) \times 24 \times 365 \times 10}{D \times A \times T} \quad (4-3)$$

where, CR_{aver} = average corrosion rate in mm/year;

WL = coupon weight loss in grams;

D = density of the coupon in gm/cm³;

A = coupon surface area exposed for corrosion in cm²;

T = time taken for corrosion in hours.

Linear Polarization Resistance (LPR) Technique.

LPR is an electrochemical technique used to monitor the *in-situ* corrosion rate. From basic electrochemical theory, the corrosion current density i_{corr} (in A/m²) can be described as:

$$i_{corr} = \frac{\beta_a \beta_c}{2.303(\beta_a + \beta_c)} \cdot \frac{1}{R_p} \cdot \frac{1}{A} \quad (4-4)$$

where, β_a and β_c are the temperature dependent anodic and cathodic Tafel constants. In this work, $\beta_a = 0.042$ V and $\beta_c = 0.123$ V were used at a temperature of 40°C, $\beta_a = 0.0487$ V and $\beta_c = 0.1437$ V were used at a temperature of 90°C according to well-established experimental work (Nesic et al., 1994). R_p is the corrosion resistance in Ohm, which can be obtained by polarizing the electrode surface using a potentiostat. A is the working

electrode surface area in m^2 . The corrosion rate (CR) in mm/yr can then be calculated according to the following equation:

$$CR = \frac{m}{At\rho} = \frac{i_{corr}M_w}{\rho nF} = 1.16 i_{corr} \quad (4-5)$$

where, m is the metal loss in kg, t is the test time in seconds, ρ is the density of the material in kg/m^3 , M_w is the molecular weight of iron, F is Farady's constant, and n is the number of electrons exchanged in the electrochemical reaction.

A three-electrode concentric ring probe manufactured by Metal Samples[®] was employed to perform the LPR analysis and is shown in Figure 4.11 . The inner and middle rings were made from C1018 carbon steel and served as the reference and working electrodes respectively; the outer ring served as the counter electrode and was made from 316 stainless steel. A ± 5 or ± 10 mV overvoltage was applied during the LPR measurements with respect to the open circuit potential. It should be noted that the resistance measured with the LPR technique is a total resistance, which was compensated for the solution resistance measured by electrochemical impedance spectroscopy techniques.

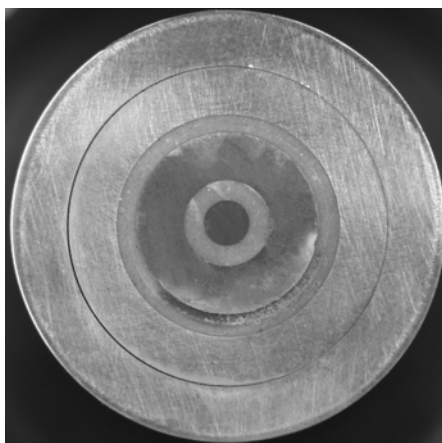


Figure 4.11 Replaceable flush-mount element of LPR probe.

Electrochemical Impedance Spectroscopy (EIS) Technique.

EIS technique was used only to obtain the solution resistance to compensate the total resistance measured in LPR measurements. The same probe and data acquisition system was used as employed for LPR measurements. The measurements were carried out at the open circuit potential with a superimposed AC potential (amplitude of 4 mV AC and frequency: 5000 - 0.1 Hz).

4.4.2 Localized corrosion measurements

Metallurgical Microscope (MM).

The three methods described above are not adequate for localized corrosion evaluation. When a small weight loss is concentrated in a few pits, very large depth penetration (localized corrosion rate) can be achieved and can produce failure. Thus, when localized attack (pitting) exists, maximum pit depth measurements are needed. One way to do this is to examine the whole specimen after film removal under a metallurgical microscope, using the calibrated fine focus to determine depth difference between surface and pit bottoms. The corrosion rate with maximum pit penetration depth can be calculated as follows:

$$CR_{\max} = \frac{P \times 10^{-3} \times 24 \times 365}{T} \quad (4-6)$$

where, CR_{\max} = corrosion rate (maximum pit penetration rate) in mm/yr;

P = maximum pit penetration depth in μm ;

T = test duration time in hours.

The localized corrosion rate is the sum of this pit penetration rate and the average corrosion rate.

To quantify the extent of pitting as compared to general (uniform) attack, a pitting factor can be used (Jones, 1996). It is defined as follows:

$$f = \frac{CR_{\max}}{CR_{\text{aver}}} \quad (4-7)$$

where, f = pitting factor;

CR_{\max} = maximum pit penetration rate in mm/yr;

CR_{aver} = average corrosion rate by specimen weight loss measurement in mm/yr.

A pitting factor of unity indicates uniform corrosion. However, a pitting factor of infinity, which is inappropriate for cases where general penetration is very low or near zero.

In addition, pit density (or spacing in number of pits/m²), surface size (surface opening), and depth can be compared using standard charts (Jones, 1996). However, full evaluation by this procedure is tedious and time consuming for any significant number of specimens. Thus it is rarely used to evaluate the localized corrosion.

Scanning Electron Microscopy (SEM).

Another way to obtain the maximum pit penetration rate is through SEM cross-sectional analysis that is done without the removal of the corrosion product film. Since only one cross-sectional area is examined, the success of this technique largely depends on whether a deepest pit can be picked up when performing the cutting/polishing process. If the pits are small and covered by corrosion product, then it is very possible to miss the

deepest pits by randomly choosing the cross section. Generally, in this study from each experiment, one specimen surface was examined under MM without the surface film and another one was examined under SEM in cross section. The reported maximum localized corrosion rate was selected based on the larger of the two measurements.

4.5 Corrosion Product Film Morphology Studies

4.5.1 Surface morphology and microstructure

Two instruments were employed in the morphology and microstructure studies. One is a Nikon[®] inverted metallurgical microscope EIPHOT 200, and the other is a JSM 5300 scanning electron microscope/energy dispersive spectroscopy (SEM/EDS). With the latter instrument, the area to be examined is irradiated with a finely focused electron beam at 30 kV. The spot size and the current density of the beam are adjusted with the help of the lens system so as to obtain good quality images without damaging the specimen. Once the area of interest on the specimen is selected, the magnification, brightness, and focus are adjusted and a picture is stored on the computer attached to the microscope.

4.5.2 Surface composition analysis

Three tools were used to examine the corrosion product film composition: EDS, X-ray diffraction (XRD), and X-ray photoelectron spectroscopy (XPS). For some specimens, EDS was applied to obtain information about impurities deposited on the specimen surface. Unfortunately, EDS cannot yield information about the composition of the corrosion product since this particular instrument cannot detect carbon and oxygen

accurately. The EDS used in this work can only detect elements of atomic number 12 or above in the Periodic Table. XPS analysis for some specimens was done in the Physics Department at Ohio University. For the majority of the experiments, XRD was used to identify the corrosion products on the specimen surface, and thus more attention is given to this technique below.

X-ray Diffraction (XRD) Analysis and Validation for The Current Research.

A Rigaku X-ray Diffractometer was used in this research. X-ray tube power was set up at 40 kV and 30 mA respectively during the data acquisition process. Each element or compound with its characteristic structure could be examined by X-ray. A validation test was performed by exposing a steel plate holder without any treatment directly under XRD detection. The result is shown in Figure 4.12. The composition of the top layer was mainly Fe_3O_4 and Fe_2O_3 as expected. These well-known iron oxides exist where steel has been exposed to humid air for a long time.

XRD can analyze both single and multi crystal structure samples. For the specific shape of the specimen used in this research, a special specimen holder had to be made to fit within the instrument. An aluminum holder was used at first. A blank specimen that had been ground with silicon carbide paper up to 600 grit was tested by using this holder. The result is shown in Figure 4.13. The two biggest peaks match both the iron and aluminum characteristic Bragg angles. The other two small peaks were identified as alumina. This means that the XRD analysis includes some information from the holder, which may cause errors in further analysis with complex compounds.

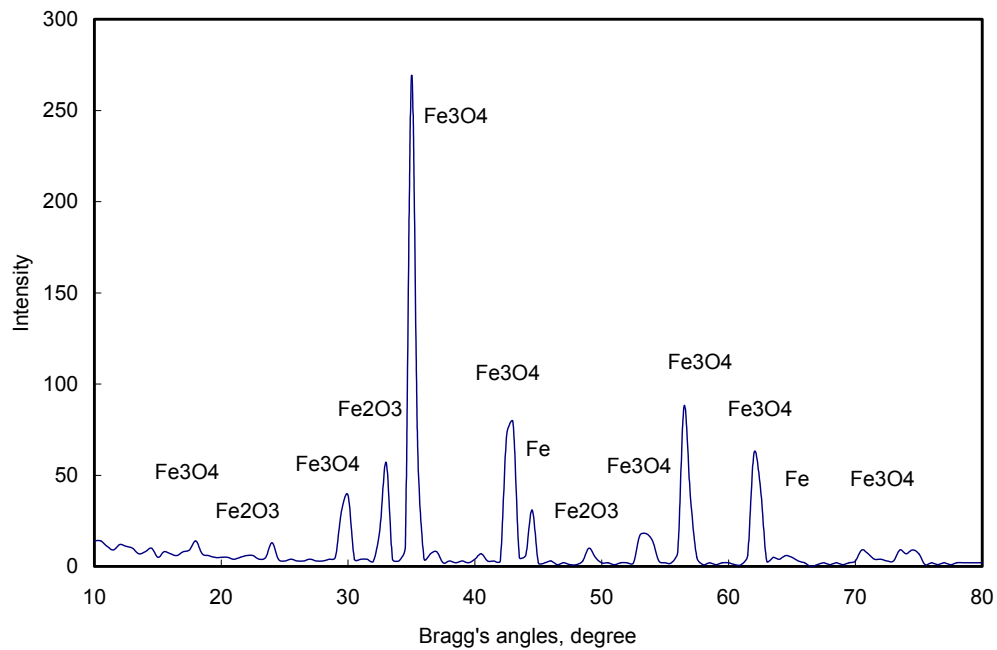


Figure 4.12 A steel plate under XRD.

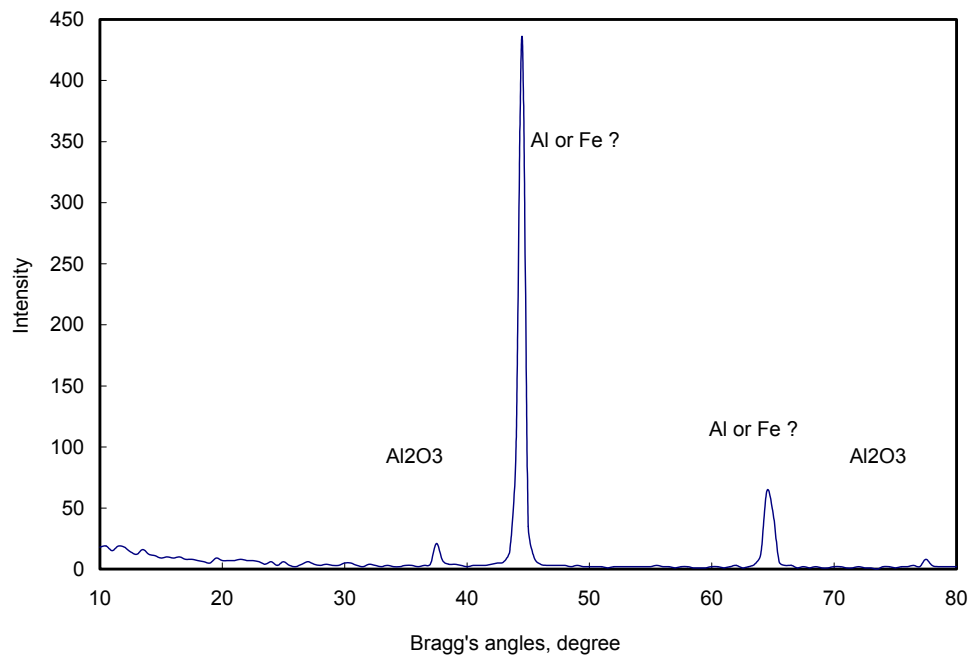


Figure 4.13 A blank specimen with aluminum holder under XRD.

Thus the aluminum coupon holder was replaced with a plastic holder. The result with the plastic holder is shown in Figure 4.14.

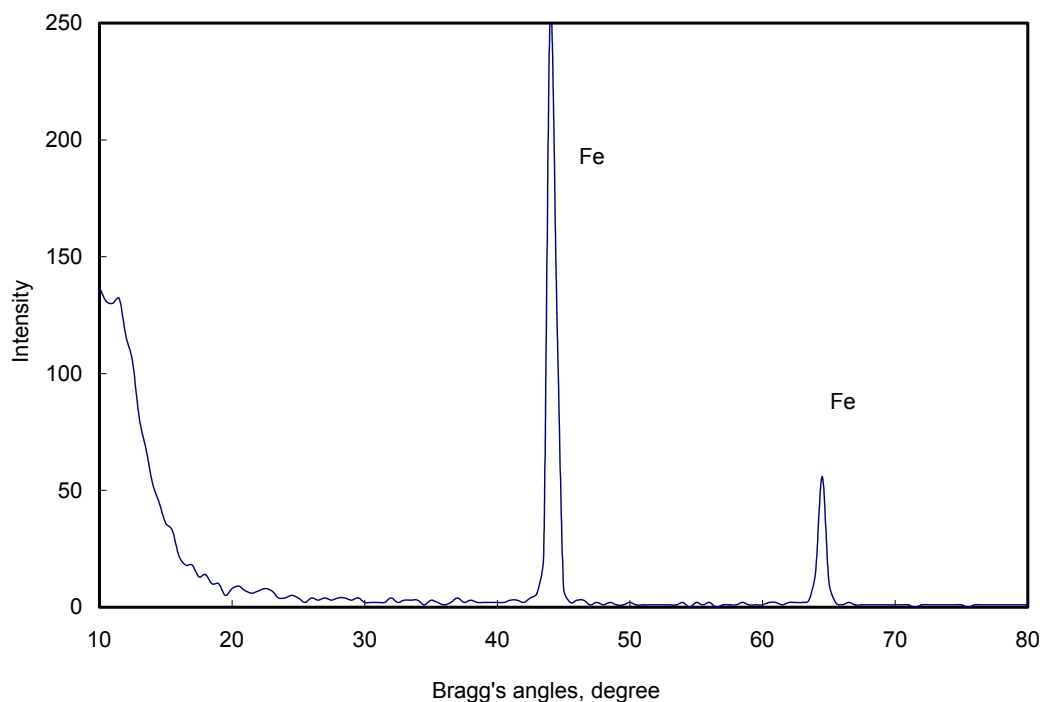


Figure 4.14 A blank specimen with plastic holder under XRD.

Only two peaks were seen, and they were identified as iron peaks. The plastic holder was then chosen for the following analysis. It was noticed that all the peaks appearing in Figure 4.12 through Figure 4.14 did not exactly exhibit the corresponding Bragg angles. There is a repeatable degree of deviation for every peak identified. This is due to the depth of the slot within the holder being not exactly at the right height, which caused the angle of X-ray penetration to deviate. However, this would not significantly affect the results related to the composition of the corrosion product film.

4.5.3 Cross-sectional analysis

Either a MM or a SEM was used to generate the cross section photographs for the specimen. The cross-section specimen preparation was performed by cutting the specimen in half first and then embedding them initially in mottled Bakelite powder. The grinding procedure was taken by dry grinding with silicon carbide paper up to 600 grit and then polished with 1 μm alumina. Later on in the research for specimens having a surface film, a better procedure was adopted by embedding the whole specimen in a resin first in order to fix the film in place, and then cutting the specimen in half and grinding with silicon carbide paper. It needs to be stressed that the grinding direction has to be perpendicular to the film growth direction. Otherwise, the corrosion product film can be “rolled over” and damaged by grinding process.

4.6 Difficulties, Solutions, and Lessons to Be Learned

Running a high pressure, high temperature pilot-scale flow loop in laboratory is never an easy job. A tremendous amount of problems and difficulties followed the experimental programs, which by and large were related to the failures in engineering, technology, and communication procedures. The author here documents these difficulties with the aim to instruct later researchers in this area.

The major source of the difficulties was from the progressive cavity pump used to move the gas. The pump is shown in Figure 4.15. This multiphase pump worked as a gas pump with only a limited amount of water to provide lubrication. Several pump failures occurred during the experiments and several actions taken to solve the problems caused

new problems. The most significant problems related to the gas pump are listed as follows.



Figure 4.15 Moyno-“Tri phase system” multiphase progressive cavity pump.

Lead Contamination.

Serious lead contamination in the flow loop was encountered several times in the early stages of the experimental program. This might have caused erroneous measurements and degraded the reliability of localized corrosion information obtained during those experiments. A detailed investigation was performed on the source of the lead and how it might affect the corrosion (Sun, 2001).

Briefly, the lead came from the primary and secondary bronze thrust plates used in the gas pump, which was made mainly from copper and lead (83% copper and 17% lead). The problem was solved after the bronze thrust plate was coated with Teflon. Results presented thereafter were obtained with the lead-free system.

Grease Contamination, Iron Contamination, and Gear Balls.

Grease was used to lubricate the gear balls of the PCP when replacing the parts after wear or breakage. It was found thereafter that a black sticky material coated the pipe wall and contaminated the whole system. This mysterious contaminant was a very effective corrosion inhibitor and greatly affected the real corrosion rate measurements. The grease was suspected to be the initiator and was confirmed later by examining the pump again. Several parts of the gas pump are shown in Figure 4.16.

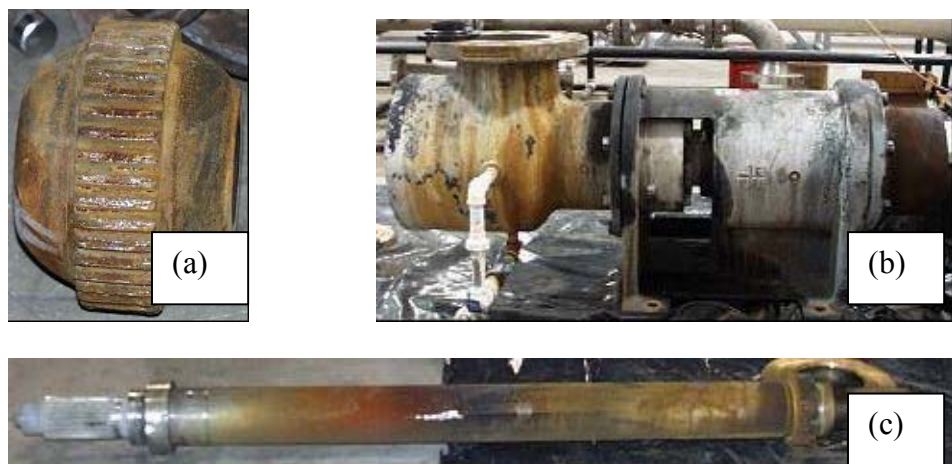


Figure 4.16 Parts of the gas pump. (a) gear ball; (b) suction housing; (c) connecting rod.

In Figure 4.16, the connecting rod (between the two gear balls) showed the iron oxide concentration gradient across the drive shaft. The suction housing of the Moyno “gas” pump is 304 stainless steel, and all wetted parts are stainless steel. There are two gear ball joints (made from carbon steel) that are used to connect the motor to the rotor because the rotor end moves up and down and does not stay centralized like a normal shaft. The gear balls are isolated from the fluid by a rubber seal, which is made from

buna N rubber. The problem with the gear joint seal arises with the rapid increase and decrease in system pressure during the deoxygenation process. An increase in pressure migrates carbon dioxide and some liquid into the gear ball location. Heat liquefies the grease within the gear joint, and then depressurization causes the carbon dioxide to expand and push the grease out of the gear joint into the flow loop. Quick depressurization creates a pressure drop across the gear joint seal so great that it bursts the rubber. As the process is repeated, grease is added to the system. The effect of system fluids entering the gear ball location was the corrosion of the gear balls and an increase of iron in the flow loop. Thus the gear balls wore more quickly due to corrosion, but a major concern was the uncontrolled amount of iron and grease added to the flow loop during the pressurization and depressurization process.

A large scale cleaning procedure was applied to remove the grease contamination from the rig. LVT oil was first used to clean out the grease, then a detergent was used to clean out the LVT oil, and finally water was used to clean out the detergent. Although significant effort had been put into cleaning the rig, the contamination was so severe that several sections of pipe had to be taken apart and physically cleaned.

Thus, attention has to be paid during rapid depressurizing of the system since it can cause wetting of the carbon steel gear balls and high dissolved iron content in the flow loop as well as the migration of grease into the loop. The processes that involve rapid depressurization are mainly the deoxygenating process, start up, and shut down.

Rubber Entrainment.

The aforementioned rubber seal for the gear balls could be torn off and moved into the system. However, the major source of the rubber entrainments was from the rubber liner of the PCP stator. Large rubber chunks were found in the flow loop and the storage tank. From time to time the rubber clogged the flow meter and the experiments were stopped.

The bolts and nuts used to keep the gas pump together were occasionally not tight enough, and vibration caused the bolts to loosen and fall inside the gas pump between the rotor (made from stainless steel) and stator (made from carbon steel and coated with rubber). With the pump running, the bolt sheared off large pieces of rubber inside the stator. A long deep trail on the rubber stator was observed after taking the gas pump apart at one occasion.

High Iron Concentration.

All the loop components are made from stainless steel, which is considered to be resistant to CO₂ corrosion. During the experiments, a high iron concentration was observed several times without deliberately adding any iron sources. This could not be explained by the corrosion of probes and coupons. The above-mentioned carbon steel gear ball corrosion was one of the sources of high iron concentrations (during the depressurization process). Another major source was not recognized until the PCP pump failed one day. The failure structure is shown in Figure 4.17.

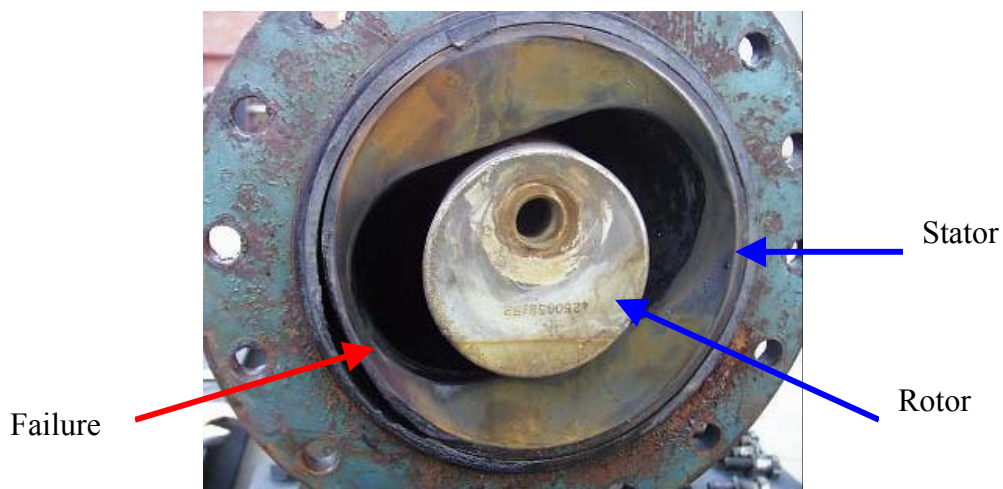


Figure 4.17 A stator failure in the gas pump.

A delaminated rubber stator created a gap between the rubber and mild steel stator. The system fluid migrated into the gap and corroded the mild steel, causing a high iron concentration in the loop. It was difficult to identify this problem during normal operation. However, one should be aware that any unusual phenomena are the mirror of the abnormal events, some of which were mentioned above. After replacing the delaminated stator and by careful depressurization of the system, no unwanted major dissolved iron concentration increase was observed.

LPR Measurements on Top of The Line.

The major measurement difficulty was applying the LPR technique to the top of line corrosion measurement. It was found that the open circuit potential (OCP) on top of the line was difficult to stabilize and fluctuated within a large range. This made the LPR technique difficult to apply and the corresponding data unreliable. The reason is not understood. However, the liquid droplets entrained in the gas phase were suspected to be

the main reason for the variation of OCP. Droplets could have impacted onto the electrode surface to cause an unstable OCP value even in the annular flow regime due to the very thin liquid film on the top of the line. Also, the electrode may have experienced intermittently dry and wet situations. The majority of the LPR data on the top of the line was not used due to their uncertainty.

CHAPTER 5: EXPERIMENTAL RESULTS AND DISCUSSIONS

As discussed in the previous chapters, the experiments were designed to meet the research objectives and find the effect of major factors that affect the wet gas corrosion. Based on the literature review in Chapter 2, a few hypotheses were formulated as follows: a). Only uniform corrosion at a high rate takes place when there is no corrosion product film formation; b). Only uniform corrosion at a low rate exists when a fully protective film is formed; c). Localized corrosion may occur when non-protective corrosion product films form.

A fully protective film was considered to form only when a corrosion rate below 0.1 mm/yr was achieved. The experiments discussed below attempted to cover the above three situations to either validate or invalidate the hypotheses. This chapter is dedicated to discussing the measured effects of each individual parameter on wet gas corrosion, especially on localized corrosion.

5.1 Baseline Test Establishment And Validation

5.1.1 Objectives

Before running any experiments, a suitable baseline experiment had to be chosen to serve as a reference point. The baseline experiment has to be relatively simple, easy to perform, and comparable to the recognized literature. Once the baseline result is established, whenever the experimental system encounters problems and uncertainties, one can fall back on the baseline test to try and resolve them. Also, the results obtained here can be compared to the other literature data to show where the current results fit into

the overall picture. Based on these considerations, a single-phase test was chosen as a baseline, and the experimental parameters are shown in Table 5.1.1.

Table 5.1.1 Test matrix for baseline experiment

Liquid phase	D.I. water with 1% NaCl
Temperature	40±1°C
CO ₂ partial pressure	4.38 bar
Total pressure	4.45 bar
Superficial liquid velocity (V _{sl})	1 m/s
Superficial gas velocity (V _{sg})	0 (single phase full pipe flow)
pH	As measured, around 3.9
Dissolved iron concentration	As measured, less than 10 ppm
Dissolved oxygen concentration	As measured, less than 20 ppb
Techniques used	ER (C1010), WL (C1018), LPR (C1018)

There are three pairs of ports in the test section (three at the top and three at the bottom of the pipe). Since the experiment was run at full pipe flow conditions, the difference in corrosion rate from the top to the bottom of pipe was expected to be insignificant. Thus two probes were used to collect the data for each technique. At the same time, another high pressure, high temperature flow loop with the same pipe I.D. was used to validate the baseline corrosion rate. The test was expected to last for 24 hours or whenever the corrosion rate was stabilized. Surface analysis was applied on some of the specimens to examine whether the corrosion product film had formed.

5.1.2 Results and Discussions

Figure 5.1.1 shows the trend of the corrosion rate during the baseline experiment in a wet gas system. The test was forced to stop due to a sudden power off, which resulted in 9 hours of data in the ER measurement, 6 hours in the LPR measurement, and

11 hours in the WL measurement. It is seen that the corrosion rate was not fully stabilized and still mildly increasing after a few hours exposure.

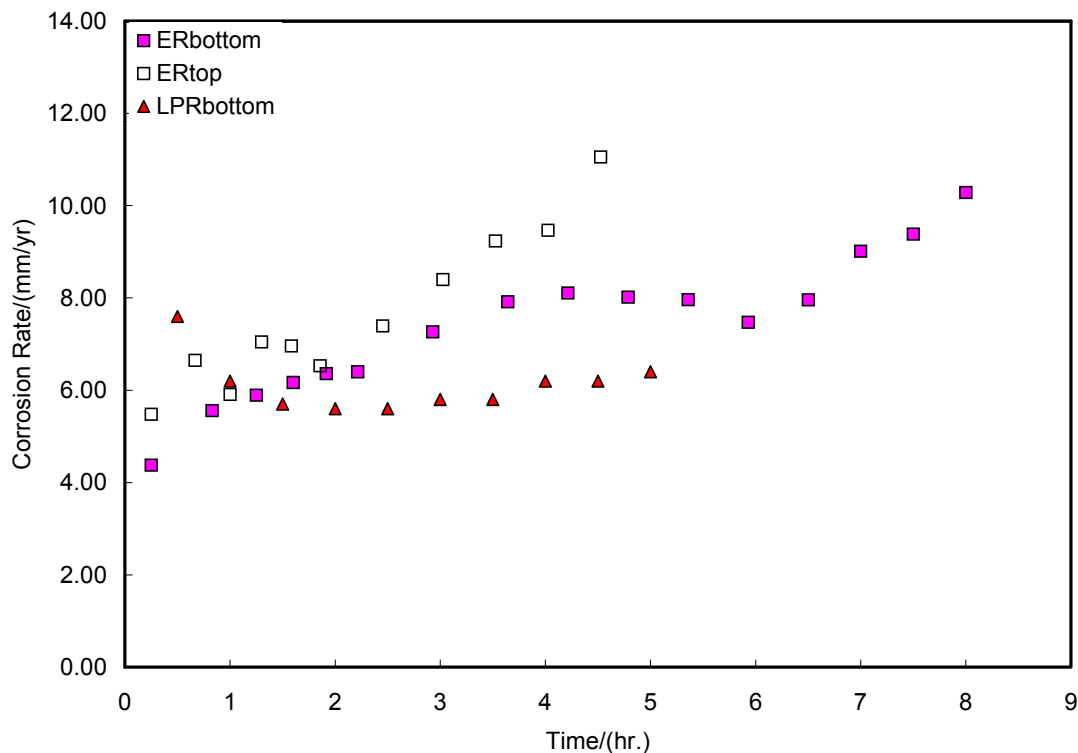


Figure 5.1.1 The change of corrosion rate with time for the single-phase flow test in the wet gas system with 1% NaCl at $T = 40^{\circ}\text{C}$, $P = 4.45$ bar ($P_{\text{CO}_2} = 4.38$ bar), and $V_{\text{sl}} = 1$ m/s.

In order to compare the results from ER and LPR with WL, the data in Figure 5.1.1 was integrated over the test time to obtain the average corrosion rate, as shown in Figure 5.1.2. The error bars in the data series represent the total uncertainty of the experimental error for the ER and the LPR measurements, which is calculated and discussed in detail in Appendix B. Since multiple specimens (8) were used for WL measurement in the same experiment, the error bar for the WL analysis represents the standard deviation from the experimental data.

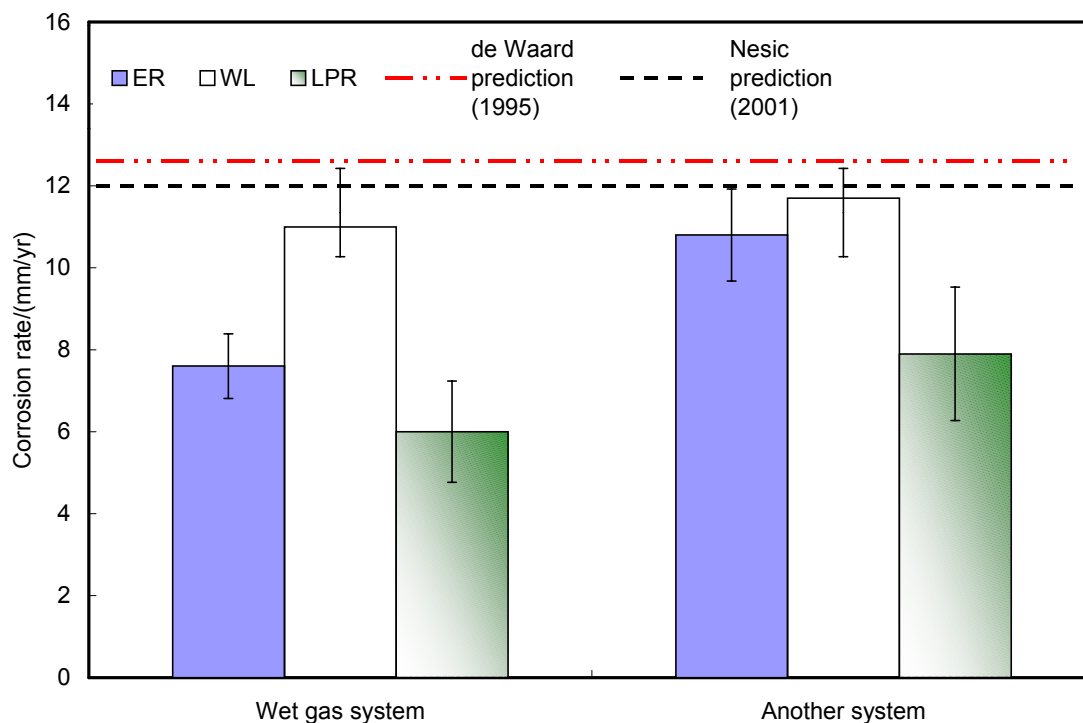


Figure 5.1.2 Measured and predicted corrosion rate using different techniques from two flow loops with 1% NaCl at $T = 40^{\circ}\text{C}$, $P = 4.45$ bar ($P_{\text{CO}_2} = 4.38$ bar), and $V_{\text{sl}} = 1$ m/s.

It is seen that the corrosion rate measured by the three techniques are of the same order of magnitude, although the WL results were somewhat higher than ER and LPR. All of them show a high corrosion rate. For the LPR measurement, the temperature-dependent Tafel constant was chosen as described in chapter 4, which is $\beta_a = 0.042\text{V}$ and $\beta_c = 0.123\text{V}$, according to Nescic et al (1994).

A parallel test in a different flow loop lasted 24 hours. The data shown in Figure 5.1.2 for the second system agreed well with the baseline system data. The two flow loop results were still considered to be comparable, taking the test time difference into consideration.

The two well-known corrosion prediction models gave good predictions for the baseline experiments. The de Waard, et al. (1995) model predicted the corrosion rate to be 12.3 mm/yr, and the Nesic, et al. (2001) model predicted 12 mm/yr. Thus the baseline experiment was established and validated, giving us confidence to proceed with the more complicated testing in two-phase flow.

5.1.3 Surface Analysis

After the specimens were taken out of the test section, visual observation identified a black, fragile film covering all of the specimen surfaces. The film was very easy to remove by simply spraying alcohol on the surface. The XRD analysis, shown in Figure 5.1.3, detected only substrate iron on the specimen.

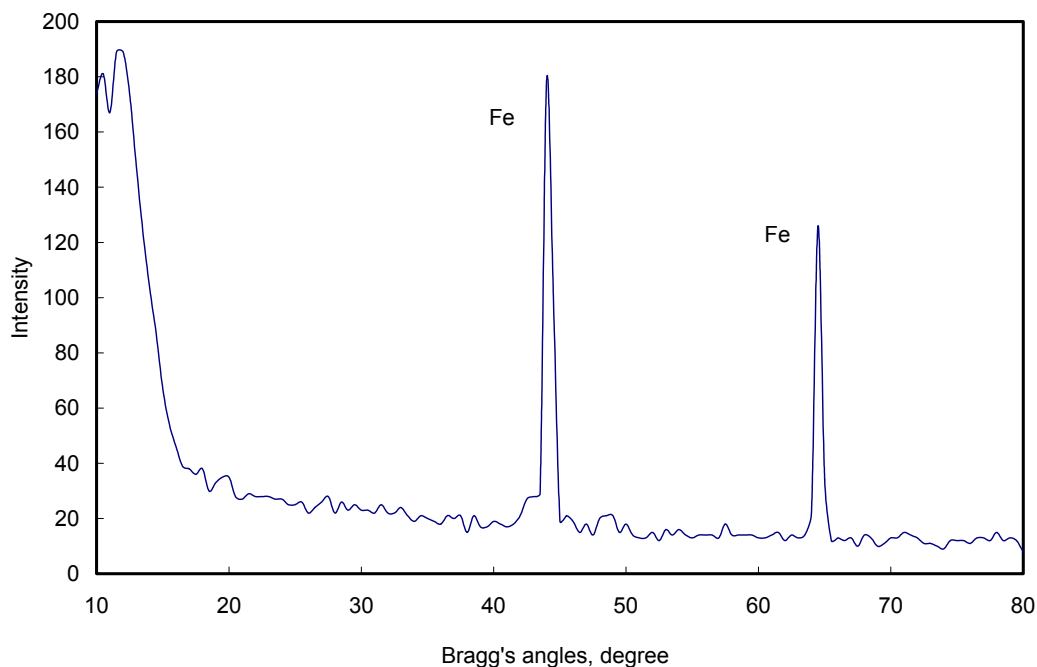


Figure 5.1.3 XRD analysis on the specimen without film after the baseline test with 1% NaCl at $T = 40^{\circ}\text{C}$, $P = 4.45$ bar ($P_{\text{CO}_2} = 4.38$ bar), and $V_{\text{sl}} = 1$ m/s.

On a carefully preserved specimen with an intact film, XRD detected iron carbide (Fe_3C), as shown in Figure 5.1.4. No iron carbonate film peaks were identified, and the detected high intensity peaks were iron carbide and substrate iron. The findings are in a good agreement with what has been reported in the literature (Olsen and Dugstad, 1991, Dugstad, 1992, Nestic and Lunde, 1994).

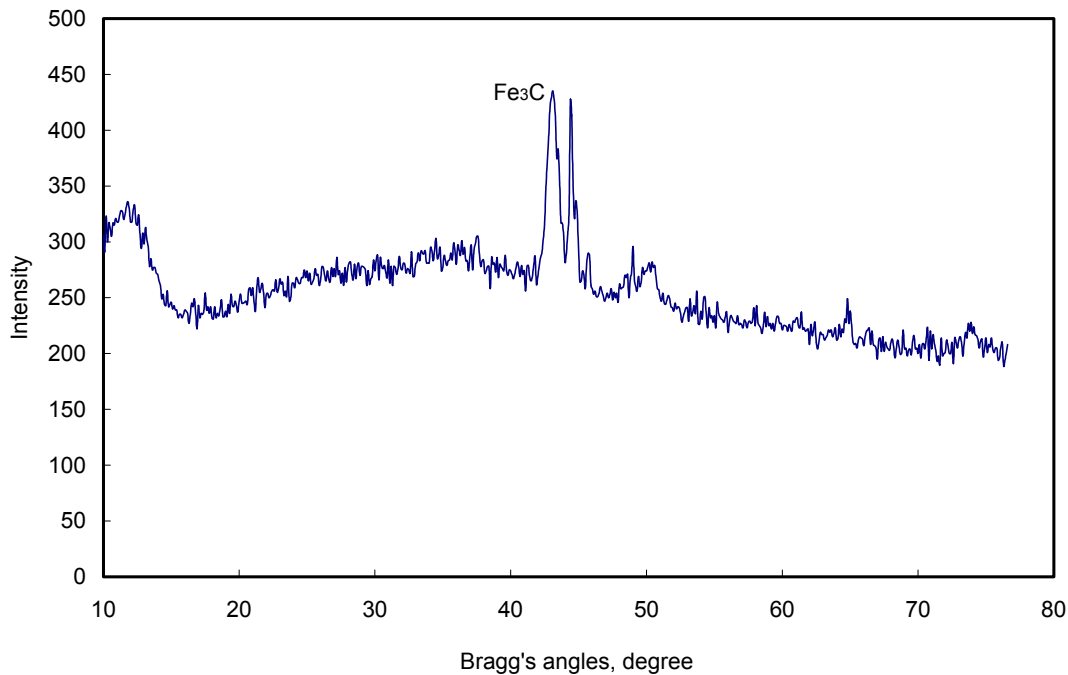


Figure 5.1.4 XRD analysis on a specimen with film after the baseline test with 1% NaCl at $T = 40^\circ\text{C}$, $P = 4.45$ bar ($P_{\text{CO}_2} = 4.38$ bar), and $V_{\text{sl}} = 1$ m/s.

5.2 The Effect of Temperature in Wet Gas Flow

Temperatures of 40°C and 90°C were chosen to test the effect of temperature on localized corrosion. The results from ER measurements are compared in Figure 5.2.1 (Localized corrosion was measured using MM).

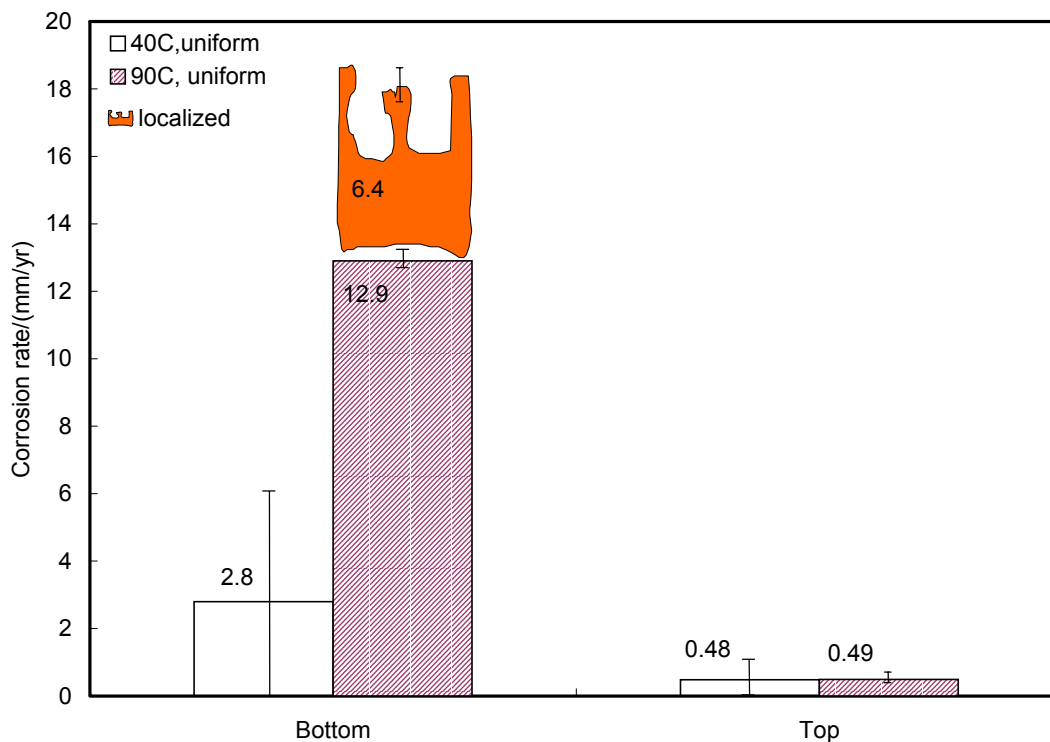


Figure 5.2.1 The effect of temperature on wet gas corrosion at $V_{sl} = 0.1$ m/s, $V_{sg} = 10$ m/s, and $P_{total} = 4.5$ bar ($P_{CO_2} = 3.8$ bar) with D.I. water only.

It is seen that localized corrosion did not occur at 40°C on either the top or the bottom of the pipe. However, at 90°C, localized corrosion on the bottom of the pipe occurred, and no localized corrosion at the top was observed. Thus the experiments were focused more on the high temperature test in the following discussions.

It was observed that the corrosion rate changed greatly from 40°C to 90°C for the bottom of the pipe. The corrosion rate increased with the increase in temperature due to the higher reaction rate at higher temperature. In this particular test, a corrosion product film had formed at 90°C, as indicated in

Figure 5.2.2. The specimen surface was totally different from the blank specimen (shown in Figure 5.2.3 for comparison) and covered by a crystal layer, which was identified later as FeCO_3 (XRD results shown in Figure 5.2.4). However, the corrosion product film formed at this condition had some local defects and failures and was non-protective. The corrosion rate remained high at over 12 mm/yr, and localized corrosion was initiated at the sites of local film failure.

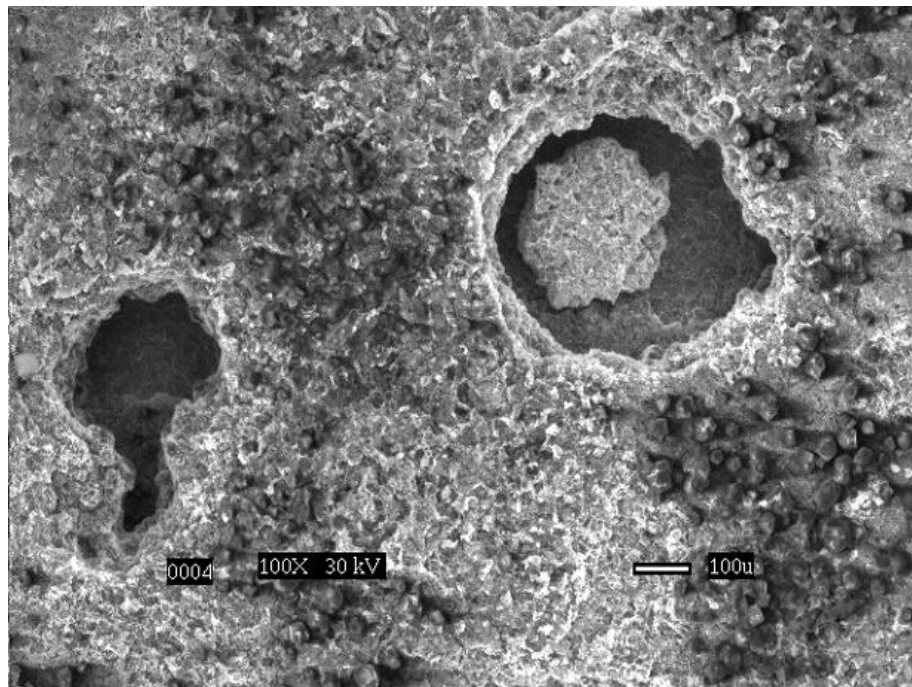


Figure 5.2.2 SEM surface morphology for 90°C bottom C1018 specimen at $V_{sl} = 0.1$ m/s, $V_{sg} = 10$ m/s, and $P_{total} = 4.5$ bar ($P_{CO_2} = 3.8$ bar) with D.I. water only.

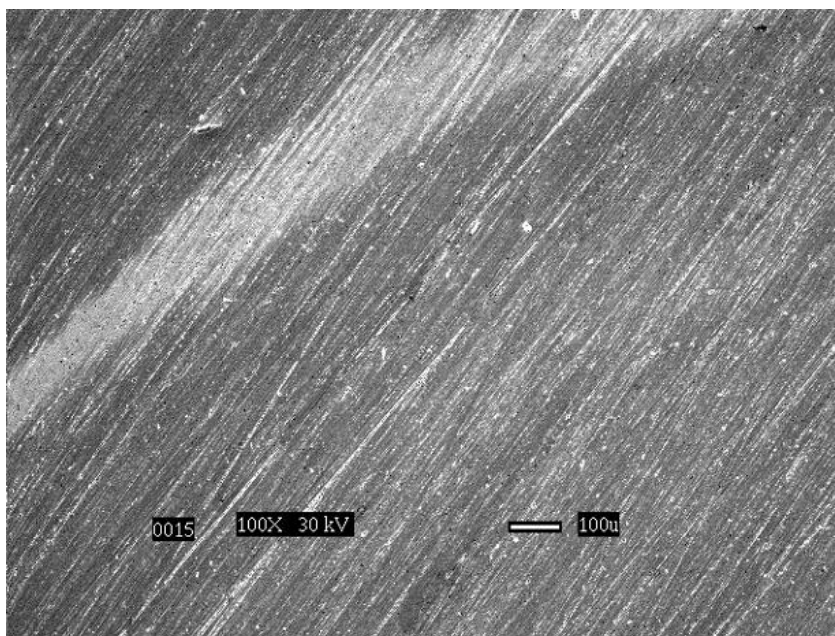


Figure 5.2.3 SEM surface morphology for blank C1018 specimen without exposure to corrosion.

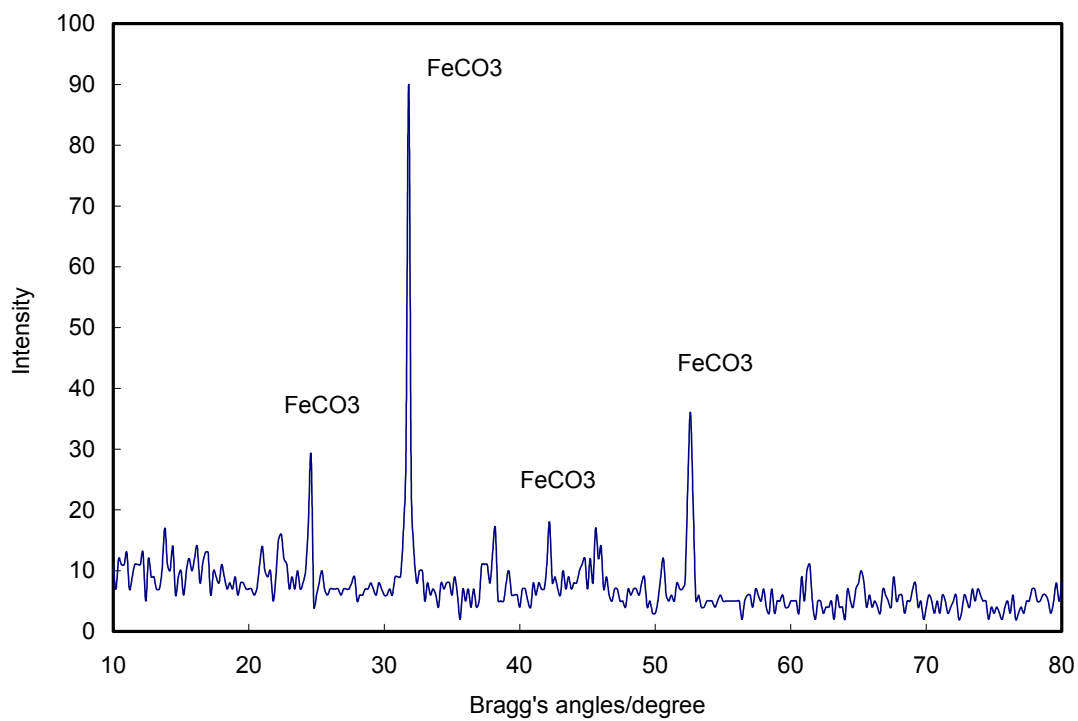


Figure 5.2.4 XRD spectrum for 90°C bottom C1018 specimen at $V_{sl} = 0.1$ m/s, $V_{sg} = 10$ m/s, and $P_{total} = 4.5$ bar ($P_{CO_2} = 3.8$ bar) with D.I. water only.

The corrosion rate at the top of the pipe did not vary much with the change of the temperature. At the test conditions, the flow was in the stratified flow regime. In this regime, some condensation occurs, the pipe was insulated, and liquid droplets entrained in the gas phase can impact the top of the pipe wall. At 40°C, the condensation on the top of the pipe was almost negligible (Vitse, 2002). Thus it is speculated that the corrosion rate was mainly contributed due to the liquid droplets impinging on the wall, as the condensed water is more corrosive. At 90°C, even if the condensation rate was higher, the small amount of water on the top might have soon become saturated by the corrosion product due to the higher reaction rate and lower solubility of FeCO_3 at this temperature. Thus the corrosion rate shows a larger difference between the top and bottom at 90°C compared to 40°C under stratified flow conditions. Further discussion about “where the water is from” on the top of the line is given in the following sections.

The error bars were evaluated by experimental uncertainty analysis described in Appendix C. The uniform corrosion rate was measured from the ER technique. It is obvious that the uncertainties in the measurement at 40°C were much larger than the uncertainties at 90°C. The 40°C test corresponded to a few hours exposure time while the 90°C test was over 100 hours. Besides the test duration time, the corrosion rate was also a major factor affecting the assessed experimental error. Generally, a higher corrosion rate, longer test time, higher sensitivity of the probes, and more stable test temperature give less variability and more accurate corrosion rates. In essence, the absolute corrosion rate taken for only a few hours through the ER technique needs to be treated extremely carefully especially when low corrosion rates are involved. The experimental error due to

the technique could be so large as to render the results useless. To improve the accuracy of the test results, one can extend the test time, repeat the test multiple times, or use multiple probes and techniques to achieve more accurate results.

5.3 The Effect of Cl⁻ Ions in Wet Gas Flow

Cl⁻ ions can initiate localized corrosion typically in the form of pitting corrosion for steels that generally have a passive film, for example, stainless steel and nickel alloys. The research on carbon steel, which is considered to be a general corrosion material, has rarely been touched. Although the majority of wet gas transportation comes with a very low salinity liquid phase, which is composed of condensed vapor phase, some wells produce a small amount of formation water together with the gas, which can contain high Cl⁻ concentrations (up to 1 wt. %, Gunaltun, 2001). Thus a series of tests on Cl⁻ concentration were performed ranging from 0 to 1% (wt.%). The test matrix for the Cl⁻ series is shown in Table 5.3.1.

Table 5.3.1 Test matrix for the effect of Cl⁻ on localized corrosion.

Liquid phase	0, 0.1%, 1% NaCl
Total pressure	4.5 bar
CO ₂ partial pressure	3.8 bar
Temperature	90°C
Superficial gas velocity	10 m/s
Superficial liquid velocity	0.1 m/s
Material	C1018, X65, and C1010
Measurement techniques	ER, LPR, and WL

5.3.1 Results On The Effect Of Cl⁻

Test with no NaCl in the flow loop

In the test without Cl⁻, the pH and dissolved iron content increased with time as shown in Figure 5.3.1. The exact same trend for both ferrous iron concentration and pH suggests that the rise of the pH was due to the corrosion (iron dissolution) process. The solution was under-saturated at the beginning of the test, but reached super saturation (SS) at the end, as indicated by Figure 5.3.1.

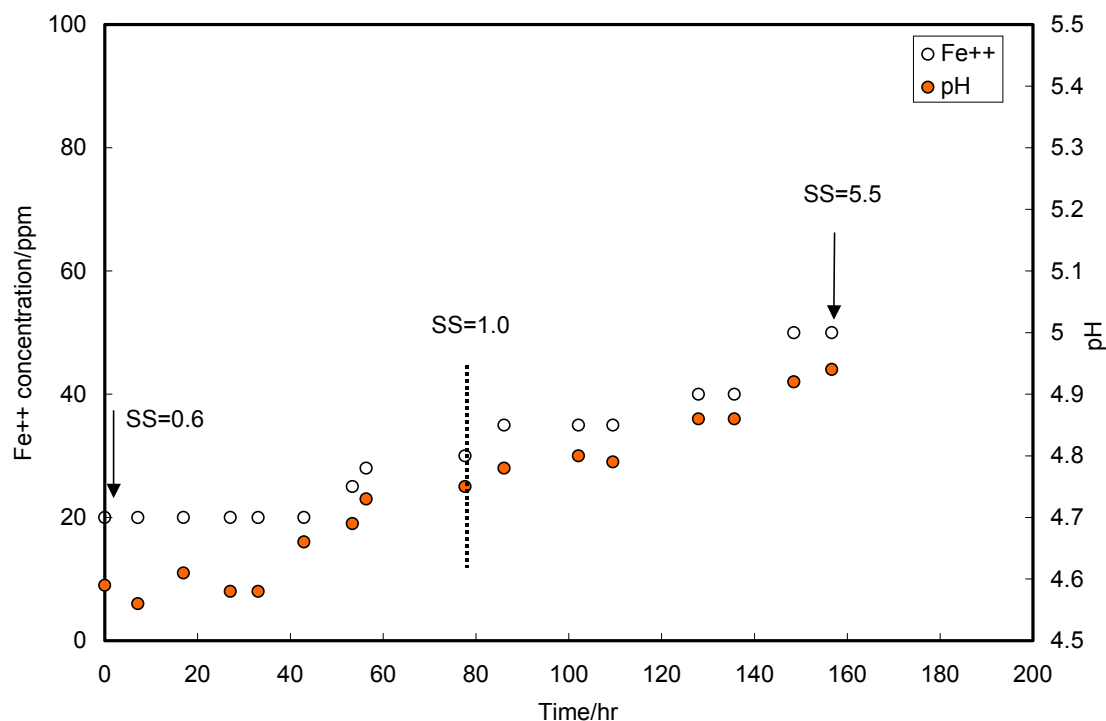


Figure 5.3.1 The change of bulk pH and Fe^{2+} with time for 0.0% Cl^- solution at $V_{\text{sg}} = 10$ m/s, $V_{\text{sl}} = 0.1$ m/s, $T = 90^\circ\text{C}$, and $P = 4.5$ bar ($P_{\text{co}_2} = 3.8$ bar).

Figure 5.3.2 shows the time evolution of the uniform corrosion rate from ER and LPR measurements. In this particular test, the two techniques gave very different results. For example, at the bottom of the pipe, the corrosion rate measured by ER remained high for the whole duration of the experiment, while the LPR showed a relatively high corrosion rate at the beginning, but a stabilized low corrosion rate at the end of the test, indicating the formation of a protective film. The two techniques showed a corrosion rate difference of two orders of magnitude.

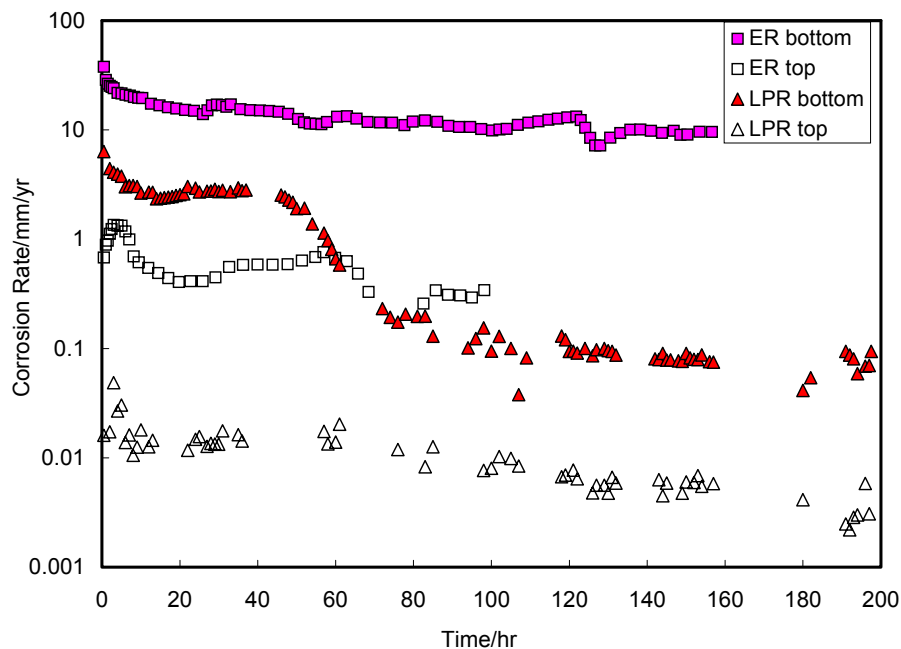


Figure 5.3.2 The change in corrosion rate with time for 0.0% Cl solution at $V_{sg} = 10$ m/s, $V_{sl} = 0.1$ m/s, $T = 90^{\circ}\text{C}$, and $P = 4.5$ bar ($P_{\text{CO}_2} = 3.8$ bar).

The third technique, WL, was also used in the test. The integrated corrosion rates for LPR and ER over the entire period of time are shown in Figure 5.3.3 together with the WL results. It is seen that the WL method indicated high corrosion rates at the bottom for both materials, C1018 and X-65. The results from WL are in good agreement with those from ER.

The specimen was visually examined after the experiment and no localized attack was observed. However, microscopy inspections revealed that a highly spread non-uniform attack did occur on both materials, as shown in Figure 5.3.4. In fact, hills and valleys, and sometimes mesa attack, occupied the whole specimen surface. It is estimated that 50% of the surface area was covered by grooves. The height difference between the

“hills” and “valleys” is described as the magnitude of the localized corrosion rate in this paper, and the value is added in Figure 5.3.3 on top of the uniform corrosion rate.

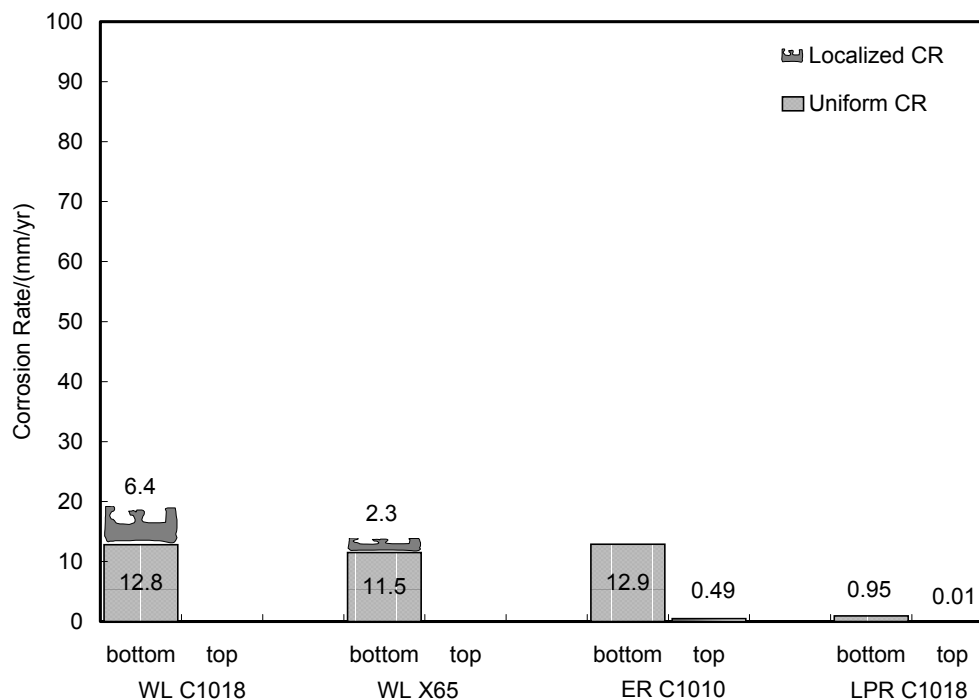


Figure 5.3.3 Average and localized corrosion rate (LC) from different methods for the experiment without Cl^- at $V_{\text{sg}} = 10 \text{ m/s}$, $V_{\text{sl}} = 0.1 \text{ m/s}$, $T = 90^\circ\text{C}$, and $P = 4.5 \text{ bar}$ ($P_{\text{CO}_2} = 3.8 \text{ bar}$).

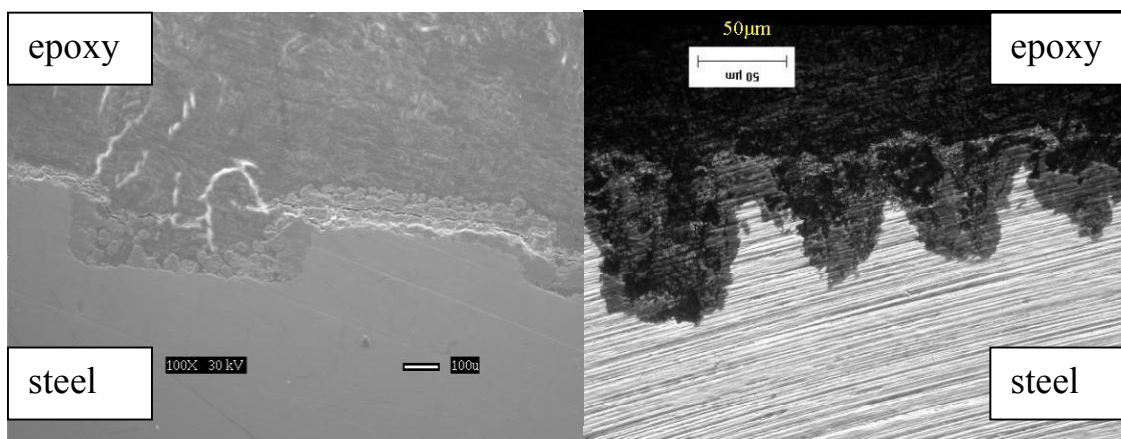


Figure 5.3.4 Cross sections for 0.0% Cl^- solutions at $V_{\text{sg}} = 10 \text{ m/s}$, $V_{\text{sl}} = 0.1 \text{ m/s}$, $T = 90^\circ\text{C}$, and $P = 4.5 \text{ bar}$ ($P_{\text{CO}_2} = 3.8 \text{ bar}$). left: bottom C1018; right: bottom X-65.

Test with 0.1% NaCl

Similarly to the test without NaCl, in this test the pH and dissolved iron content increased during the test, as shown in Figure 5.3.5. The solution again started out as under-saturated and ended up being super-saturated. Figure 5.3.6 shows the change of uniform corrosion rate with time measured by ER and LPR. At the beginning of the test, both ER and LPR bottom gave the same corrosion rate results. But after an initial period of time, LPR bottom showed a greatly decreased corrosion rate again and finally stabilized at a much lower value compared to the ER method, as happened in the test without Cl⁻. The corrosion rate on the top, measured by the ER method, shows high corrosion at the beginning and then decreased to a relative stable and small value in a short time. Although the solution resistance was greatly decreased by adding NaCl, the top LPR measurements were not stable. This suggests that the water on the top was predominantly from condensation. The corrosion rates have orders of magnitude differences between the bottom and top, which is reflected in all three measurement techniques, as shown in Figure 5.3.7. Weight loss results are more comparable to ER results, while LPR deviates from the other two methods. However, there is a major difference in this test compared to the previous test with no NaCl. Some localized attack in the form of pitting or mesa corrosion was found on the bottom of the C1018 steel coupons (see Figure 5.3.8). X-65 was still attacked by non-uniform corrosion and has the similar very rough surface as observed in the test without NaCl. The top specimen of both materials was well protected by thin films, and no localized corrosion was found. This can be seen by cross-sectional analysis shown in Figure 5.3.8.

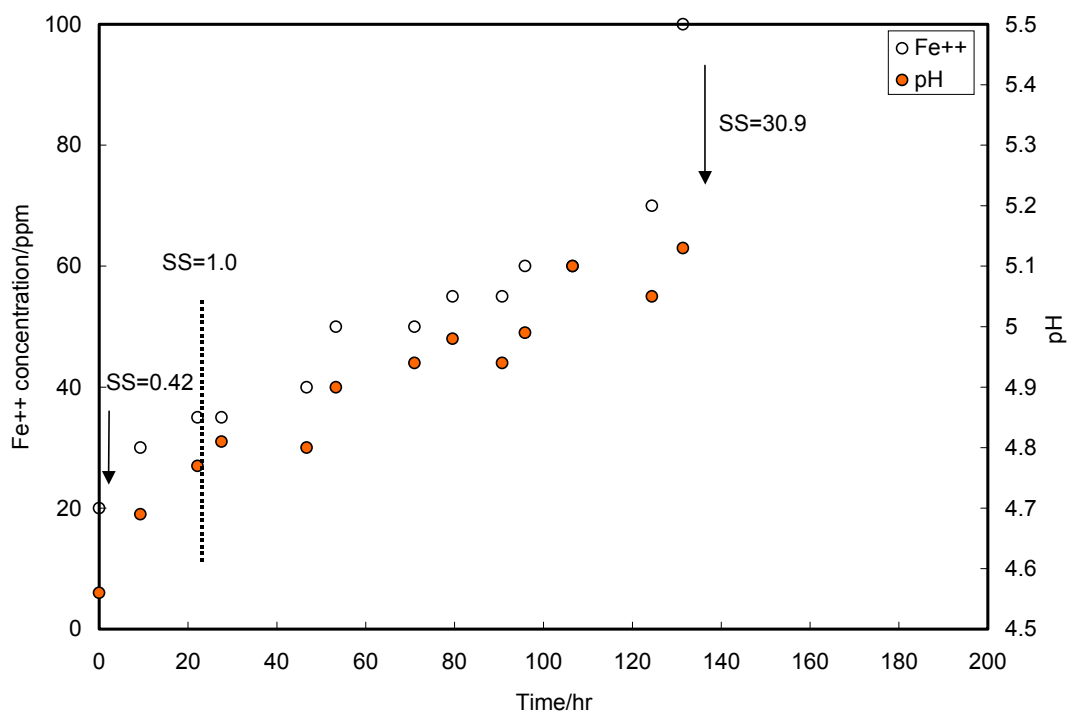


Figure 5.3.5 The change of pH and Fe^{2+} with time for 0.1% NaCl solutions at $V_{sg} = 10$ m/s, $V_{sl} = 0.1$ m/s, $T = 90^\circ\text{C}$, and $P = 4.5$ bar ($P_{\text{CO}_2} = 3.8$ bar).

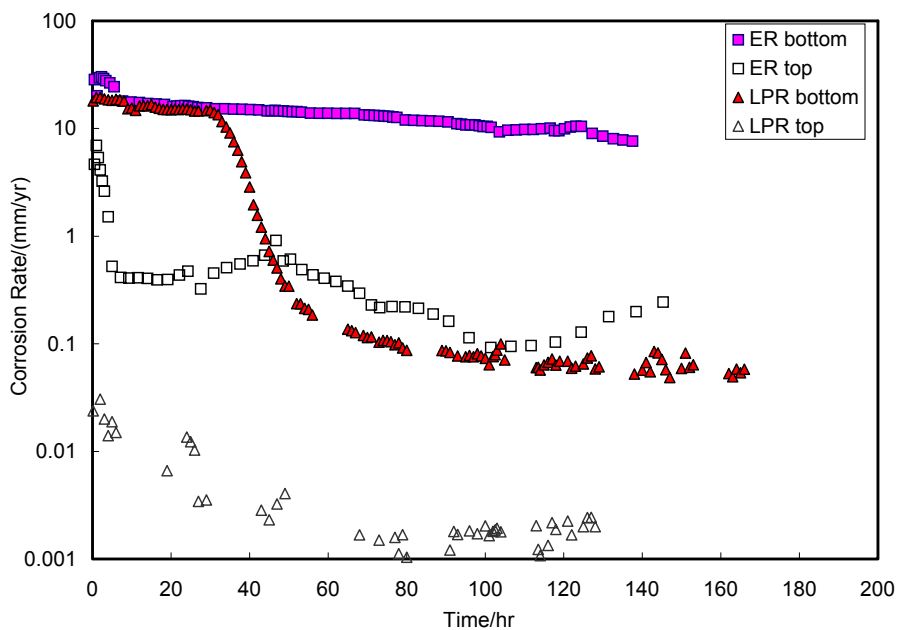


Figure 5.3.6 The change of corrosion rate with time for 0.1% NaCl solutions at $V_{sg} = 10$ m/s, $V_{sl} = 0.1$ m/s, $T = 90^\circ\text{C}$, and $P = 4.5$ bar ($P_{\text{CO}_2} = 3.8$ bar).

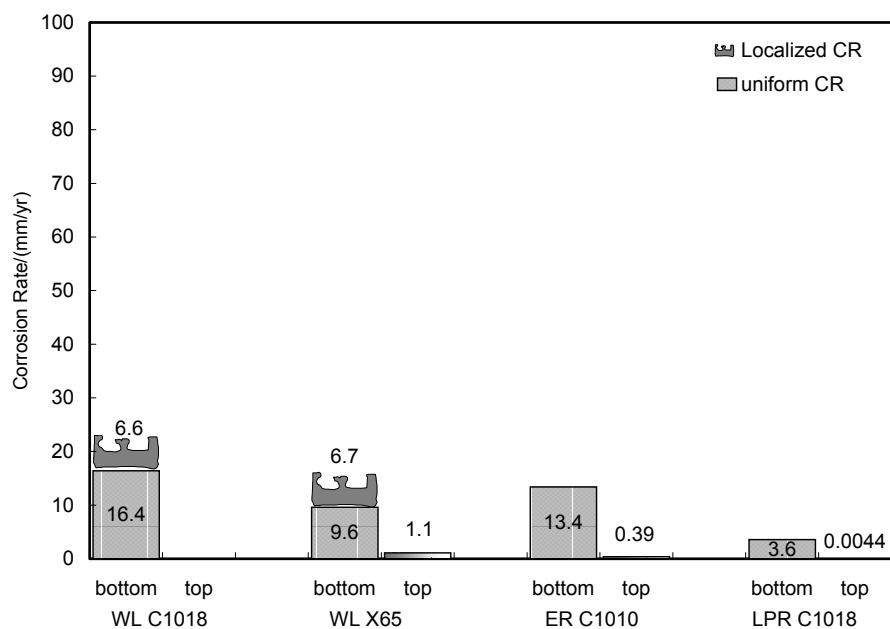


Figure 5.3.7 Average and localized corrosion rate (LC) from different methods for 0.1% NaCl solutions at $V_{sg} = 10$ m/s, $V_{sl} = 0.1$ m/s, $T = 90^{\circ}\text{C}$, and $P = 4.5$ bar ($P_{\text{CO}_2} = 3.8$ bar).

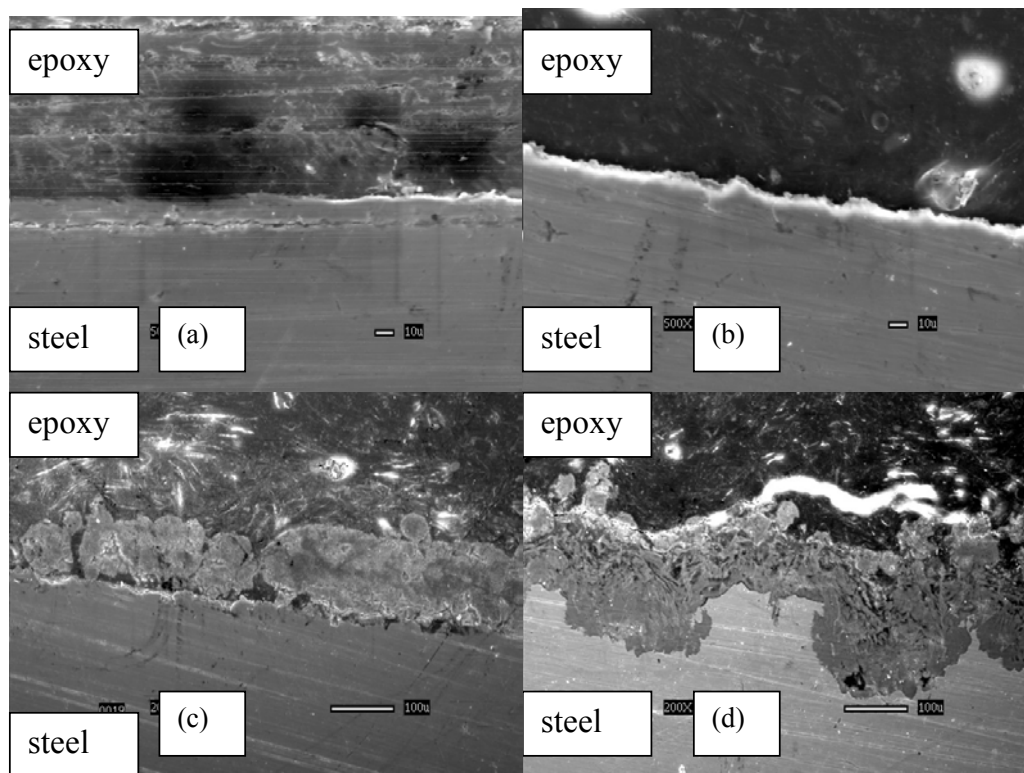


Figure 5.3.8 Cross sections for 0.1% NaCl solutions at $V_{sg} = 10$ m/s, $V_{sl} = 0.1$ m/s, $T = 90^{\circ}\text{C}$, and $P = 4.5$ bar ($P_{\text{CO}_2} = 3.8$ bar). (a) top C1018; (b) top X-65; (c) bottom C1018; (d) bottom X-65.

Test with 1% NaCl.

The results obtained in this experiment are shown in Figure 5.3.9, Figure 5.3.10, and Figure 5.3.11. This test was stopped after 100 hours due to failure of the gas pump. But the experiment was long enough to show the trend and allow comparison with the previous two tests. For example, the pH and Fe^{2+} concentration change follow the same trend as the other two tests (Figure 5.3.9), and the LPR bottom measurement again shows the protective film formation after an initial time (Figure 5.3.10). All the other corrosion rate measurements show a trend similar to the other two tests, but have slightly higher values (Figure 5.3.11). Localized corrosion occurred on both materials with a small percentage of surface area attacked, which is different from the last two tests. Cross-sectional analysis (Figure 5.3.12) again shows protective film on the top specimen and a very porous film on the bottom specimen.

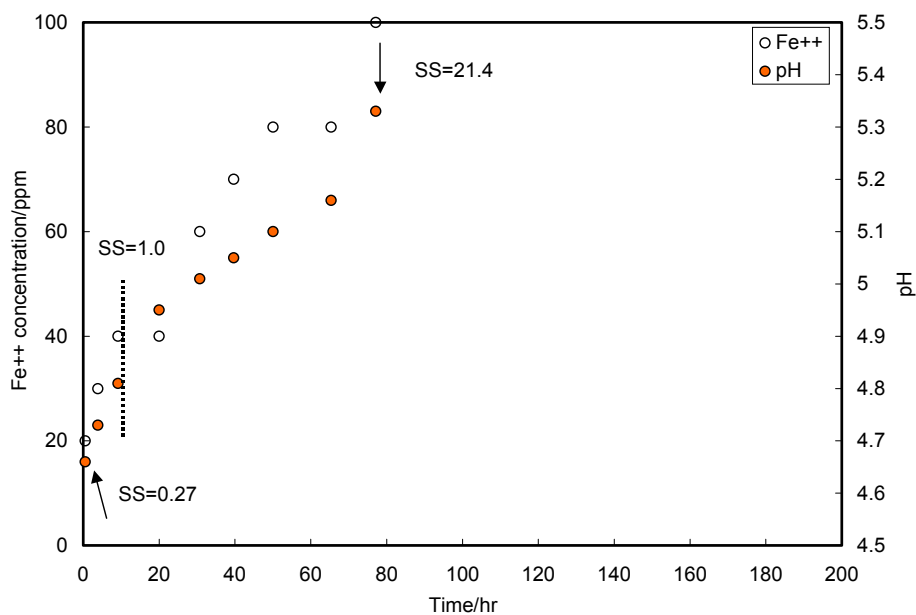


Figure 5.3.9 The change of pH and Fe^{2+} with time for 1% NaCl solutions at $V_{\text{s}g} = 10$ m/s, $V_{\text{s}l} = 0.1$ m/s, $T = 90^{\circ}\text{C}$, and $P = 4.5$ bar ($P_{\text{co}_2} = 3.8$ bar).

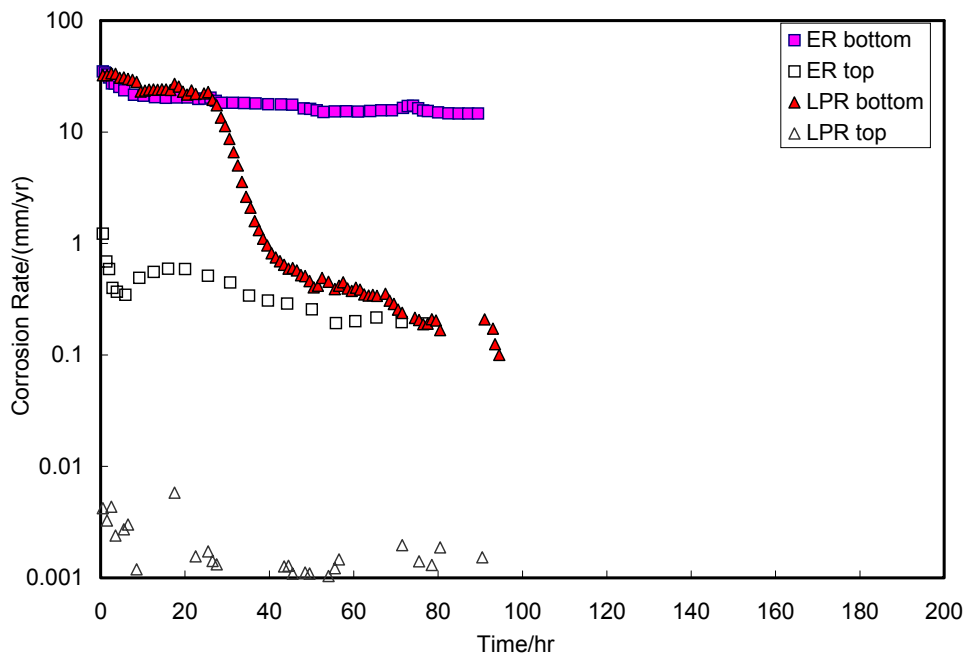


Figure 5.3.10 The change of corrosion rate with time for 1% NaCl solutions at $V_{sg} = 10$ m/s, $V_{sl} = 0.1$ m/s, $T = 90^{\circ}\text{C}$, and $P = 4.5$ bar ($P_{\text{CO}_2} = 3.5$ bar).

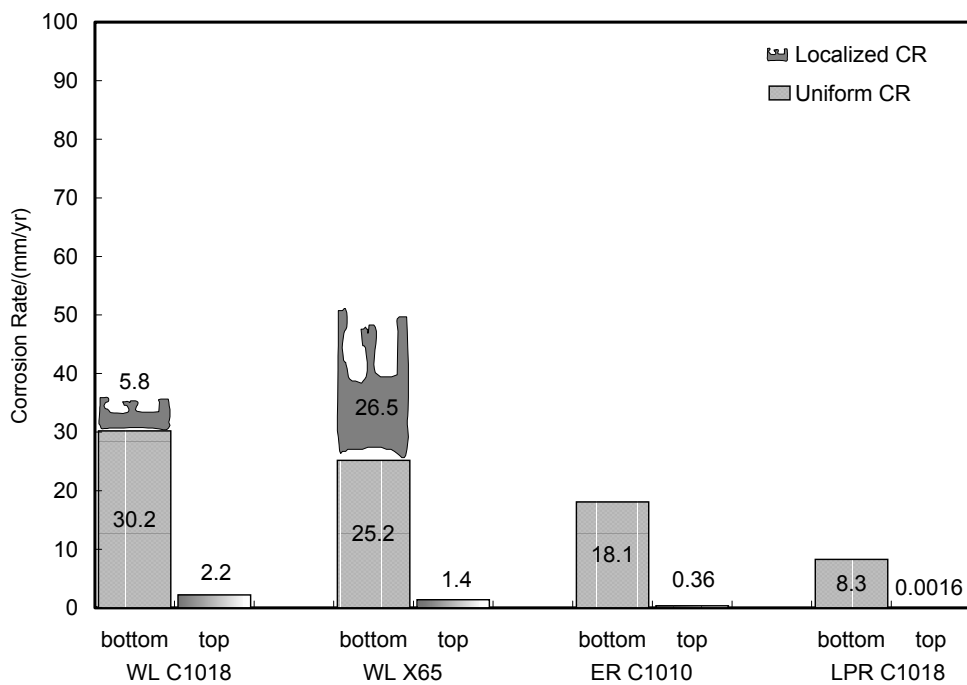


Figure 5.3.11 Average and localized corrosion rate (LC) from different methods for 1% NaCl solutions at $V_{sg} = 10$ m/s, $V_{sl} = 0.1$ m/s, $T = 90^{\circ}\text{C}$, and $P = 4.5$ bar ($P_{\text{CO}_2} = 3.8$ bar).

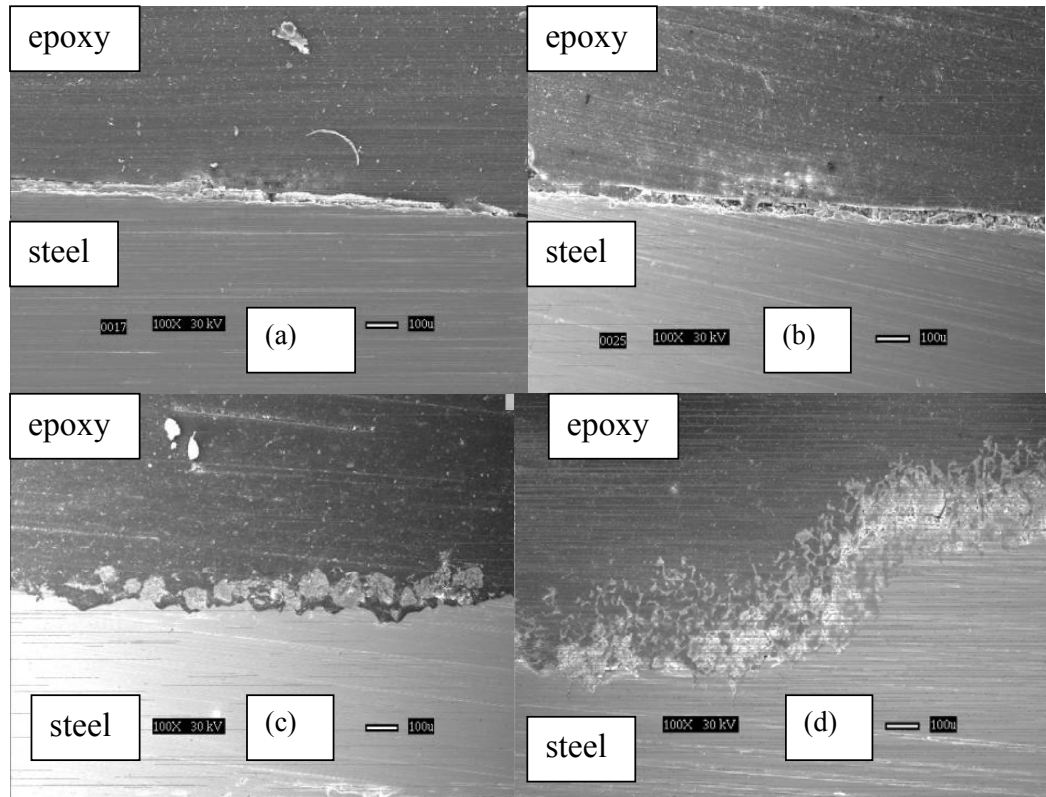


Figure 5.3.12 Cross sections for 1% NaCl solutions at $V_{sg} = 10$ m/s, $V_{sl} = 0.1$ m/s, $T = 90^{\circ}\text{C}$, and $P = 4.5$ bar ($P_{\text{CO}_2} = 3.8$ bar). (a) top C1018; (b) top X-65; (c) bottom ER C1010; (d) bottom X-65.

5.3.2 Discussions Of The Effect Of Cl^-

The experimental uncertainty analysis on the corrosion rate from different techniques is as follows: $\pm 0.01\sim 0.8\%$ for the WL measurements, $\pm 0.2\%$ for the ER bottom measurements, $\pm 2.4\sim 5.0\%$ for the ER top measurements, and $\pm 27.2\%$ for the LPR measurements. The relative error for localized corrosion measurements is $\pm 0.3\sim 2\%$.

Figure 5.3.13 shows the effect of NaCl concentration on the bottom corrosion rate from the WL method for both materials. It is seen that Cl^- had some effect on both uniform and localized corrosion rate on the bottom of the line. In all cases, localized

corrosion occurred on both materials. However, Figure 5.3.13 does not tell more about the nature of the localized attack. As described above, some of the localized attack was widespread on the specimen surface, with hills, valleys, and mesa-type corrosion covering the whole surface, while on others it was a true local phenomenon. Based on this consideration, the concept of pitting density was proposed to describe the localized corrosion. The pitting density is defined as the ratio of pitted area or the area suffering localized attack to the total area of the specimen. The results are shown in Figure 5.3.14. With an increase in Cl^- concentration, the pitting density decreased, which means that the localized attack tends to be more “local.” C1018 and X65 have different sensitivities with respect to the Cl^- concentration.

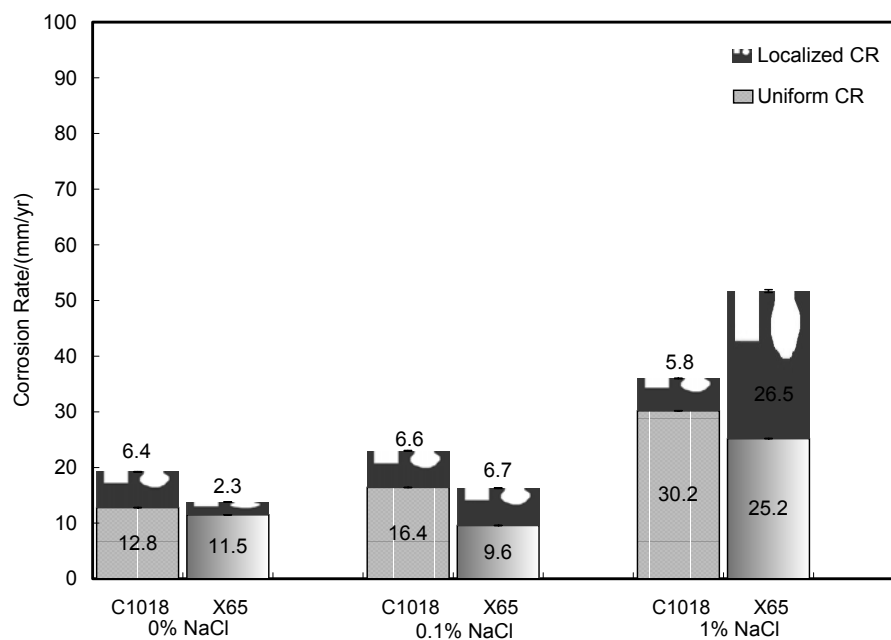


Figure 5.3.13 The effect of NaCl concentration on bottom corrosion for different materials from WL method at $V_{sg} = 10$ m/s, $V_{sl} = 0.1$ m/s, $T = 90^\circ\text{C}$, and $P = 4.5$ bar ($P_{\text{CO}_2} = 3.8$ bar).

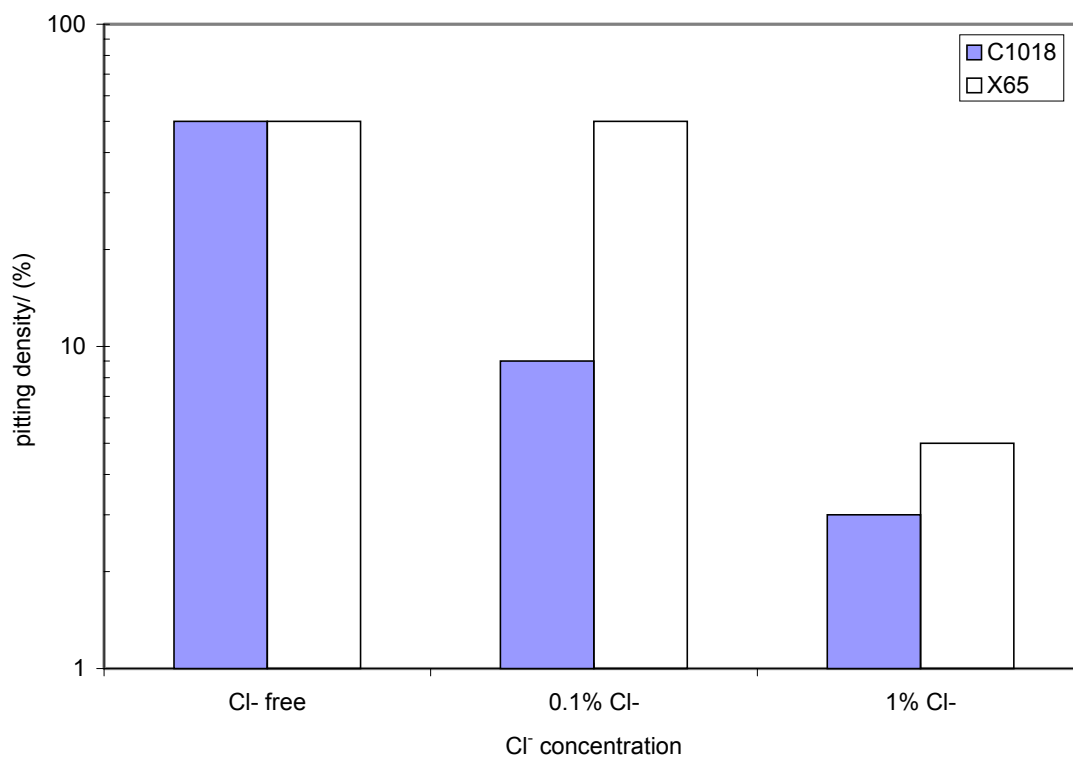


Figure 5.3.14 The effect of Cl⁻ concentration on localized corrosion at $V_{sg} = 10$ m/s, $V_{sl} = 0.1$ m/s, $T = 90^{\circ}\text{C}$, and $P = 4.5$ bar ($P_{\text{CO}_2} = 3.8$ bar).

In all three experiments, the water chemistry was changing from an under-saturated iron solution at the beginning to a super-saturated iron solution at the end of each test, as shown in Table 5.3.2. This might have created a favorable environment for initiation of localized corrosion. Figure 5.3.15 may help explain what happened. It seems that super saturation played a very important role in the onset of localized corrosion. Localized corrosion may not occur in either an under-saturated solution or a highly super-saturated solution as discussed previously. The tests presented in this work happened to fall in a range close to the saturation line, and localized corrosion was triggered. At these environment parameters, the Cl⁻ affects the solution super saturation level through ionic strength and the iron carbonate solubility as shown in Table 5.3.2 below.

Table 5.3.2 Super-saturation (SS) table and the estimated pitting density for Cl⁻ series test.

NaCl, %	At the beginning of test			At the end of test			Pitting density	
	Measured pH	Measured Fe ²⁺	SS level	Measured pH	Measured Fe ²⁺	SS level	C1018	X-65
0.0	4.65	20	0.60	4.94	50	5.5	50%	50%
0.1	4.65	20	0.42	5.13	100	30.9	9%	50%
1.0	4.65	20	0.27	5.3	100	21.4	3%	5%

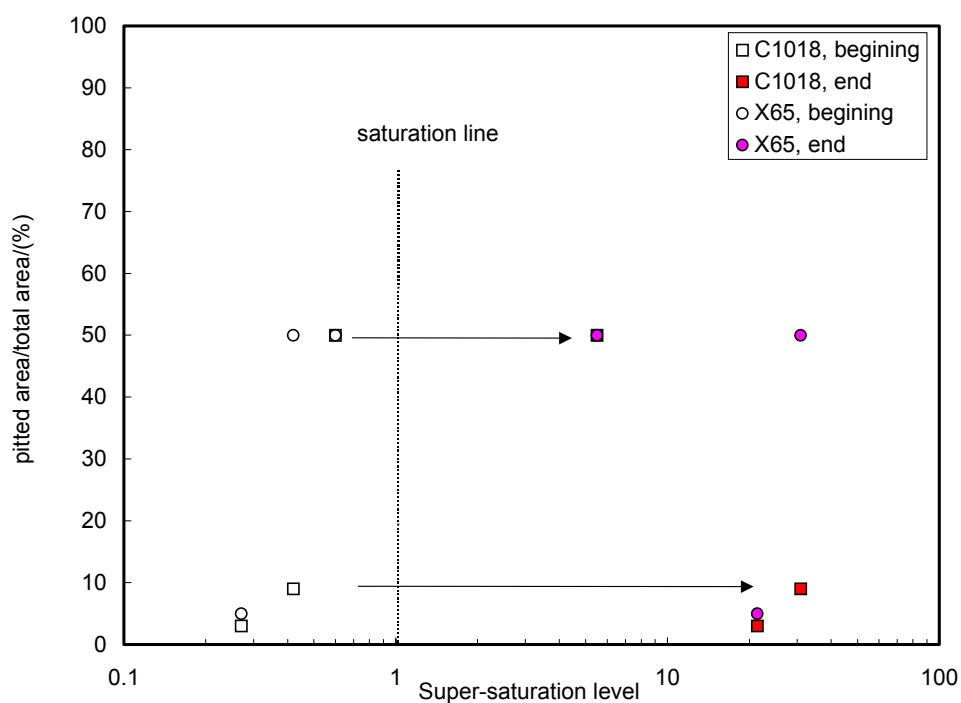


Figure 5.3.15 The relationship between the super-saturation level and pitting density for the bottom at $V_{sg} = 10$ m/s, $V_{sl} = 0.1$ m/s, $T = 90^{\circ}\text{C}$, and $P = 4.5$ bar ($P_{\text{CO}_2} = 3.8$ bar).

Without exception, no localized corrosion was found on the top of the line in any of the tests. The corrosion rate was orders of magnitude lower than the bottom, as shown in Figure 5.3.16 by ER measurements. The flow regime was in stratified flow according to the pressure drop measurement result, which was 38.5 Pa/m.

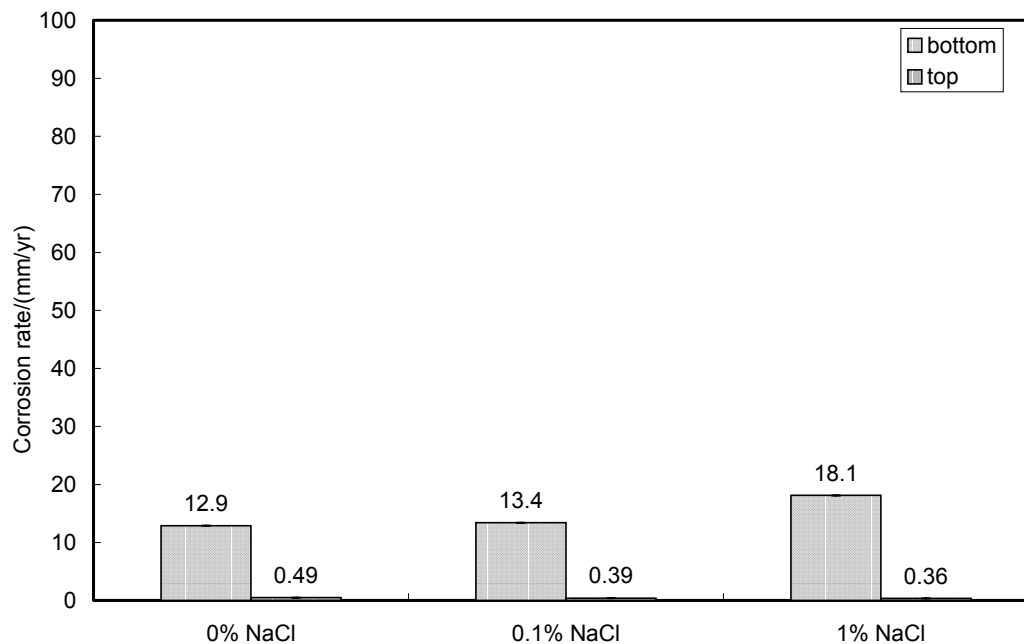


Figure 5.3.16 The effect of NaCl concentration on the average corrosion rate by ER measurements at $V_{sg} = 10$ m/s, $V_{sl} = 0.1$ m/s, $T = 90^{\circ}\text{C}$, and $P = 4.5$ bar ($P_{\text{co}_2} = 3.8$ bar).

The water chemistry on the top of the line was different from the bottom. Under the stratified flow conditions tested, the water on the top of the pipe could be from two sources: either from the droplets entrained in the gas phase, which should have the same chemistry as the water at the bottom; or from the pure condensing water, whose chemistry is very different. However, according to the cross-section images, the amount of water on the top must have been very small, enabling formation of a very thin liquid film, which was rapidly saturated by FeCO_3 and led to a protective layer. This layer was not affected by the presence of Cl^- . Admittedly the concentration of Cl^- at the top was most likely lower due to the presence of condensed water. Thus, no localized corrosion was found on the top, and the uniform corrosion rate remained low.

Throughout the three experiments, the ER and WL measurements were in good agreement, while the LPR measurements deviated. The reason for this behavior could be that polarization disturbs the corrosion process. This would become more important when the solution is around the saturation point. Cathodic polarization consumes hydrogen ions and creates a locally higher pH, while the anodic scan releases more ferrous ions and increases the iron concentration on the steel surface. A higher pH and iron concentration could cause the high super saturation locally, which speeds up the film formation process.

The surface analysis for the corroded specimen provided a solid backing for the corrosion rate measurements. XRD results show that the corrosion product is mainly FeCO_3 for both materials. This is valid for both the top and the bottom specimen in all three tests. The spectrum was the same as the one in Figure 5.2.4. The carbonate layer on the top seems more protective with smaller crystals, indicating higher super saturation and faster precipitation, than those formed on the bottom with a more porous, less crystalline structure, as seen from Figure 5.3.17. The cross-sections of the specimen (Figure 5.3.4, Figure 5.3.8, and Figure 5.3.12) show the thin, protective film on the top and the thick, non-protective film on the bottom. The thickness of the top film was generally less than 10 μm , while the film formed on the bottom was more than 100 μm . In addition, at the bottom, the film was detached from the metal surface over large areas, which provided very poor resistance to corrosion. Therefore, the corrosion product film formed on the bottom of the line was considered non-protective although it provided a certain degree of protectiveness for the steel surface, as one can tell from the corrosion rate profiles in Figure 5.3.2, Figure 5.3.6, and Figure 5.3.10. The corrosion rate decreased slowly with time but maintained a very high value over the entire period.

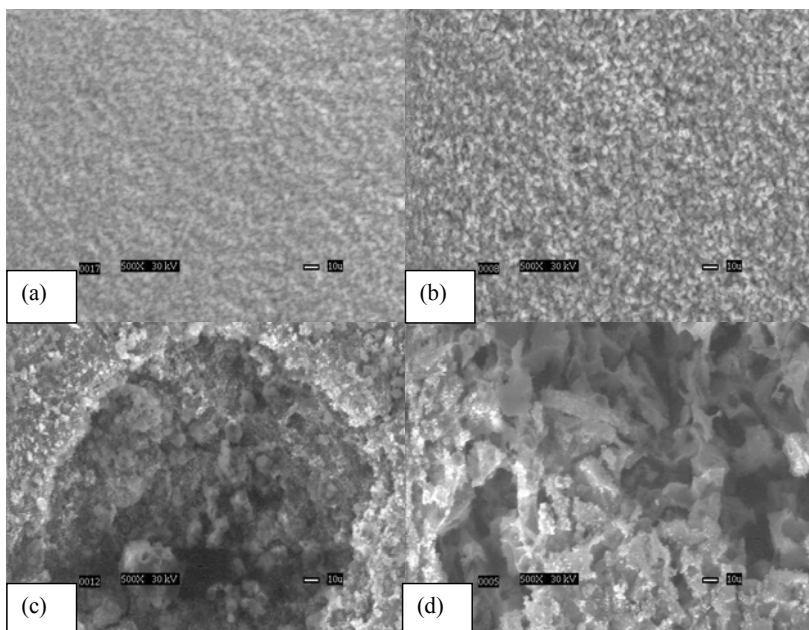


Figure 5.3.17 SEM micrographs for 0.1% NaCl solutions at $V_{sg} = 10$ m/s, $V_{sl} = 0.1$ m/s, $T = 90^{\circ}\text{C}$, and $P = 4.5$ bar ($P_{\text{CO}_2} = 3.8$ bar). (a) top C1018; (b) top X-65; (c) bottom C1018; (d) bottom X65.

5.3.3 Summary For The Effect of Cl^-

Under wet gas test conditions, localized corrosion occurred at the bottom of the line on both C1018 and X65 materials irrespective of the Cl^- concentrations but with different pitting densities. Pitting density is thus recommended for use as an additional parameter when describing the localized corrosion behavior. Neither C1018 nor X-65 suffered localized attack at the top of line under stratified flow conditions. Cl^- content is important in the onset of localized corrosion since it largely affects the ionic strength and thus super-saturation level of the solution. A higher Cl^- concentration seems to cause a lower pitting density, and the localized corrosion tends to be more “local.” C1018 and X-65 steels showed somewhat different sensitivities to pitting density with respect to Cl^- concentration.

5.4 The Effect of CO₂ Partial Pressure in Wet Gas Flow

5.4.1 At 40°C

Temperature is one of the key factors to affect the corrosion product film formation as previously discussed. At 40°C without the adjustment of pH, the main contribution from CO₂ partial pressure would be on the natural pH, as can be seen from Table 5.4.1.

Table 5.4.1 Natural pH and super saturation (SS) level at various CO₂ partial pressures.

P _{co2} , bar		3.8	7.8	11.2	14.7	18.1
0ppm Fe ²⁺	pH	3.68	3.52	3.40	3.38	3.33
	SS	0	0	0	0	0
10ppm Fe ²⁺	pH	4.00	3.80	3.60	3.56	3.50
	SS	0.003	0.002	0.0018	0.0016	0.0015
20ppm Fe ²⁺	pH	4.24	3.95	3.80	3.71	3.64
	SS	0.0018	0.010	0.008	0.0064	0.0056

It is seen that pH decreases with an increase in CO₂ partial pressure. Even with 20 ppm (or mg/kg) ferrous iron in the solution, the pH was still lower than 4.5 and, in most of the circumstances, lower than 4.0 over the entire pressure range. The environment was very acidic and thus corrosive. The solution was far below the saturation (SS = 1) point, and it was not possible for iron carbonate to deposit as a corrosion product film. Therefore, the effect of the CO₂ partial pressure on corrosion rate shown below was conducted under film free conditions.

It was found that only uniform corrosion occurred over the large range of CO₂ partial pressure from around 4 bars to up to 20 bars, and this remained true for both the top and the bottom of the pipe. The results are presented in Figure 5.4.1 and Figure 5.4.2 for different flow conditions.

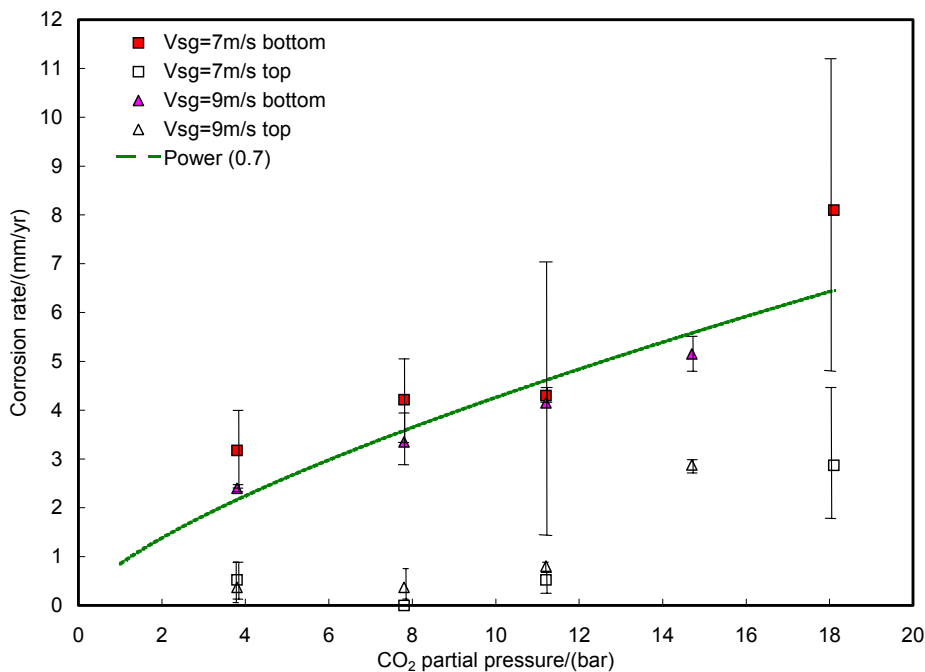


Figure 5.4.1 The effect of CO₂ partial pressure on both the top and the bottom corrosion rate at Vsl = 0.1 m/s, T = 40°C with D.I. water only.

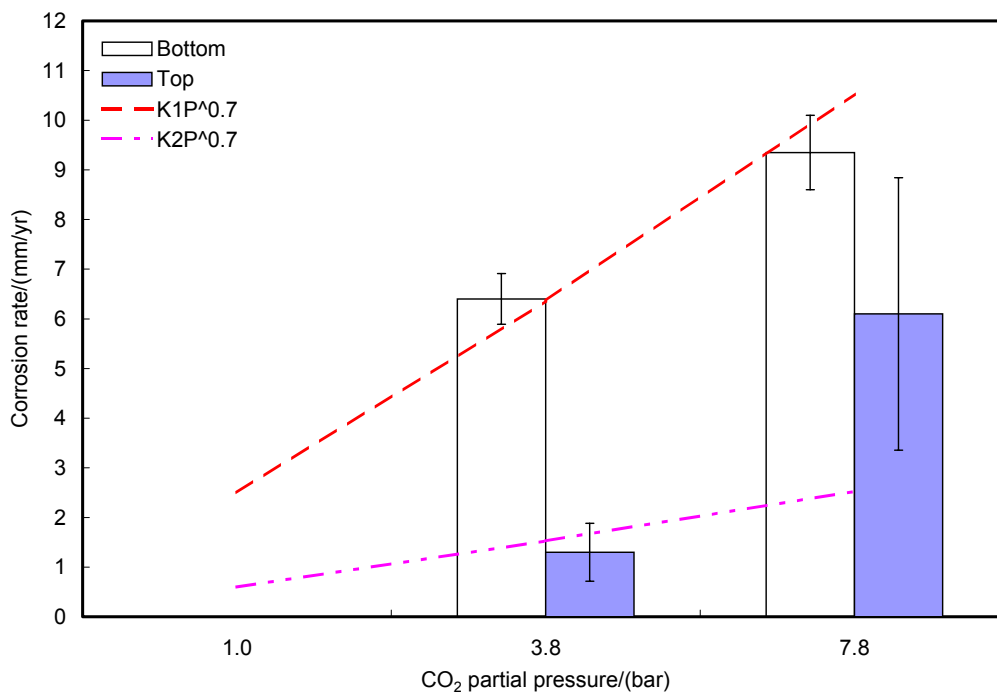


Figure 5.4.2 The effect of CO₂ partial pressure on both the top and the bottom corrosion rate at Vsl = 0.2 m/s, Vsg = 10 m/s, T = 40°C with D.I. water only.

The measurement was done by the ER method. Since most of the data points were measured by two ER probes, the error bars in the above two graphs represent the relative errors from the experiments. In cases where only one data point was available, the experimental uncertainty analysis described in Appendix B was applied.

For the experiments with a superficial liquid velocity of 0.1 m/s shown in Figure 5.4.1, the corrosion rate increased with the increase in CO₂ partial pressure for both the top and the bottom. However, the corrosion rate followed different trends at the two locations. It has been suggested (de Waard and Lotz, 1993, Dugstad et al., 1994) that the corrosion rate increases with a 0.7 power in relation to CO₂ partial pressure. Therefore, a power of 0.7 over the CO₂ partial pressure line was also given in Figure 5.4.1 for comparison. It is seen that the bottom of line corrosion rate in wet gas conditions also follows the 0.7 power law under film-free conditions. The corrosion rate on the top was small at low pressure up to 8 bars but dramatically increased with rising CO₂ partial pressure. The power law did not apply on the top corrosion rate mostly because of the flow regime change. At low pressure, the flow was in stratified with only occasional droplets hitting on the top of the pipe wall; at high pressure, the flow pattern changed from stratified to semi-annular or annular flow (with some transition zone in between), the top of the pipe started to see the same water phase as the bottom, and the corrosion rate went up consequently.

With a superficial liquid velocity of 0.2 m/s and a superficial gas velocity of 10 m/s, the bottom corrosion rate agreed well with the power law, but the corrosion rate on the top was out of the power line (see Figure 5.4.2). Under these flow conditions, even

the top of the line had high corrosion rates up to a few millimeters per year. The increase in partial pressure might have facilitated the water to spread around the pipe cross-section and cause the formation of annular flow. However, the local water film velocity and thickness could be different when changing the pressure, even when the superficial flow velocities were kept the same.

Localized corrosion was not identified at this temperature due to film-free conditions. Further investigations with CO₂ partial pressure were performed with conditions that could form corrosion product films.

5.4.2 At 90°C

In the CI series tests in section 5.3, localized corrosion occurred on the bottom of the pipe without the adjustment of pH. More tests were performed under controlled pH environments to identify the effect of CO₂ partial pressure on localized corrosion. The test matrix for this series is shown in Table 5.4.2. Since only pH and pressure were changed, the four experiments conducted are called: low-pressure low-pH test, low-pressure high-pH test, high-pressure low-pH test, and high-pressure high-pH test.

Table 5.4.2 The test matrix for the series of test on the effect of CO₂ partial pressure.

Liquid phase	1% NaCl
Total pressure	4.5, 11.3 bar
CO ₂ partial pressure	3.8, 10.6 bar
Temperature	90°C
pH	<5.2, 5.2, 6.2
Superficial liquid velocity	10 m/s
Superficial gas velocity	0.1 m/s
Material tested	C1018, X65, and C1010
Measurement techniques	ER, LPR, and WL

Low-pressure (3.8 bar), low-pH (4.6~5.3) test

This test was actually one of the Cl^- series test, and the results have been presented in section 5.3. The pH in this test was not adjusted but increased due to the release of ferrous iron into the solution. The flow pattern was stratified flow.

High-pressure (10.6 bar), low-pH (5.2) test

The pH was adjusted by adding NaHCO_3 into the loop. The pH and ferrous iron content were monitored during the test, and the result is shown in Figure 5.4.3. Similarly to the Cl^- series tests discussed in section 5.3, the solution started under-saturated and ended up super-saturated. The average pressure drop in this test was 126.2 Pa/m, which suggests that the flow pattern had changed to annular flow.

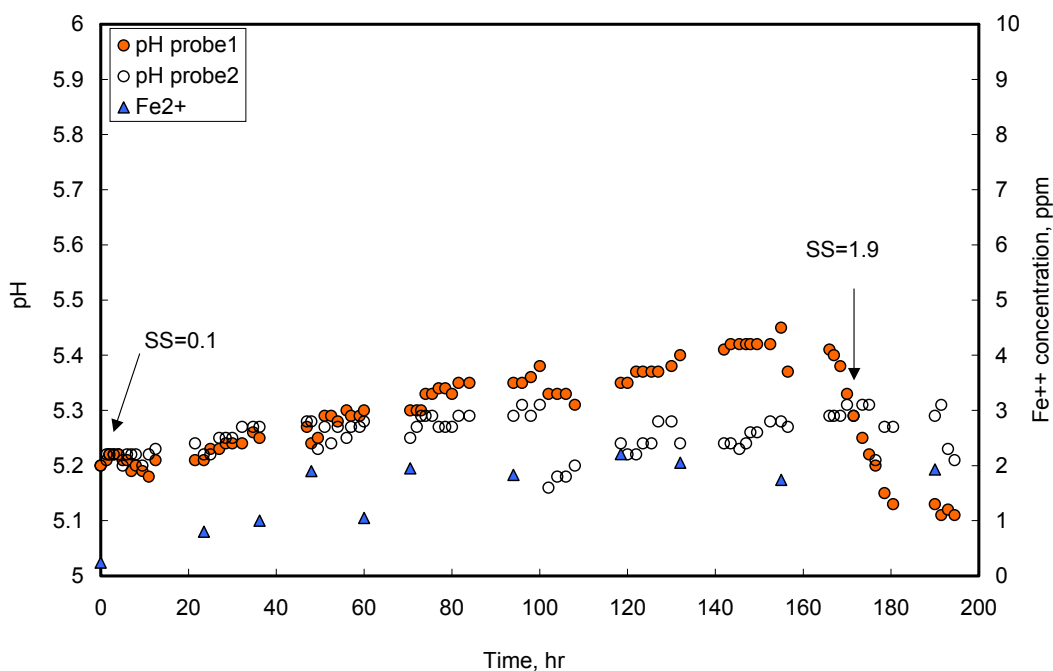


Figure 5.4.3 The pH and Fe^{2+} measurements with time for 1% NaCl at $V_{sg} = 10$ m/s, $V_{sl} = 0.1$ m/s, $T = 90$ °C, and $P = 11.3$ bar ($P_{\text{CO}_2} = 10.6$ bar).

The corrosion rate evolution is shown in Figure 5.4.4 from the ER and LPR methods for both the top and the bottom of the line.

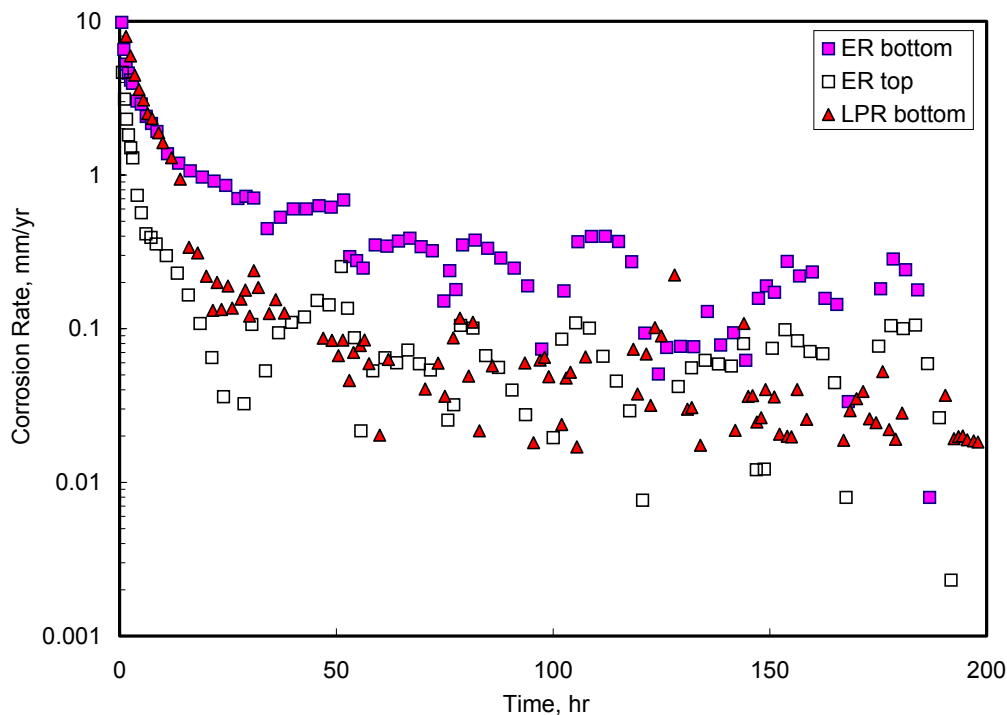


Figure 5.4.4 The change of corrosion rate with time for 1% NaCl at $V_{sg} = 10$ m/s, $V_{sl} = 0.1$ m/s, $T = 90^{\circ}\text{C}$, $P = 11.3$ bar ($P_{\text{CO}_2} = 10.6$ bar), and $\text{pH} = 5.2$.

In contrast to the low-pressure, low-pH test, LPR and ER measurements are in a good agreement with each other for the bottom of the pipe, especially at the beginning of the test. The two measurements overlapped and together showed a high corrosion rate up to 10 mm/yr initially. Shortly thereafter, the corrosion rate decreased with time and stabilized at a lower value. The same can be seen at the top of the line as well. But when compared to the low-pressure, low-pH test, the corrosion rate on the top started at a much higher value, which might be caused by the different flow regimes. The LPR

measurement on the top was not shown in Figure 5.4.4 due to the unreliable results.

During the experiment, it was observed that the open circuit potential (OCP) on the top varied within a large range. This makes the LPR technique difficult to apply, and the corresponding data were rejected. Such phenomena were observed throughout the other tests as well. Thus applying the LPR technique on the top of line proved unsuccessful in wet gas services. It was suspected that the gas phase was probably the major reason for the variation of OCP. Some droplets entrained in the gas phase kept impacting on the electrode surface to cause the unstable OCP value. Based on this, the top LPR measurement results were rejected through this dissertation from here onward.

The time-average corrosion rate from different techniques is shown in Figure 5.4.5.

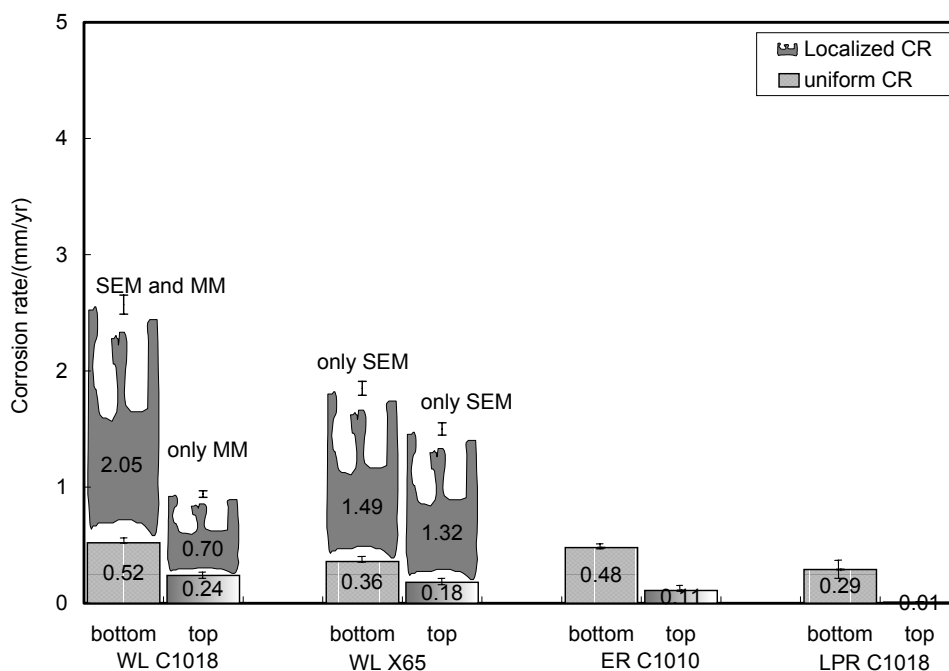


Figure 5.4.5 The average and localized corrosion rate from different methods for 1% NaCl at $V_{sg} = 10$ m/s, $V_{sl} = 0.1$ m/s, $T = 90^{\circ}\text{C}$, $P = 11.3$ bar ($P_{\text{CO}_2} = 10.6$ bar), and $\text{pH} = 5.2$.

It is seen that the average corrosion rate at the bottom still had a higher value (a factor of 2 to 4) than the top, which had been observed in the Cl⁻ series tests. Although the flow regime was in annular flow in this test, the resulting corrosion rates were different from the bottom to the top. This might be caused by the different liquid film thicknesses and velocities from the bottom to the top. It is well known that corrosion is more sensitive to flow under lower pH than higher pH (de Waard and Milliams, 1975), thus the metal surface is more sensitive to flow in the lower pH environment.

Another major finding in this test was the occurrence of localized corrosion on both materials for both the top and the bottom specimen, as can also be seen in Figure 5.4.5. Compared to the low-pressure, low-pH test, the magnitude of localized corrosion was much smaller, but remained much higher when compared to the uniform corrosion rate. SEM micrographs in Figure 5.4.6 indicated the porous film formation on both materials for both the top and the bottom.

Unlike the low-pressure, low-pH test, in which large pits in the middle of the specimen surface were apparent and visible, the localized attack in this test was not seen easily and could only be detected with the help of the metallurgical microscope or from SEM cross section analysis, as shown in Figure 5.4.7. It is seen that the pits formed on the surface were shallow and isolated from each other. Thus, the corrosion product film was considered to be non-protective.

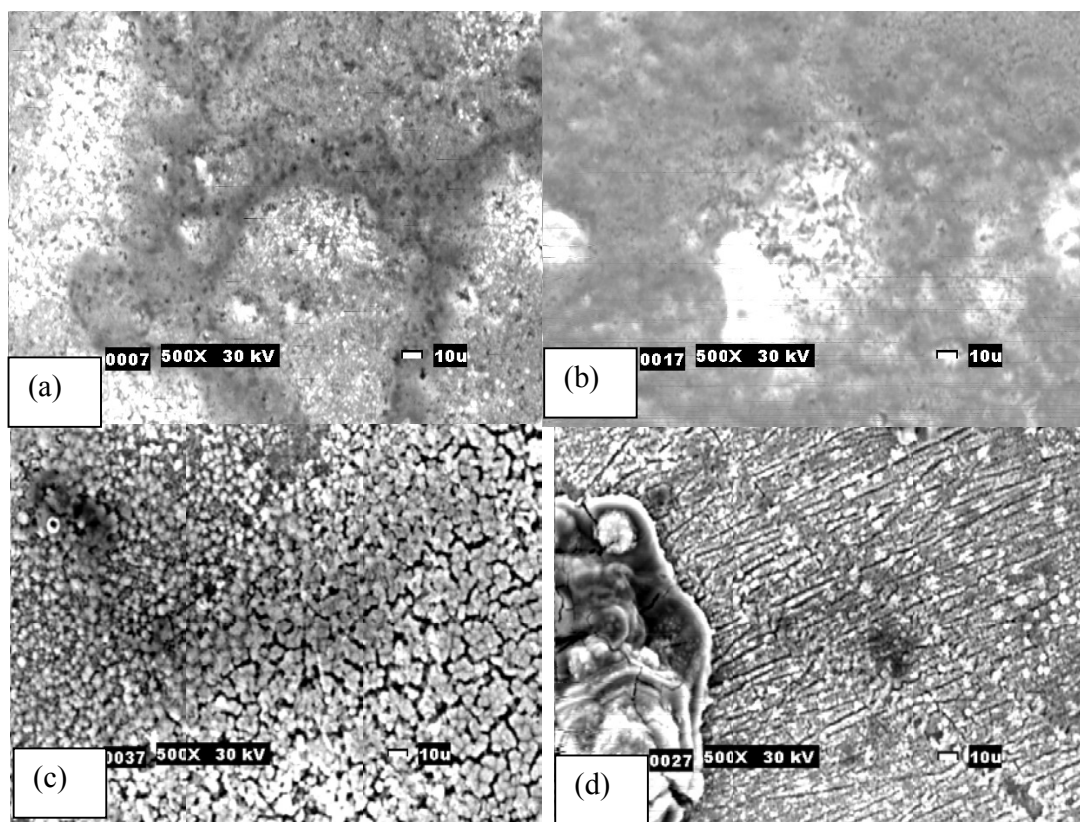


Figure 5.4.6 SEM micrographs for 1% NaCl at $V_{sg} = 10$ m/s, $V_{sl} = 0.1$ m/s, $T = 90$ °C, $P = 11.3$ bar ($P_{CO_2} = 10.6$ bar), and $pH = 5.2$. (a) top C1018; (b) top X-65; (c) bottom C1018; (d) bottom X65.

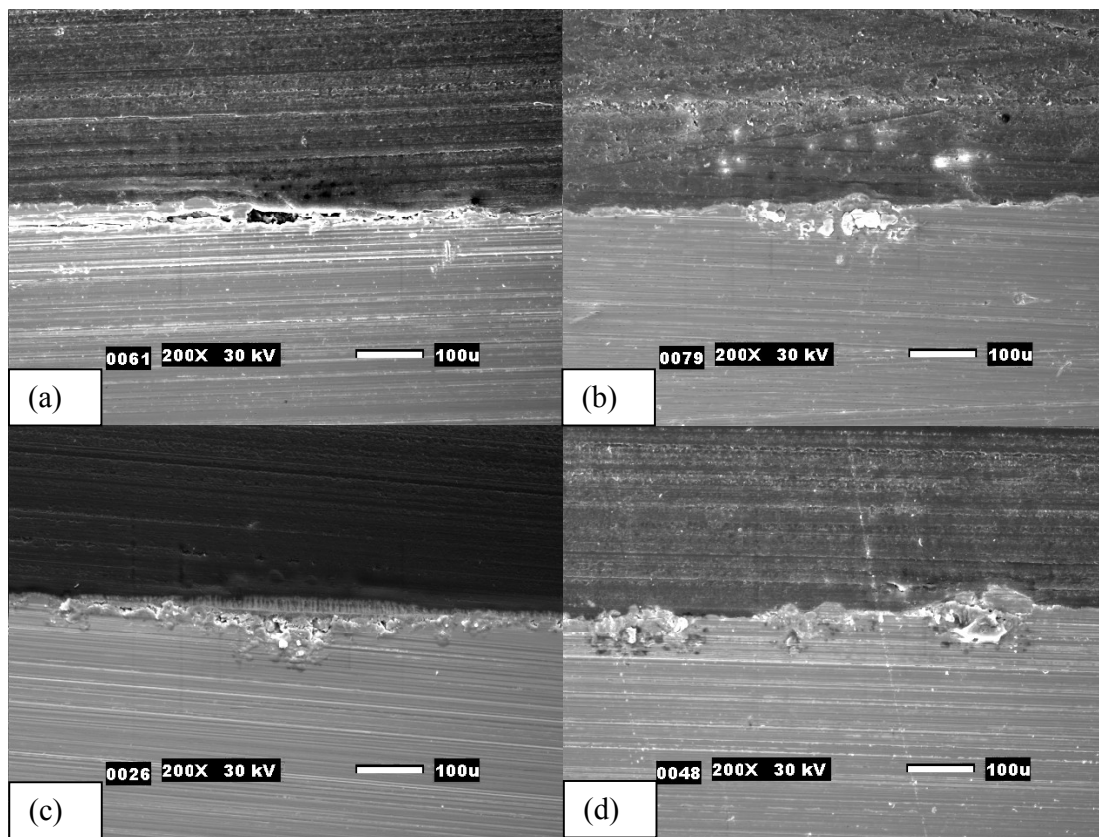


Figure 5.4.7 Cross sections for 1% NaCl at $V_{sg} = 10$ m/s, $V_{sl} = 0.1$ m/s, $T = 90$ °C, $P = 11.3$ bar ($P_{CO_2} = 10.6$ bar), and $pH = 5.2$. (a) top C1018; (b) top X-65; (c) bottom C1018; (d) bottom X65.

Low-pressure (3.8 bar), high-pH (6.2~6.3) test

Four probes were used to monitor the pH during the test. The data is shown in Figure 5.4.8. There are some fluctuations in the pH measurements, but most of the time pH remained between 6.2 and 6.3. Thus the following discussion will refer to this number. The solution started out and was maintained at super-saturation level over the entire test time. The pressure drop was also monitored during the test, and the result was close to the low pH test under the same pressure, which was around 38.5 Pa/m. Thus the flow was in a stratified flow regime.

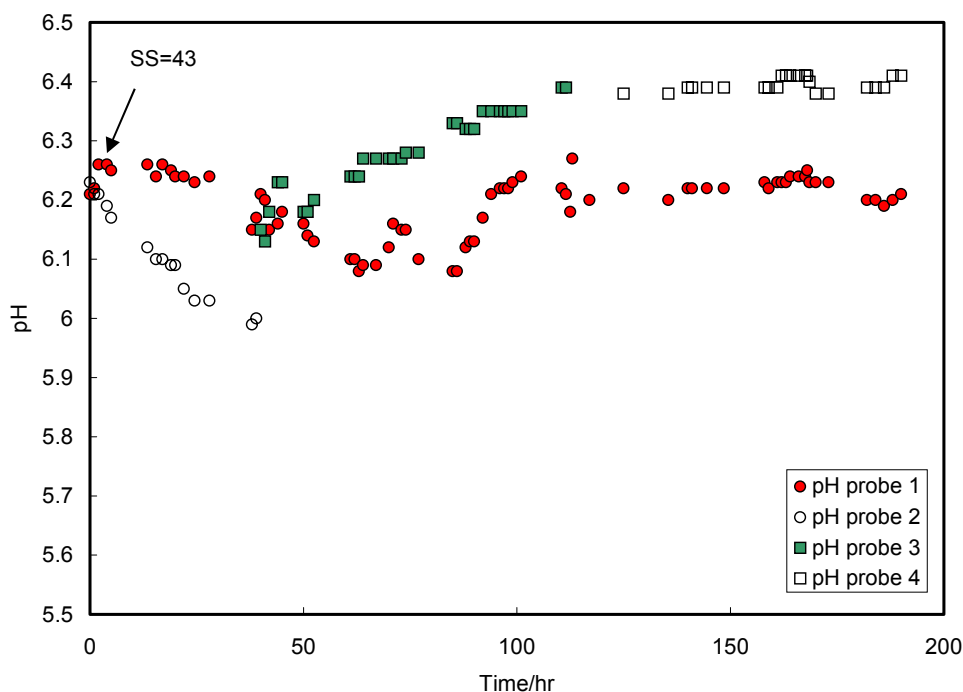


Figure 5.4.8 The pH measurement with time for 1% NaCl at $V_{sg} = 10$ m/s, $V_{sl} = 0.1$ m/s, $T = 90$ °C, and $P = 4.5$ bar ($P_{CO_2} = 3.8$ bar).

Figure 5.4.9 shows the evolution of corrosion rate from ER and LPR methods for both the top and the bottom of the pipe. Compared to the low pH test, this high pH test resulted in a much lower (about a factor of 400) corrosion rate even at the beginning of the test for the bottom of the pipe. The corrosion rate at the top of the pipe started with a value similar to the low pH test, but it ended at a lower value. During the test period, the corrosion rate decreased with time and finally stabilized at a very low value (less than 0.1 mm/yr) in a very short time for both the top and the bottom of the pipe. For the bottom of the pipe, the LPR measurement overlaps with the ER measurement almost over the entire range. This builds the confidence in the corrosion rate results as well validates the measurement techniques in wet gas service. Due to the controlled high pH solution on the

bottom, the stabilized corrosion rates at the top and bottom were much closer to each other compared to the low pH test, where the corrosion rate on the bottom were two orders of magnitude higher than on the top with the existence of the same flow pattern.

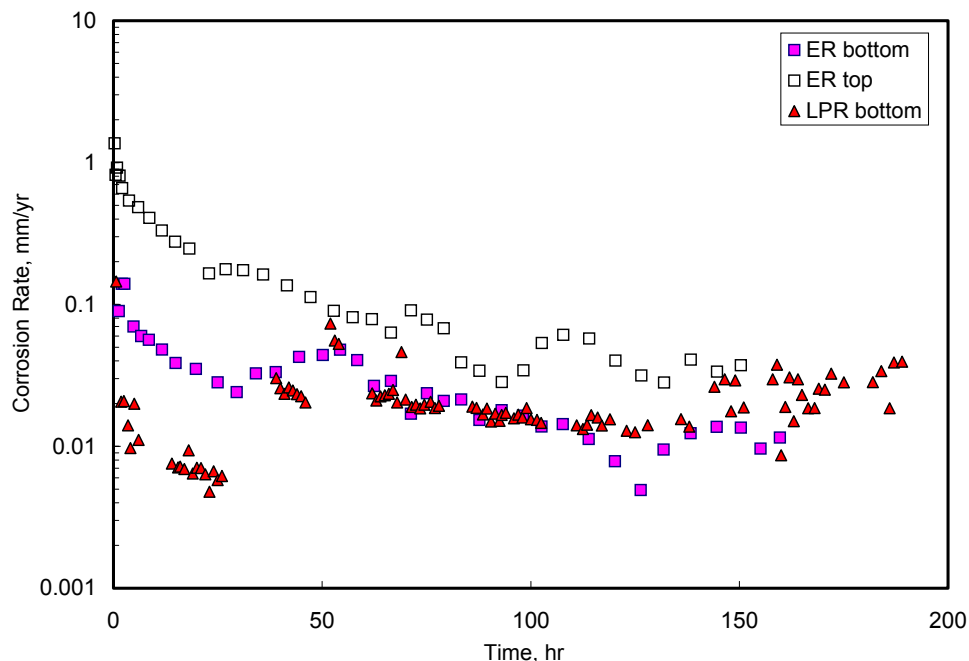


Figure 5.4.9 The change of corrosion rate with time for 1% NaCl at $V_{sg} = 10$ m/s, $V_{sl} = 0.1$ m/s, $T = 90$ °C, $P = 4.5$ bar ($P_{CO_2} = 3.8$ bar), and $pH = 6.2\sim 6.3$.

In the previous low-pressure, low-pH test, the average corrosion rate on the top was orders of magnitude lower than that on the bottom due to the formation of a protective film at the top. In this high pH test, on the contrary, the average corrosion rate on the top was higher than on the bottom, reflected by all the measurement techniques shown in Figure 5.4.10. The bottom of the pipe has nearly no corrosion because of the high pH level in the solution. The top corrosion rate was also low but much higher than the bottom. This suggests that condensation played an important role by decreasing the

pH at the top of line, and the water chemistry was apparently different from the bottom to the top.

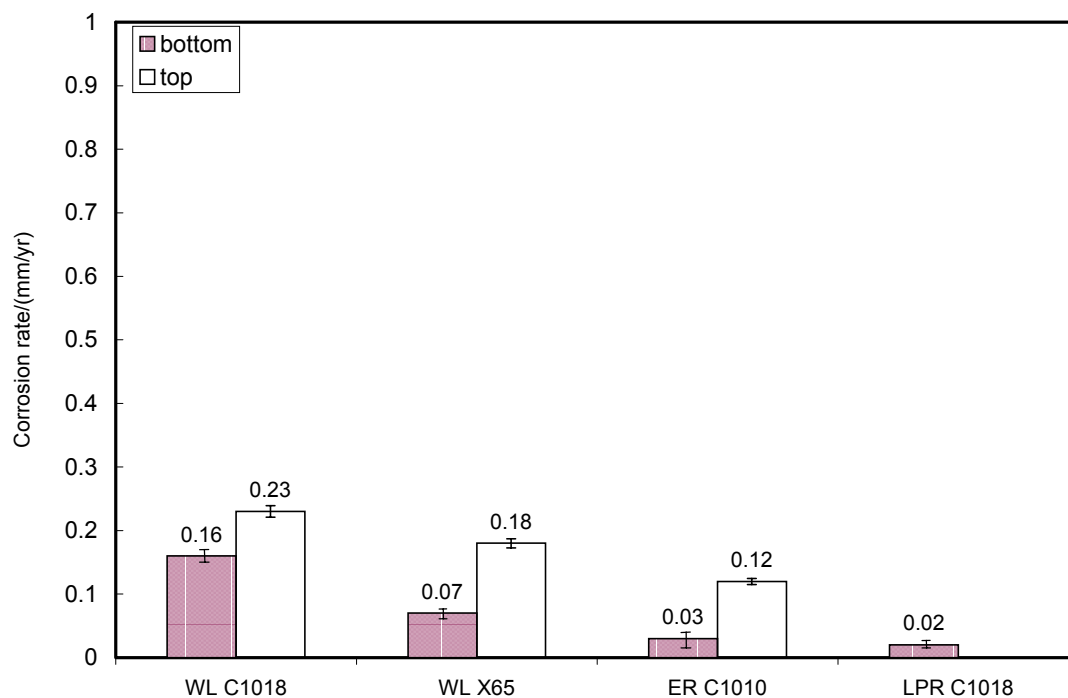


Figure 5.4.10 Average corrosion rate from different methods for 1% NaCl at $V_{sg} = 10$ m/s, $V_{sl} = 0.1$ m/s, $T = 90$ °C, $P = 4.5$ bar ($P_{CO_2} = 3.8$ bar), and $pH = 6.2\sim 6.3$.

SEM micrographs indicated iron carbonate film formation on the top specimen for both C1018 and X65 steel, as shown in Figure 5.4.11, which was also confirmed by the XRD analysis. The bottom specimen of both materials has no clear crystal structure under this magnifications, and the grinding marks are still visible. This suggests that the corrosion product film formed on the specimen surface must be very thin, but very protective according to the corrosion rate analysis.

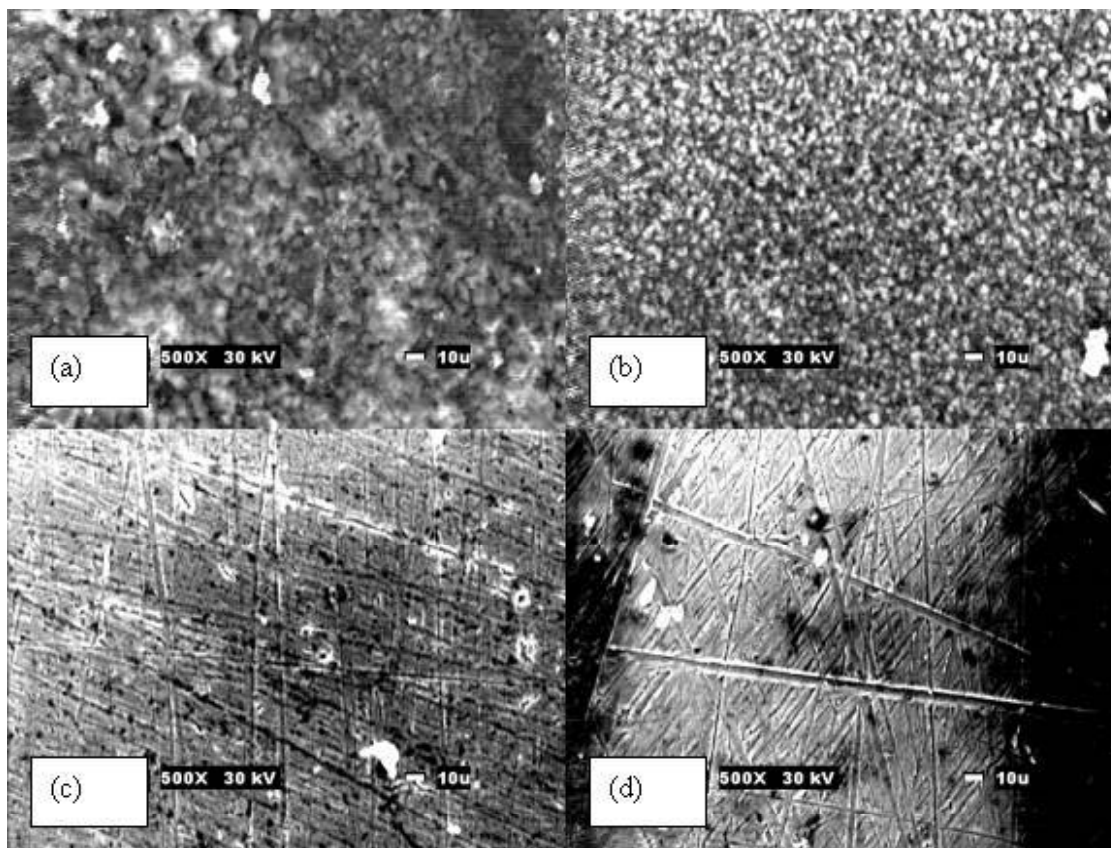


Figure 5.4.11 SEM micrographs for 1% NaCl solution at $V_{sg} = 10$ m/s, $V_{sl} = 0.1$ m/s, $T = 90$ °C, $P = 4.5$ bar ($P_{CO_2} = 3.8$ bar), and $pH = 6.2\sim 6.3$. (a) top C1018; (b) top X-65; (c) bottom C1018; (d) bottom X65.

The cross sectional analysis shown in Figure 5.4.12 confirmed the same information as above, with a layer of carbonate film on the top specimen and almost invisible film on the bottom specimen. However, surface analysis did not reveal any localized attack on either of the materials. The hypothesis proposed at the beginning of this chapter: no localized corrosion occurs when fully protective film is formed, has been apparently proven.

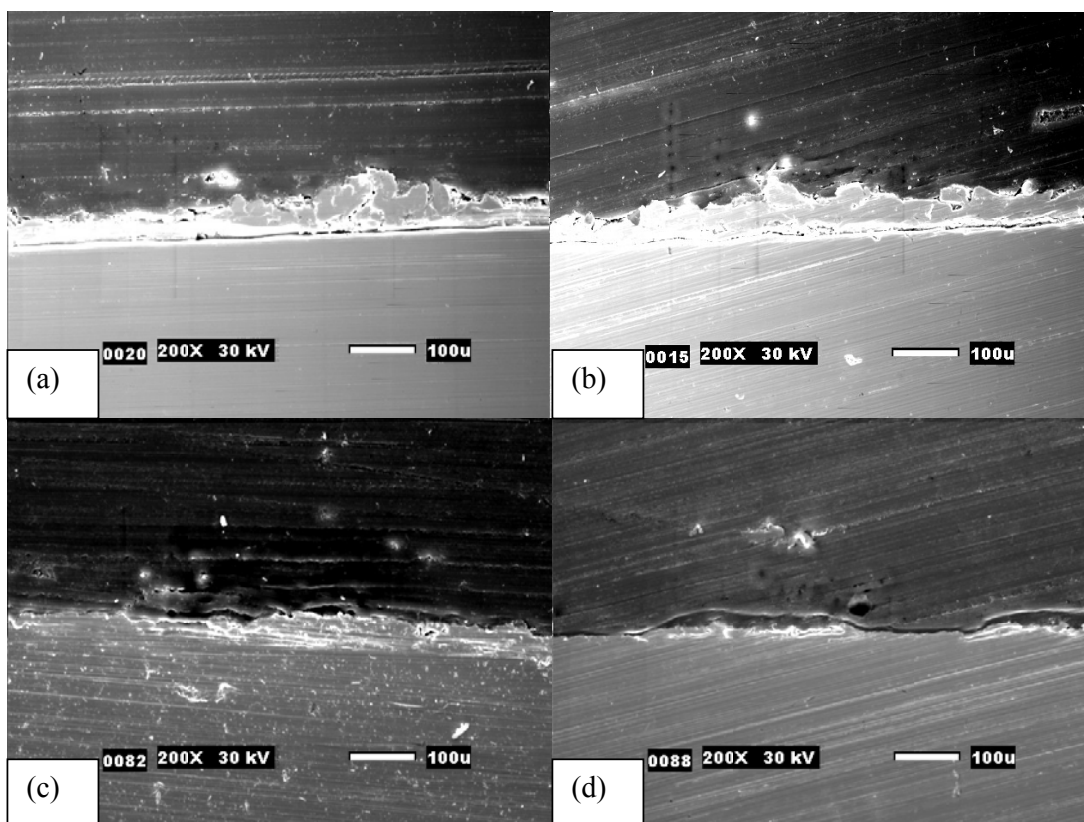


Figure 5.4.12 Cross sections for 1% NaCl solution at $V_{sg} = 10$ m/s, $V_{sl} = 0.1$ m/s, $T = 90$ °C, $P = 4.5$ bar ($P_{CO_2} = 3.8$ bar), and $pH = 6.2\sim 6.3$. (a) top C1018; (b) top X-65; (c) bottom C1018; (d) bottom X65.

High-pressure (10.6 bar), high-pH (6.2) test

The ferrous iron level was less than 5 ppm over the entire test period. The pH was also stable during the test, maintained at 6.2 as shown in Figure 5.4.13. The solution was super-saturated at the beginning of the test. The pressure drop was 134.0 Pa/m, which resulted in the formation of annular flow due to the increased pressure. Thus, the water chemistry was apparently the same for both the top and the bottom.

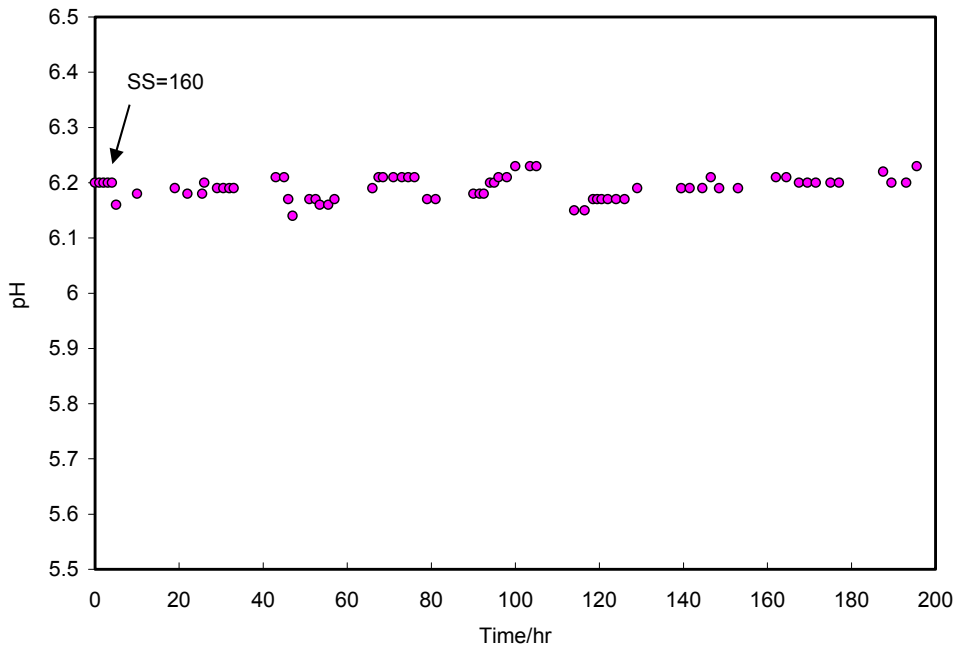


Figure 5.4.13 The pH measurement with time for 1% NaCl at $V_{sg} = 10$ m/s, $V_{sl} = 0.1$ m/s, $T = 90$ °C, and $P = 11.3$ bar ($P_{CO_2} = 10.6$ bar).

Similar to the low pressure, high pH test, the corrosion rate decreased only at the beginning of the test and stabilized at less than 0.1 mm/yr in a short time for both the top and bottom of the line, as reflected by both the ER and LPR methods in Figure 5.4.14. Again, LPR measurements on the bottom were in good agreement with the ER method. The corrosion rate on the bottom essentially did not change compared to the low pressure, high pH test. But the stabilized corrosion rate at the top was getting closer to the bottom one. The average corrosion rate was also getting close from the top to the bottom, reflected by different measurement techniques, as shown in Figure 5.4.15.

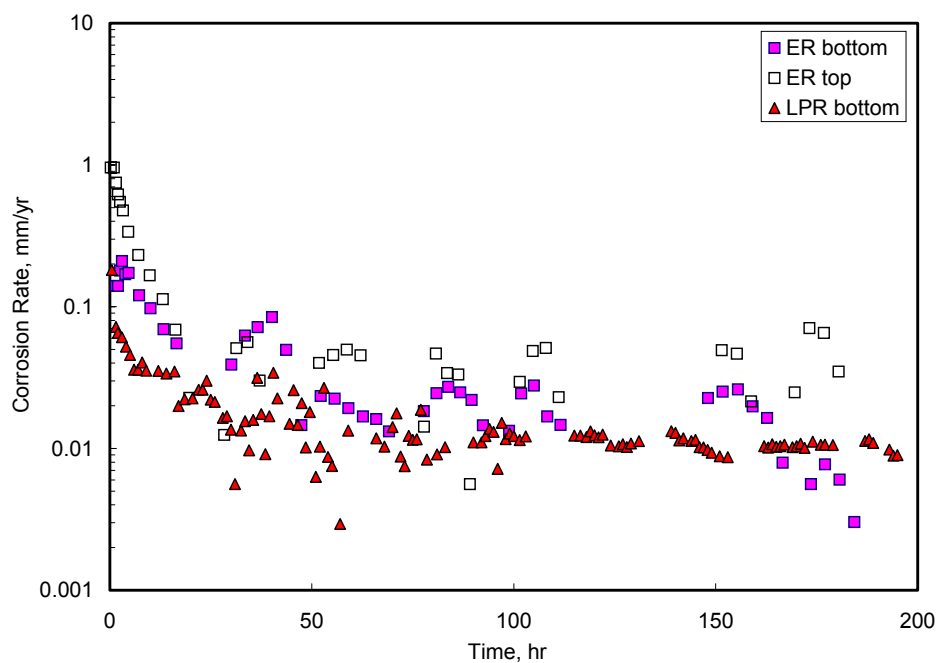


Figure 5.4.14 The change of corrosion rate with time for 1% NaCl at $V_{sg} = 10$ m/s, $V_{sl} = 0.1$ m/s, $T = 90$ °C, $P = 11.3$ bar ($P_{CO_2} = 10.6$ bar), and $pH = 6.2$.

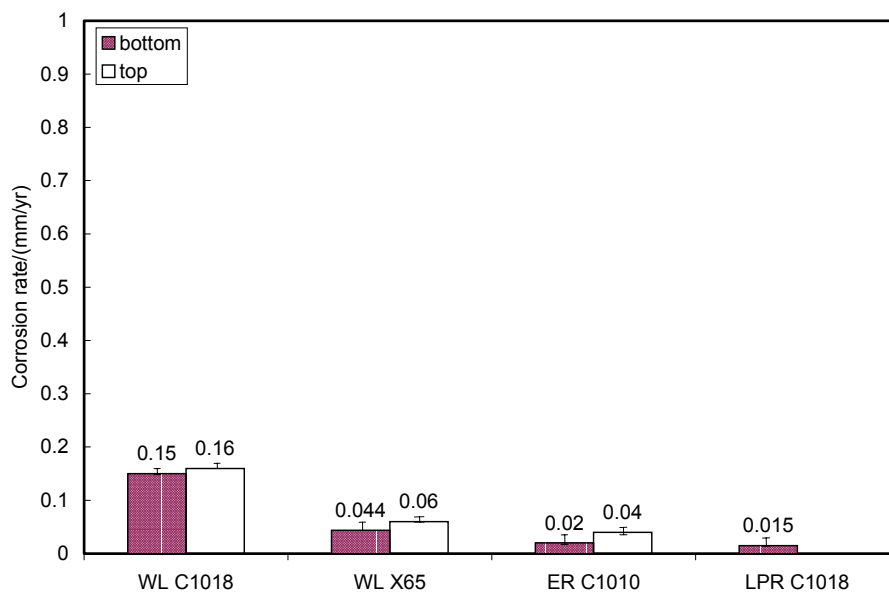


Figure 5.4.15 Average corrosion rate from different methods for 1% NaCl at $V_{sg} = 10$ m/s, $V_{sl} = 0.1$ m/s, $T = 90$ °C, $P = 11.34$ bar ($P_{CO_2} = 10.64$ bar), and $pH = 6.2$.

It is also noticed that WL X65 gave comparable results with ER and LPR, while WL C1018 results deviated from all the other corrosion rate measurements, as also reflected in the low-pressure, high-pH test. The reason was due to the low corrosion rate results and a very thin film on the specimen surface in these two tests. Particularly on the bottom of the pipe, extremely low corrosion was observed. The same procedure was followed to remove the film by using an inhibited HCl solution, which might have caused the unexpected extra metal loss in the C1018 material.

SEM micrographs in Figure 5.4.16 reveal similar information to the low-pressure, high-pH test: clear FeCO_3 crystal (confirmed by XRD analysis) formation on the top specimen for both materials while almost invisible film on the bottom materials.

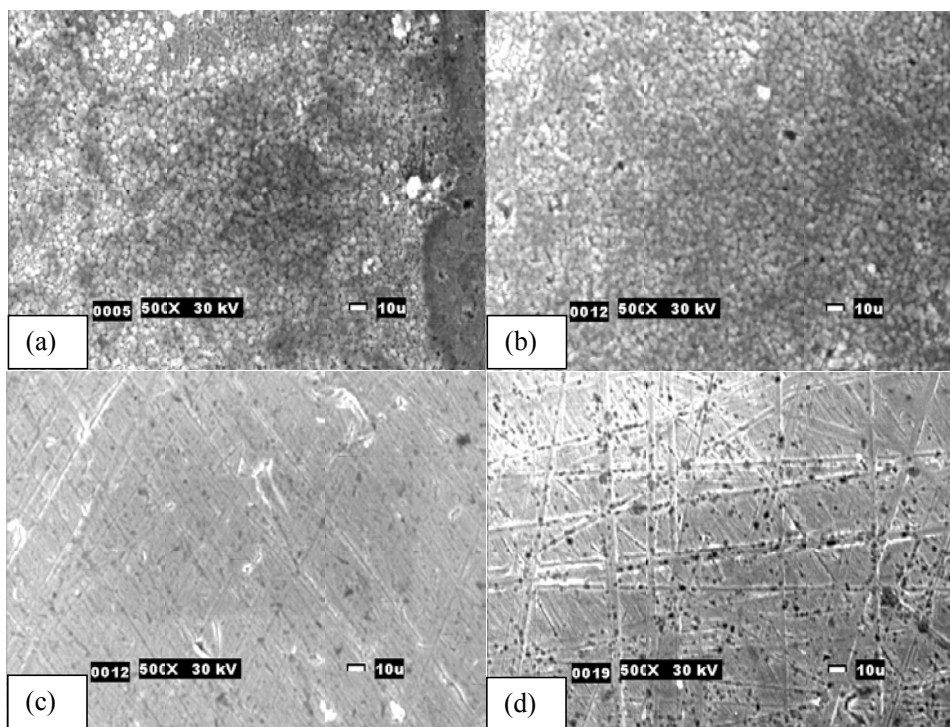


Figure 5.4.16 SEM micrographs for 1% NaCl at $V_{sg} = 10$ m/s, $V_{sl} = 0.1$ m/s, $T = 90$ °C, $P = 11.3$ bar ($P_{CO_2} = 10.6$ bar), and $pH = 6.2$. (a) top C1018; (b) top X-65; (c) bottom C1018; (d) bottom X65.

Similar to the low pressure, high pH test, the surface analysis did not show any localized corrosion on either of the materials (C1018 and X65). High pH essentially inhibited the localized corrosion from occurring over the large range of CO₂ partial pressure.

Figure 5.4.17 shows a cross section analysis for this test. Although the film properties (including the thickness and porosity) were different from the top to the bottom, they successfully prevented the material from corroding, especially localized corrosion. Thus they should be considered as protective films. The second hypothesis at the beginning of this chapter: no localized corrosion occurs when fully protective film is formed, was again proven to be correct.

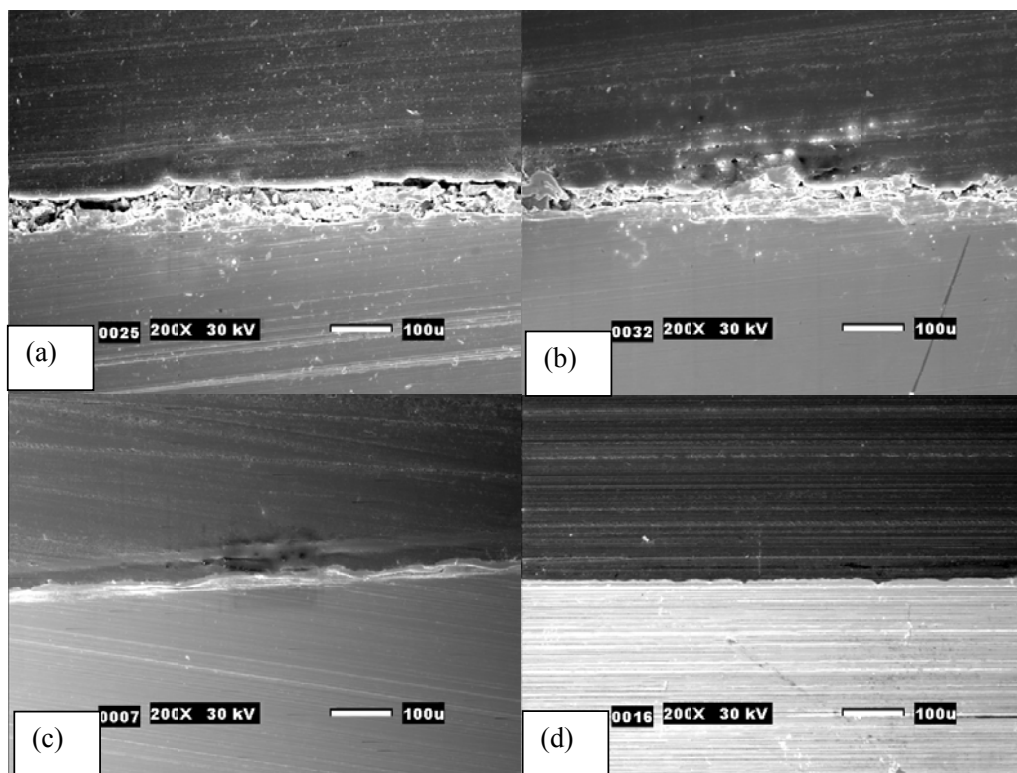


Figure 5.4.17 Cross sections for 1% NaCl at $V_{sg} = 10$ m/s, $V_{sl} = 0.1$ m/s, $T = 90$ °C, $P = 11.34$ bar ($P_{CO_2} = 10.6$ bar), and $pH = 6.2$. (a) top C1018; (b) top X-65; (c) bottom C1018; (d) bottom X65.

Discussions on the effect of CO₂ partial pressure

The CO₂ partial pressure had different effects on corrosion depending on the presence/absence of a corrosion product film. In the tests performed at high temperature, the formation of iron carbonate films with two different properties was observed. One was a so-called non-protective film, which formed in the two low pH tests and provided limited protectiveness. However, the precipitation rate could not keep up with the corrosion underneath the metal, which triggered localized corrosion, as shown in Figure 5.4.18 for both low and high pressures.

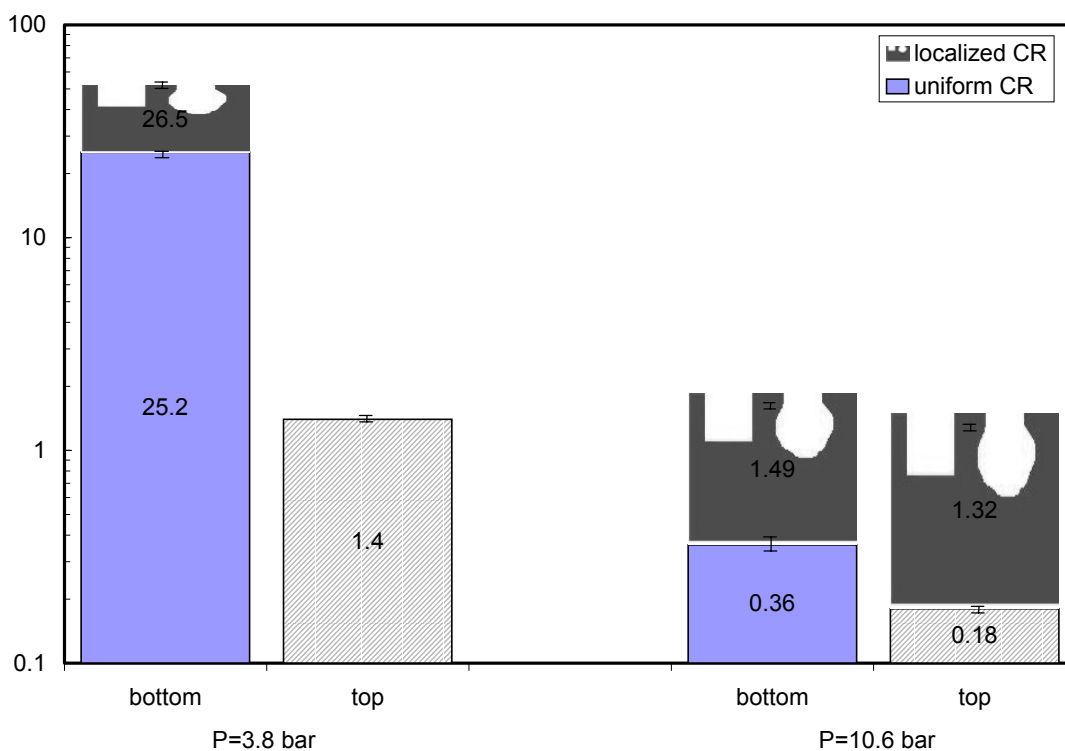


Figure 5.4.18 The effect of CO₂ partial pressure on the corrosion rate at low pH (≤ 5.2) from WL X65 steel at $V_{sl} = 0.1$ m/s, $V_{sg} = 10$ m/s, $T = 90^\circ\text{C}$ with 1% NaCl solution.

The magnitude of the corrosion rate was not directly comparable in Figure 5.4.18 for the two pressures due to two reasons: the low-pressure test had a changing pH throughout the experiment, and it lasted for only 100 hours, while the high pressure test had a fixed pH and lasted for 200 hours. However, from the orders of magnitude difference in the average corrosion rate, it suggests that the higher CO₂ partial pressure had led the formation of a more protective film under film forming conditions. This was also mirrored in the stabilized corrosion rate shown in Figure 5.4.19. Nesic et al (2002) made similar conclusions based on the predictions from their mechanistic film growth model.

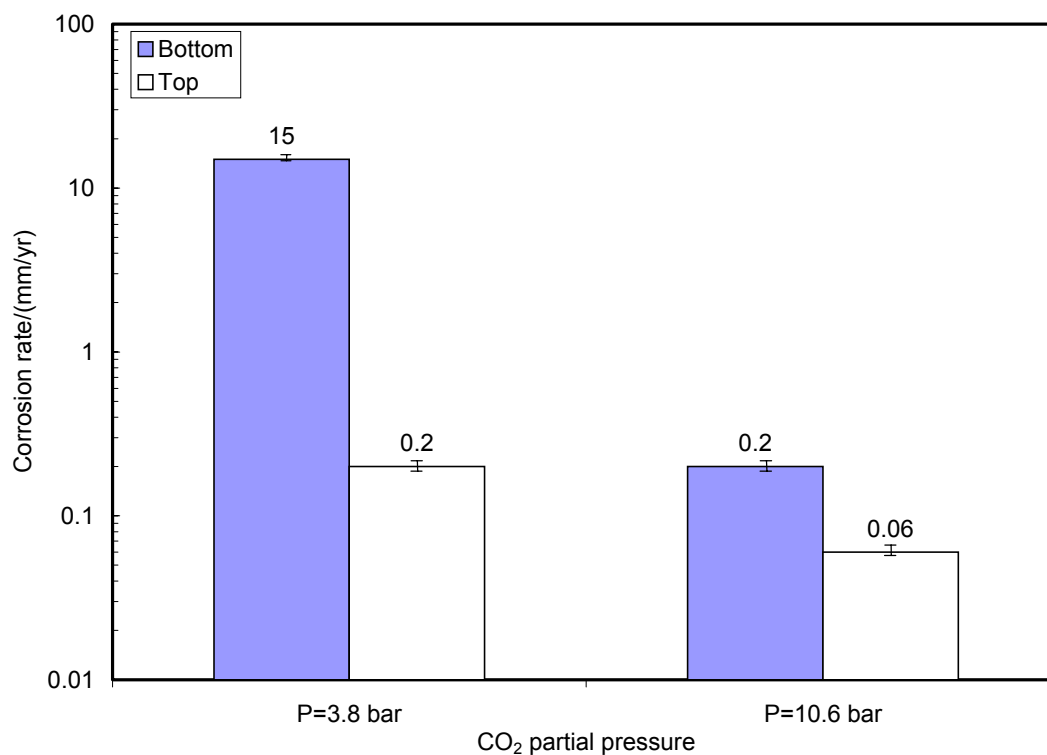


Figure 5.4.19 The effect of CO₂ partial pressure on stabilized corrosion rate at low pH (≤ 5.2) from ER technique at $V_{sl} = 0.1$ m/s, $V_{sg} = 10$ m/s, $T = 90^\circ\text{C}$ with 1% NaCl solution.

The most predominant contribution from pressure was from the change in flow regime. Under the same flow velocities, higher pressure led to the formation of annular flow, which had caused the same water chemistry for both the top and the bottom. Localized corrosion occurred on the top of the line at high pressure, although the stabilized uniform corrosion rate was very low (0.06 mm/yr). The very low uniform corrosion rate does not guarantee safe operation due to possible localized attack. Thus, the real corrosion risk cannot be determined simply from the uniform corrosion rate. This becomes extremely important in field applications, where ER probes are very often used to monitor the corrosion rate. Once localized corrosion takes place, it is always much higher than the uniform corrosion rate measured by the ER technique.

The film formed in the two high pH tests under high temperature can be called a fully protective film. The film provided full protection for the metal surface from corrosion, and no localized corrosion was identified for both low and high pressures, as shown in Figure 5.4.20. Under controlled high pH environments, the increase in CO₂ partial pressure did not change the corrosion rate on the bottom, but it decreased the corrosion rate on the top, as reflected by the different measurement techniques. It seems that a pH of 6.2 was sufficient to inhibit the corrosion process. At high pressure, the flow regime was in annular flow, and the top of the line also experiences high pH. But in stratified flow, as in the low-pressure conditions, the top of the line suffered from condensation at the beginning and resulted in a higher average corrosion rate. However, once the fully protective corrosion product film formed, the corrosion rate was unresponsive to the change of CO₂ partial pressure for both top and the bottom, as can be

seen in Figure 5.4.21. The stabilized corrosion rates were the same for different pressures, and they were below 0.1 mm/yr.

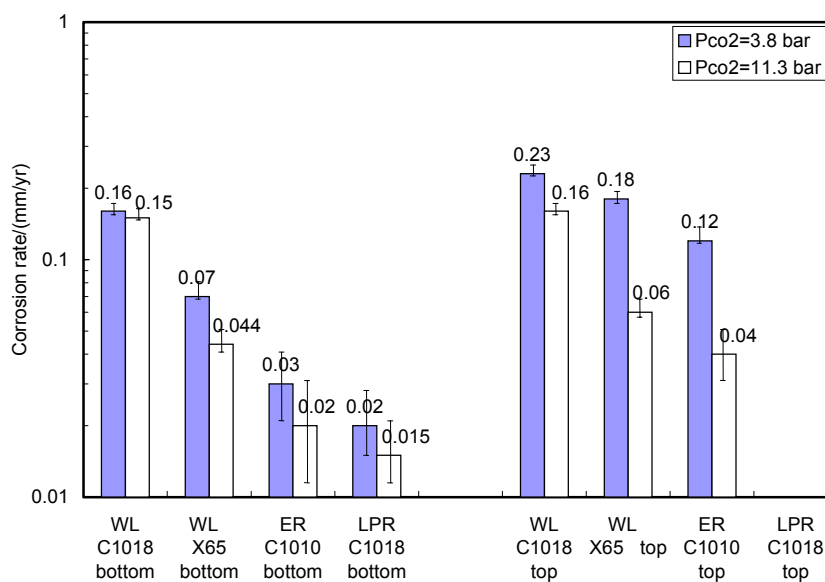


Figure 5.4.20 The effect of CO₂ partial pressure on the corrosion rate at high pH (6.2~6.3) from different measurement techniques at Vsl = 0.1 m/s, Vsg = 10 m/s, T = 90°C with 1% NaCl solution.

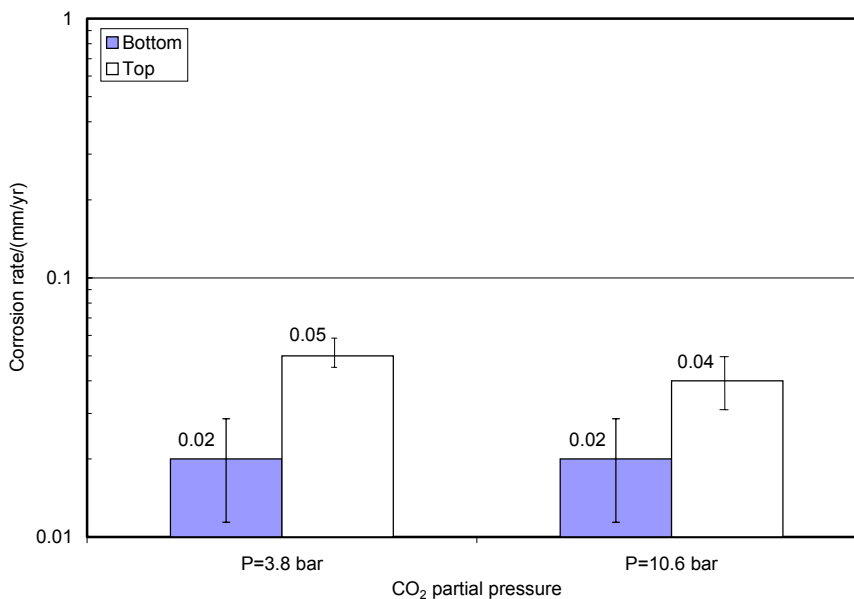


Figure 5.4.21 The effect of CO₂ partial pressure on stabilized corrosion rate at high pH (6.2~6.3) from ER technique at Vsl = 0.1 m/s, Vsg = 10 m/s, T = 90°C with 1% NaCl solution.

5.4.3 Summary On The Effect Of CO₂ Partial Pressure

With the same superficial velocities and temperature, the increase in pressure shifted the flow regime from stratified flow to annular flow, resulting in different corrosion behavior between the top and the bottom of the pipe. CO₂ partial pressure played three different roles with respect to the corrosion product film. Under film-free conditions at 40°C, an increase of CO₂ partial pressure led to an increase in the corrosion rate for both the top and the bottom of the pipe. However, it did not initiate localized corrosion over the entire pressure range. Under film-forming conditions at 90°C, CO₂ partial pressure could increase the rate of film formation and facilitate more protective film formation. The uniform corrosion rate therefore decreased with the increase in CO₂ partial pressure. But this did not prevent the localized corrosion from occurring if the film was not fully protective. Localized corrosion could even take place when the uniform corrosion rate was low. This remained the same for both the top and the bottom of the pipe independent of the flow regime. With the formation of a fully protective film, the increase in the CO₂ partial pressure could not affect the corrosion rate, and no localized corrosion was initiated.

5.5 The Effect of pH in Wet Gas Flow

The significance of pH in CO₂ corrosion has been studied and recognized by different researchers (de Waard and Milliams, 1975, Dugstad et al., 1994, Nestic et al., 1996) over the past twenty years. In accordance with this, its importance was verified again in the present wet gas corrosion study. The major role that pH played can be seen from Figure 5.5.1 through Figure 5.5.4, which represent the pH effect on both average and localized corrosion as well as on the stabilized corrosion rate under low and high CO₂ partial pressures separately.

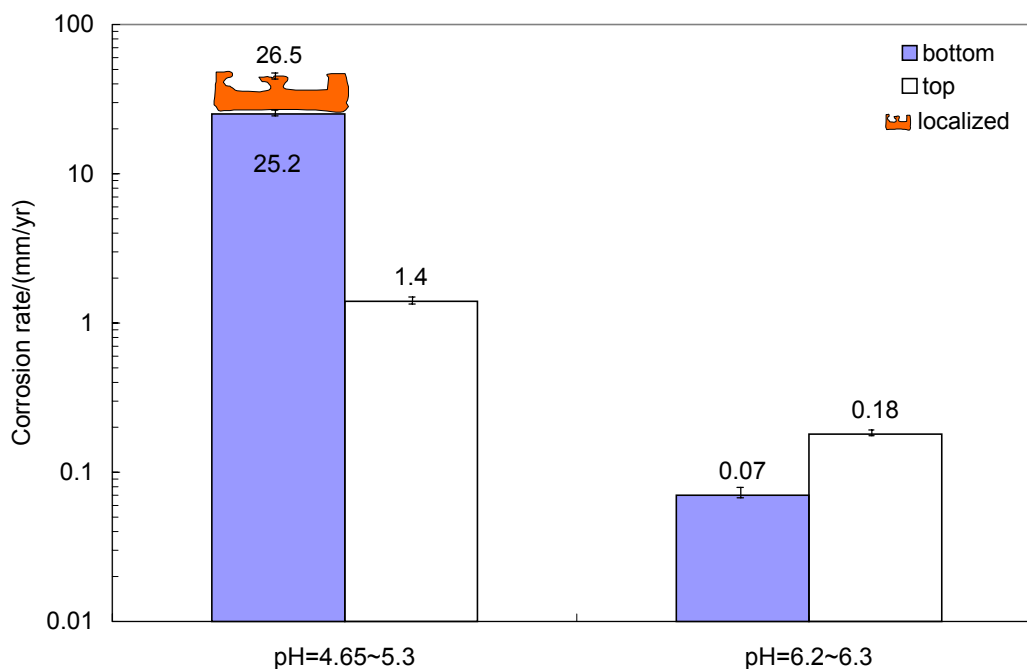


Figure 5.5.1 The effect of pH on the average and localized corrosion rate from WL X65 for 1% NaCl at $V_{sl} = 0.1$ m/s, $V_{sg} = 10$ m/s, $T = 90^{\circ}\text{C}$, and $P = 4.5$ bar ($P_{\text{CO}_2} = 3.8$ bar).

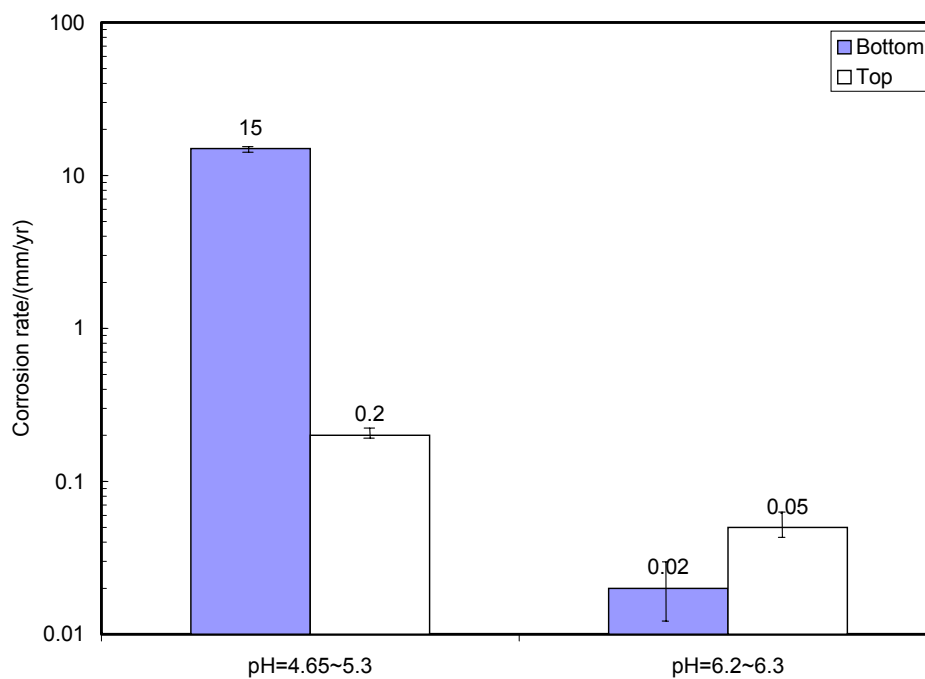


Figure 5.5.2 The effect of pH on the stabilized corrosion rate from ER method for 1% NaCl at $V_{sl} = 0.1$ m/s, $V_{sg} = 10$ m/s, $T = 90^{\circ}\text{C}$, and $P = 4.5$ bar ($P_{\text{CO}_2} = 3.8$ bar).

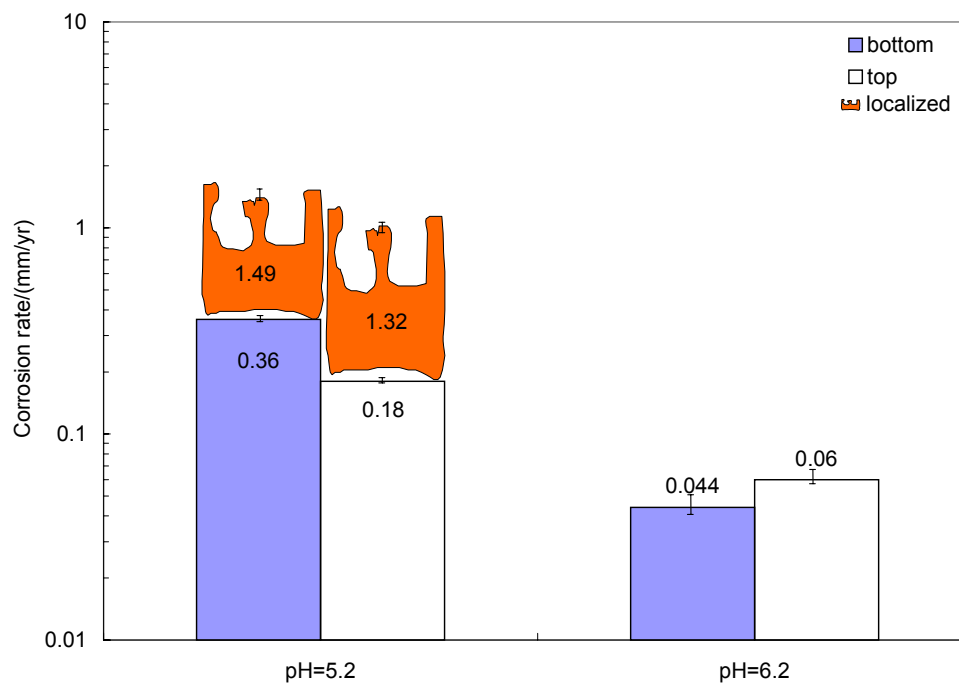


Figure 5.5.3 The effect of pH on average and localized corrosion rate from WL X65 for 1% NaCl at $V_{sl} = 0.1$ m/s, $V_{sg} = 10$ m/s, $T = 90^{\circ}\text{C}$, and $P = 11.3$ bar ($P_{\text{CO}_2} = 10.6$ bar).

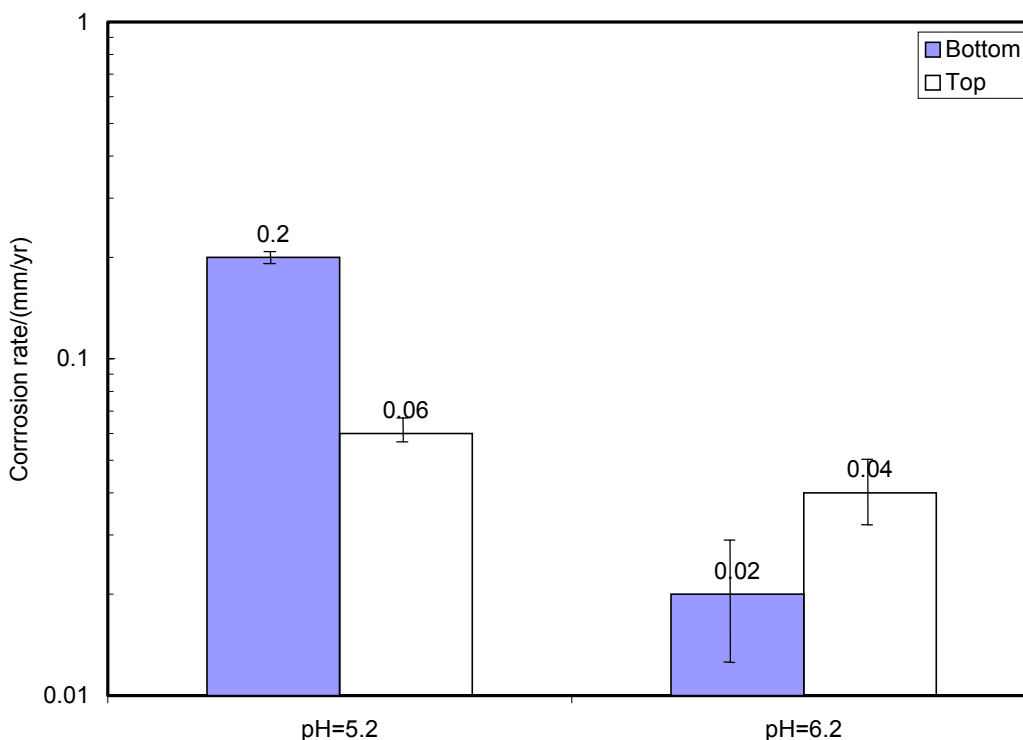


Figure 5.5.4 The effect of pH on stabilized corrosion rate from ER method for 1% NaCl at $V_{sl} = 0.1$ m/s, $V_{sg} = 10$ m/s, $T = 90^{\circ}\text{C}$, and $P = 11.3$ bar ($P_{\text{CO}_2} = 10.6$ bar).

A relatively low pH environment can apparently initiate the localized attack. Under the stratified flow regime, localized corrosion occurred only on the bottom as shown in Figure 5.5.1. The water on the top must have a different chemistry due to the condensation. However, when the water was spread around the pipe wall as in annular flow, which caused the same pH everywhere in the pipe, localized corrosion took place on both the top and bottom, as indicated in Figure 5.5.3. Thus the issue of whether the top of the line would suffer localized attack largely depends on the flow regime and the local pH. Under a high pH environment, localized corrosion was inhibited in both the top and the bottom in both flow regimes. The most important pH contribution is that it largely

affects species concentration in solution. This might further affect the solution supersaturation level and, finally, scaling tendency.

Uniform corrosion was also largely affected by the change of pH and flow regime. As can be seen from Figure 5.5.2 and Figure 5.5.4 with the stabilized corrosion rate (stable for more than 50 hours), the corrosion rates dropped dramatically with the increase of pH for both flow regimes. The corrosion rates on the top and the bottom were much closer to each other in annular flow, which is understandable due to the same water chemistry. The difference in corrosion rate from the top to the bottom might be attributed to the dissimilar water film velocities near the pipe wall.

Under stratified flow, the corrosion rate on the top was more than an order of magnitude lower than the bottom corrosion rate at low pH. On the contrary, at high pH, the corrosion rate on the top was more than a factor of two higher than the bottom corrosion rate. As addressed before, the top of line experienced more water condensation in stratified flow. The distinct water chemistry from the bottom to the top can explain the discrepancy in corrosion rate. However, the question arose: does the water on the top come entirely from condensation under the stratified flow regime? If the answer was yes, then one should not see any difference with the change of pH in the solution, given that all the other test parameters remain the same, for example, superficial velocities, temperature, pressure etc. The condensed water on the top should not be able to “sense” the pH change in the bulk water at the bottom. Nevertheless, in Figure 5.5.2, the corrosion rate actually decreased a factor of four when the pH was increased. This suggests that a portion of the water on the top must be from the water droplets that have the same pH as the bulk water. Thus the issue “where the water is from” on the top of the

line in stratified flow can now be resolved. The answer is: it is from both condensation and water droplet impingement.

In the oil and gas industry, a pH of 4 to 6 is of primary practical interest since it represents the majority of environments in pipeline transportation. Since localized corrosion is of large concern, pH stabilization technique should be considered as a method to combat it.

5.6 The Effect of Flow in Wet Gas

Flow is another major factor affecting corrosion by increasing the transport of species involved in the corrosion process or by mechanical removal of the corrosion product film. Flow is described below by the individual phase flow rates and by the flow regimes.

5.6.1 The Effect of Flow Velocity at 40°C

The effect of the superficial gas and liquid velocities on corrosion was tested at different CO₂ partial pressures. The results are shown in Figure 5.6.1 and Figure 5.6.2.

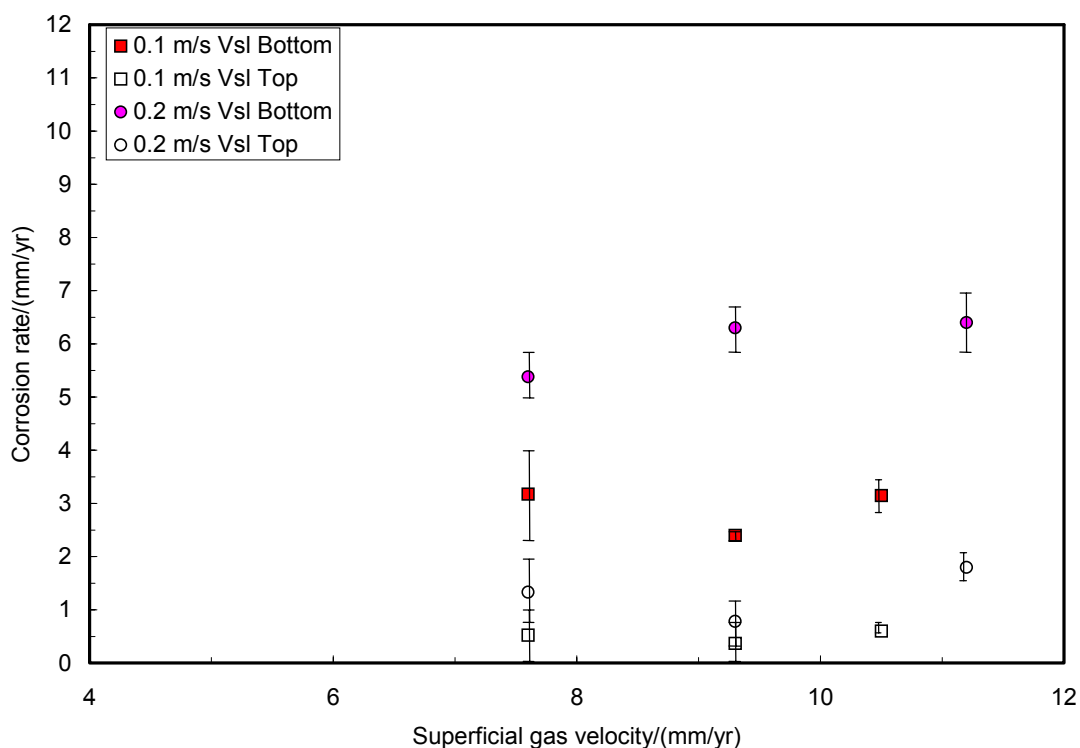


Figure 5.6.1 The effect of superficial velocities on corrosion at 40°C with 100% water cut under CO₂ partial pressure of 3.8 bar.

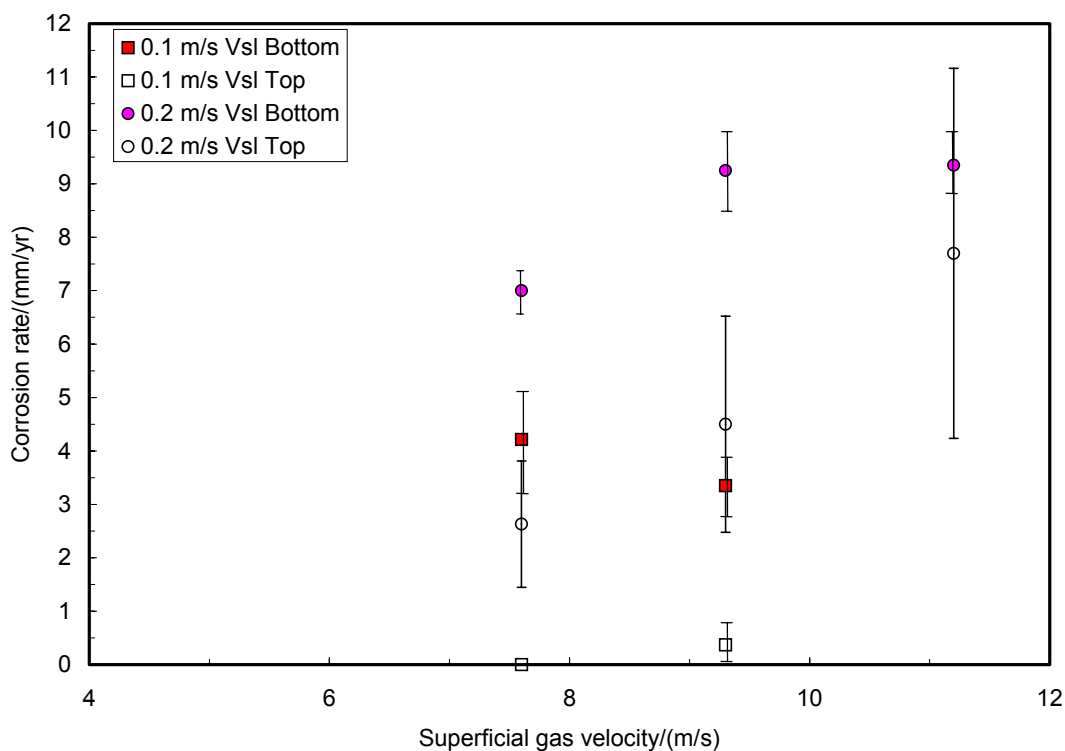


Figure 5.6.2 The effect of superficial velocities on corrosion at 40°C with 100% water cut under CO₂ partial pressure of 7.8 bar.

The error bars in the above figures represent the maximum and the minimum corrosion rates obtained in the experiments while the data point represents the mean value of the experimental results. Although the superficial gas velocity was only tested within a small range, from 7 m/s to 11 m/s, the results indicated that the increase in gas velocity caused an increase in the corrosion rate for both the top and the bottom of the pipe. This might be due to the enhanced turbulence (more mixing) in the liquid film induced by the faster gas flow velocity.

The corrosion rate also increased with an increase in superficial liquid velocity. The superficial liquid velocity was tested from 0.1 m/s to 0.2 m/s. An increased liquid flow rate causes more water to be present in the pipe and introduces a higher mass

transfer rate. The 0.2 m/s liquid flow rate allowed sufficient water to be present for spreading of the liquid film around the pipe wall to form annular flow. Therefore, the corrosion rate at the top was large. The corrosion rate change at higher velocity (0.2 m/s) and higher CO₂ partial pressure (7.8 bar) was more apparent when compared to the lower velocity (0.1 m/s) and lower CO₂ partial pressure (3.8 bar).

No localized corrosion was identified at any of the flow conditions tested for both the top and the bottom of the pipe. Since there was no formation of corrosion product films, flow affects the corrosion only through the mass transport process within the boundary layer.

5.6.2 The Effect of Flow Velocity at High Temperature of 90°C

Two groups of tests were performed to identify the effect of superficial gas velocity on localized corrosion at high temperature. One was under 3.8 bar CO₂ partial pressure with the gas velocity ranging from 6 m/s to 20 m/s. The test loop was seriously contaminated by lead and an unknown black material. The absolute results were dubious, and the effect of lead on corrosion was further investigated. The results were presented in the Corrosion Center's advisory board meeting (Sun, 2001) and are not included in this dissertation.

Another group of tests was performed under a CO₂ partial pressure of 10.6 bar and superficial gas velocities of 5 m/s and 10 m/s at pH of 5.2. These results were valid, and the 10 m/s test was already reported and referred to as the high-pressure, low-pH test in section 5.4.

Low velocity of 5 m/s V_{sg} test under high pressure and low pH environment

The pressure drop was monitored during the experiment, and the resulting average pressure drop was around 33.4 Pa/m, which suggested the flow is in the stratified flow regime. The evolution of the corrosion rate was recorded through the test, as shown in Figure 5.6.3.

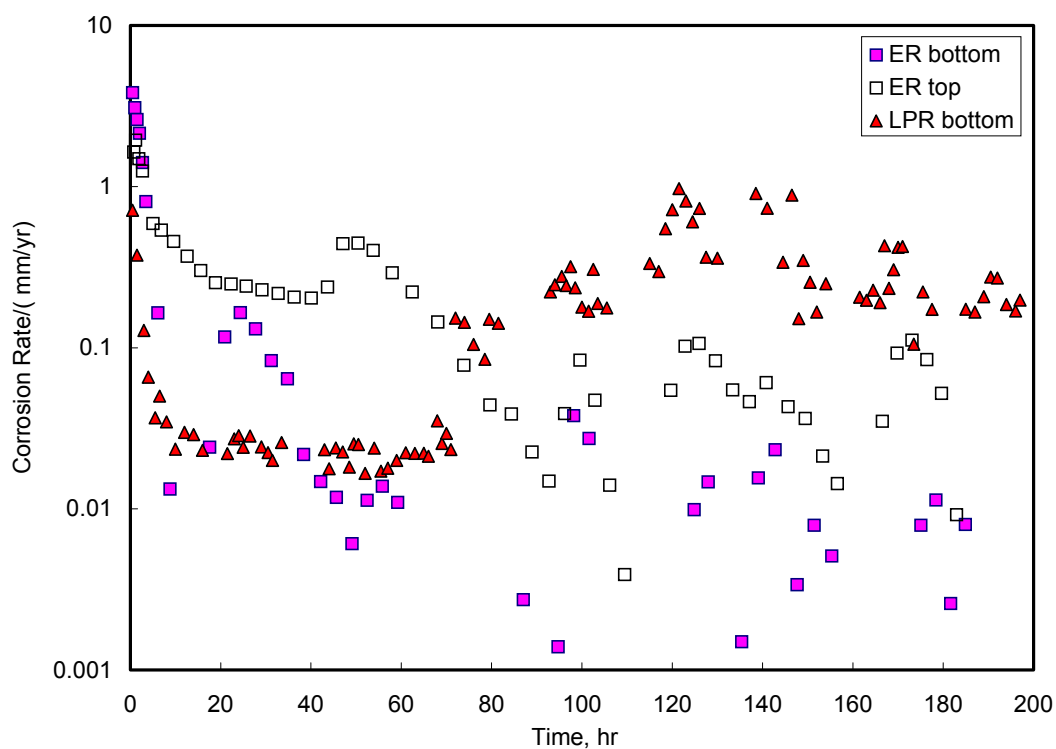


Figure 5.6.3 The change of corrosion rate with time for 1% NaCl at $V_{sl} = 0.1$ m/s, $V_{sg} = 5$ m/s, $T = 90^{\circ}\text{C}$, $P = 11.3$ bar ($P_{\text{CO}_2} = 10.6$ bar), and $\text{pH} = 5.2$.

In the first 60 hours, the change of corrosion rate obeyed the same law as all the other tests, with a high initial corrosion rate and then a decreased corrosion rate with time. But after 60 hours, the ER and LPR measurements on the bottom started to deviate from each other, and the bottom ER results appeared to be very scattered. It was

suspected that the probe might have suffered from some sort of failure or a connection problem. Fortunately, a third technique with weight loss measurements was used and the results are shown in Figure 5.6.4. From weight loss analysis, it is seen that the top ER measurement and bottom LPR measurement can be used, while the bottom ER result had to be discarded. WL measurements also indicated comparable corrosion rates at the bottom and the top, which was totally different from stratified flow in the low-pressure tests. Since the flow was in a stratified flow regime, condensation occurred on the top of the line. Under high CO₂ partial pressure, the pH on the top could be much lower than the bulk pH. This could explain the appearance of localized attack on the top in this test.

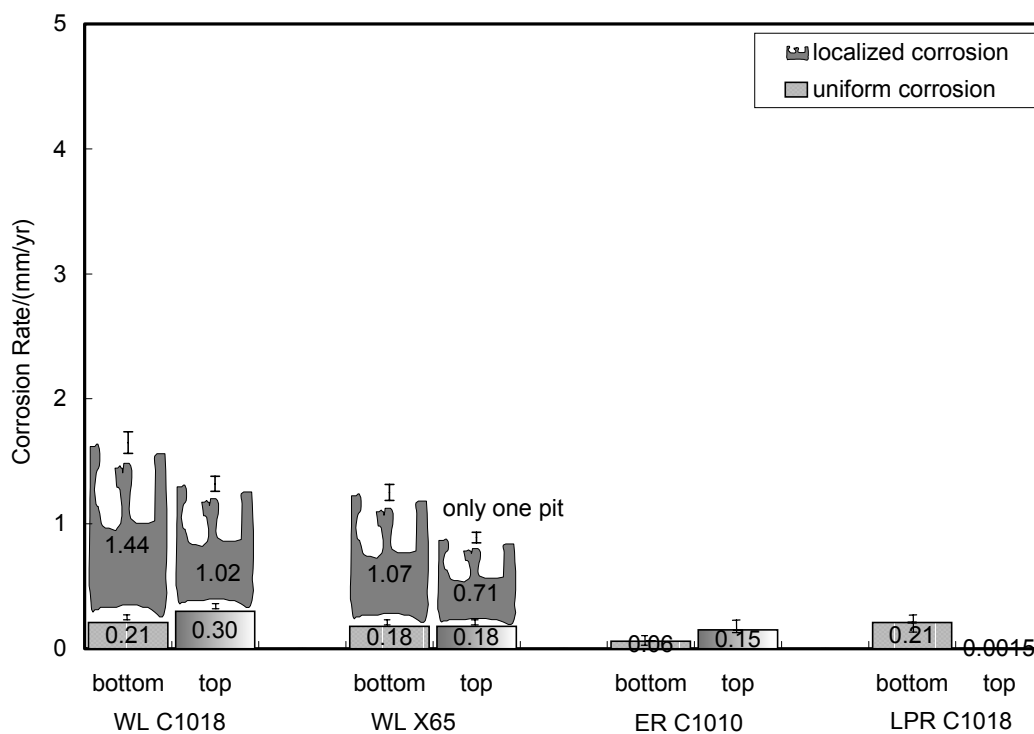


Figure 5.6.4 The average and localized corrosion rate from different methods for 1% NaCl at $V_{sg} = 5$ m/s, $V_{sl} = 0.1$ m/s, $T = 90^{\circ}\text{C}$, $P = 11.3$ bar ($P_{\text{CO}_2} = 10.6$ bar), and $\text{pH} = 5.2$.

Once again, localized corrosion occurred on both materials for both the top and the bottom of the pipe, as shown in Figure 5.6.4. The number of the pits was also reduced with the decrease in flow velocity; for example, only one pit was found in the top X65 specimen. The specimen surface under SEM shown in Figure 5.6.5 revealed that a more protective film formed on the top surface than the high velocity test. No localized corrosion was detected on the top specimen in cross sectional analysis, as shown in Figure 5.6.6. However, MM detected a couple of pits on the surface. The bottom specimen showed clear localized corrosion with few pits.

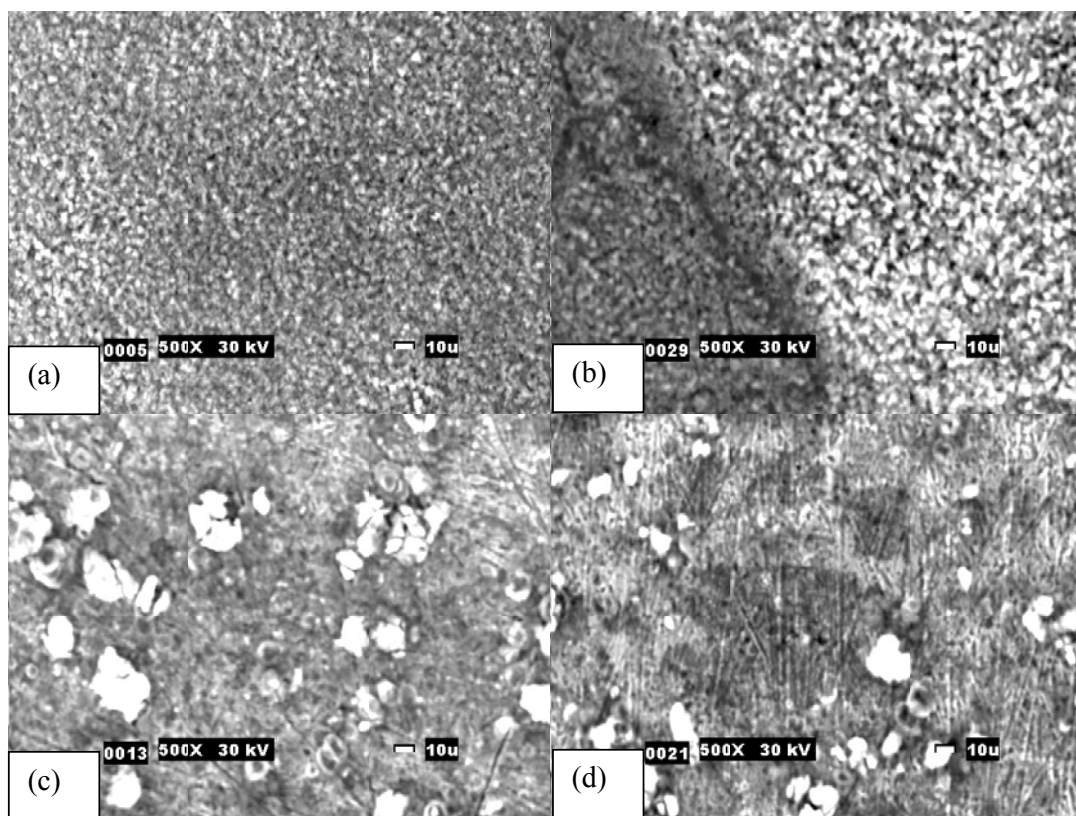


Figure 5.6.5 SEM micrographs for 1% NaCl at $V_{sg} = 5$ m/s, $V_{sl} = 0.1$ m/s, $T = 90$ °C, $P = 11.34$ bar ($P_{CO_2} = 10.64$ bar), and $pH = 5.2$. (a) top C1018; (b) top X-65; (c) bottom C1018; (d) bottom X65.

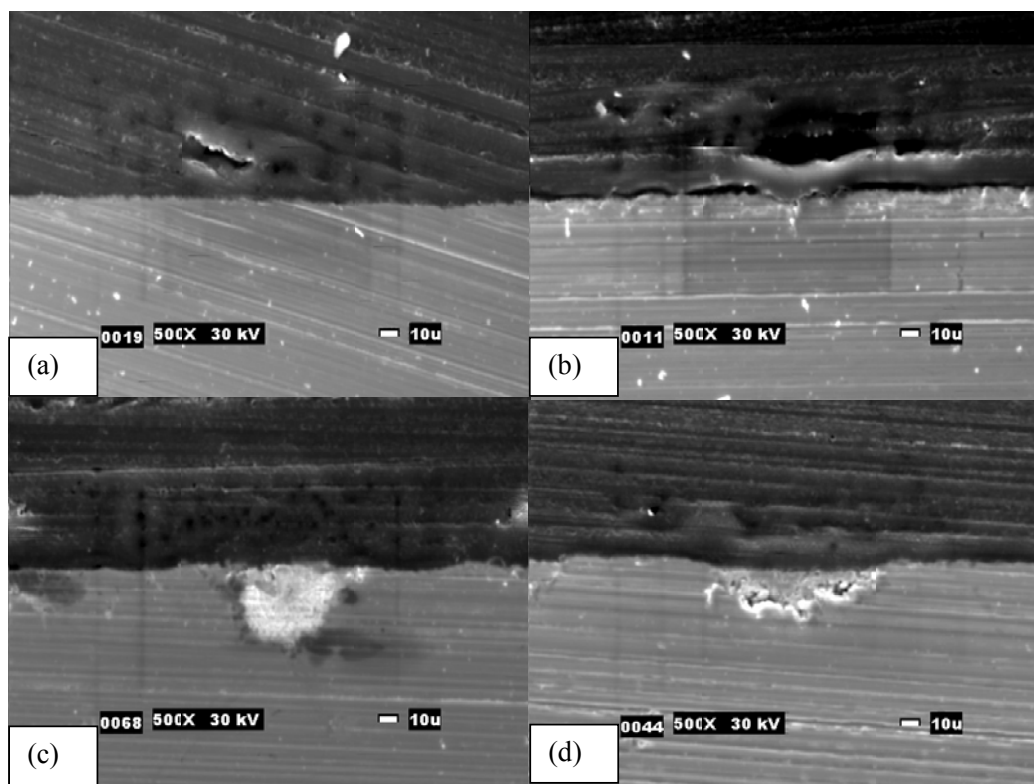


Figure 5.6.6 Cross sections for 1% NaCl at $V_{sg} = 5$ m/s, $V_{sl} = 0.1$ m/s, $T = 90$ °C, $P = 11.3$ bar ($P_{CO_2} = 10.6$ bar), and $pH = 5.2$. (a) top C1018; (b) top X-65; (c) bottom C1018; (d) bottom X65.

Discussions on the effect of velocity

The effect of superficial gas velocity on corrosion under the high pressure of 11.3 bar is shown in Figure 5.6.7. It is seen that localized corrosion took place on both the top and the bottom for both velocities under controlled pH of 5.2. However, it was also observed that the pitting density or the number of pits was greatly decreased when the gas velocity was reduced from 10 m/s to 5 m/s. For example, only one pit was found on the top X65 and bottom C1018 at 5 m/s. The total amount of pits were all less than 10 on both materials, even at the bottom of the pipe. One can then infer that a critical velocity must exist below which no localized corrosion will occur.

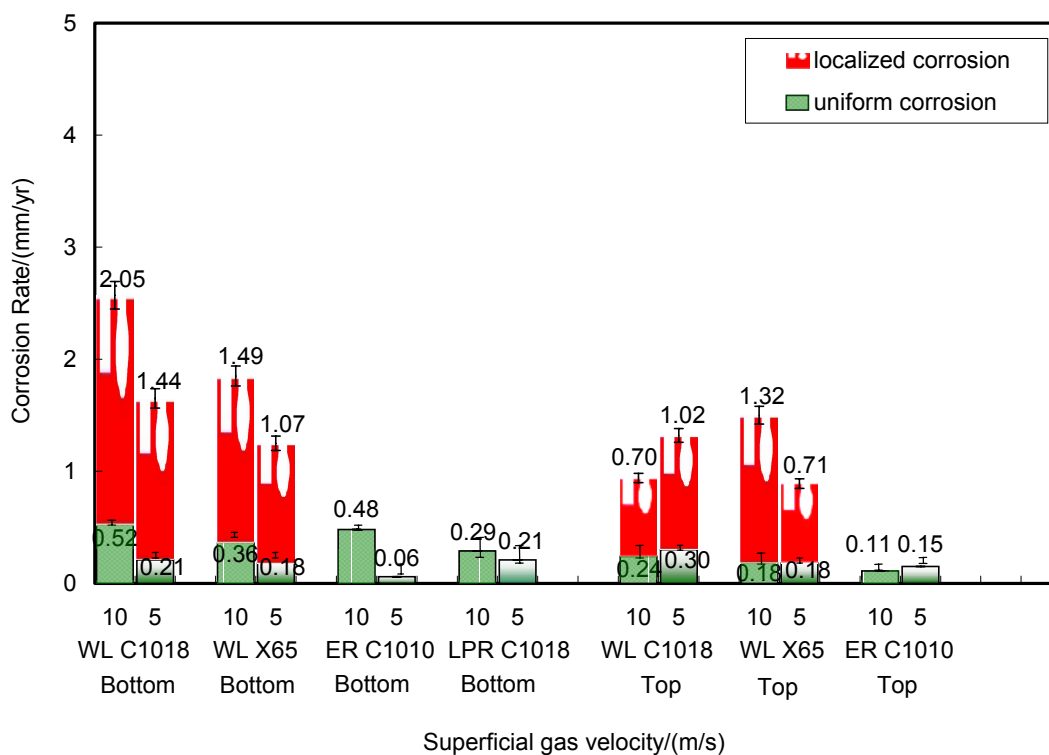


Figure 5.6.7 The effect of superficial gas velocity on the corrosion rate from different measurement techniques at pH = 5.2 for 1% NaCl at $V_{sl} = 0.1$ m/s, $T = 90^{\circ}\text{C}$, and $P = 11.3$ bar ($P_{\text{CO}_2} = 10.6$ bar).

It was noticed that the corrosion behavior was distinct from the top to the bottom when the velocity changed. At the bottom of the pipe, the severity of both localized corrosion and uniform corrosion was alleviated when the gas velocity was reduced. This is explainable since the higher velocity causes more turbulent flow, which means the occurrence of a higher mass transfer rate for the corrosive species and corrosion product to and from the metal surface (Nesic et al., 2001). However, on the top of the pipe, no major difference existed when the velocity changed, as reflected by all the measurement techniques. As mentioned earlier, the flow regime influenced this test. Under a pressure of 11.3 bar, 10 m/s gas velocity led to annular flow formation, which means the top water

has the same pH of 5.2 as the bottom water, while a 5 m/s gas velocity led to stratified regime, which caused a different water chemistry from the bottom to the top. One might recall that in the so-called low pressure, low pH test, the flow was also in stratified flow, and no localized corrosion was found on the top of the line. The condensed water was such a small amount that it was saturated quickly by the corrosion product and resulted in a low corrosion rate and protection from localized attack. However, under high CO₂ partial pressure, the pH in the pure condensing water must be very low. The low pH can initiate the localized attack, as addressed earlier in this report. In summary, pH once again showed its leading role in CO₂ corrosion, including localized attack.

5.6.3 The Effect of Flow Regime

The previous sections have involved discussions with flow patterns and their effects on top of the line corrosion. The bottom of the line is always in contact with a liquid phase, and water chemistry is always important. The top of the line does not have a liquid film in a stratified flow regime, thus the condensation had to be considered in some of the cases. The experimental findings indicated that the individual phase flow rate and the system pressure were closely related to the flow patterns, as shown in Figure 5.6.8.

It was seen that increasing the superficial liquid or gas velocity or the system pressure caused the flow regime transition from stratified flow to annular flow. The last case with uniform distribution of liquid film thickness is almost unachievable in horizontal pipes due to the gravitational effect.

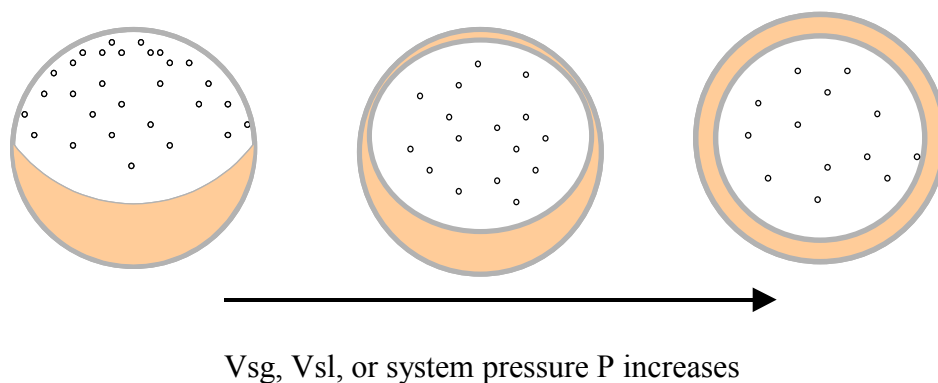


Figure 5.6.8 The schematic flow pattern transitions with superficial velocities and system pressure.

The annular flow that occurred in the experiments was always considered to be accompanied by non-uniform distribution of liquid film thickness from the top to the bottom of the pipe, thus resulting in a non-uniform distribution of the actual flow velocity in the near-wall region from the top to the bottom. However, it was observed during the experiments that the corrosion behavior (including both uniform corrosion and localized corrosion) was getting closer for both the top and the bottom in annular flow, most probably because they had the same water environment. On the contrary, the corrosion behavior could be distinguished from the top to the bottom when the flow was in stratified flow regime. Other system parameters, such as CO₂ partial pressure, temperature, and condensation rate (the research only considered small condensation without significant cooling) then became crucial. Therefore, it is imperative to understand the flow regime in wet gas service.

5.7 The Effect of Oil in Wet Gas Flow

Tests were performed to study the effect of oil on wet gas corrosion. The test matrix is shown in Table 5.7.1. LVT 200 oil has a viscosity of 3 cP and a density of 820 kg/m³ at room temperature. The average pressure drop was around 60 Pa/m, and the flow annular. The pH was measured as approximately 5.0 during the test.

Table 5.7.1 The test matrix for the effect of oil on corrosion.

Liquid phase	80% water (no NaCl), 20% (v:v) LVT oil
Total pressure	4.5 bar
CO ₂ partial pressure	3.8 bar
Temperature	90°C
Superficial liquid velocity	0.05 m/s
Superficial gas velocity	15, 20 m/s
Material tested	C1018, C1010
Measurement techniques	ER, WL

5.7.1 Results on The Effect of Oil

The results from the above two tests are presented together below. The change of corrosion rate with exposure time for both the top and the bottom are shown in Figure 5.7.1. It appeared that for all test conditions, the change of corrosion rates with time had a shape similar to the tests without the oil phase. The corrosion rates decreased rapidly in the first 25 hours and followed a slow further decrease for up to about 50 hours exposure time. Due to the corrosion product film built-up (as can be seen in SEM analysis below), after about 50 hours, the corrosion rates remained almost constant at a comparably low level of below 0.5 mm/year. This indicated that the corrosion product films were very effective in preventing corrosion.

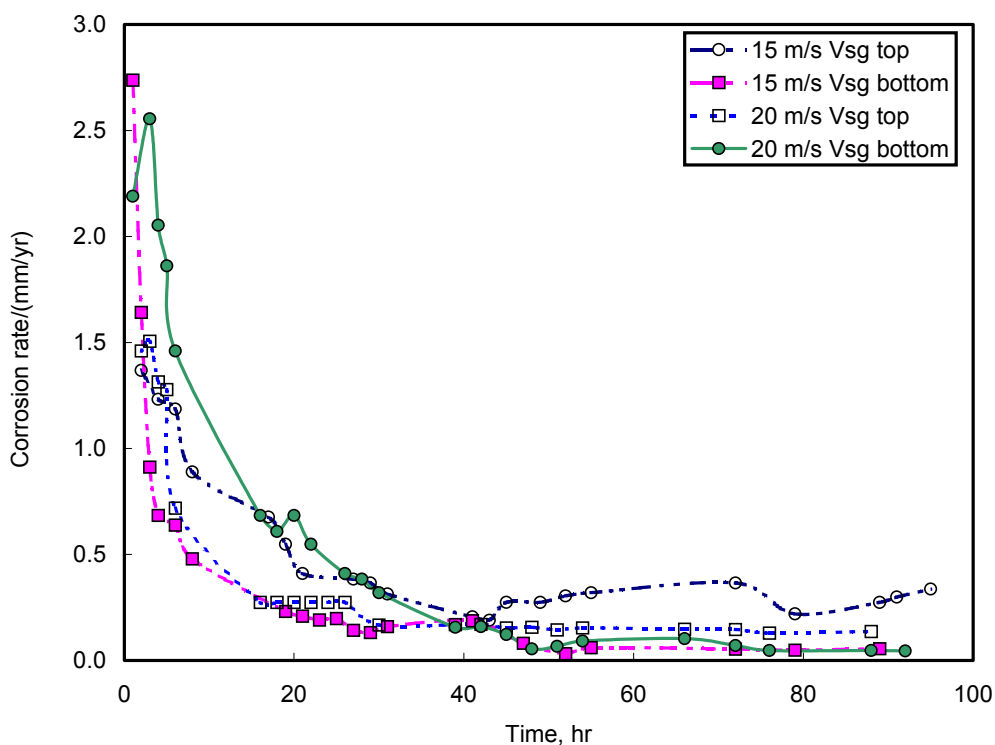


Figure 5.7.1 The change of corrosion rate with time from ER measurement at 80% water cut with $V_{sl} = 0.05$ m/s, $T = 90^{\circ}\text{C}$, and $P = 4.5$ bar ($P_{\text{CO}_2} = 3.8$ bar).

The results obtained were in a good agreement with some unpublished results (Hong, 2001). At elevated temperature (90°C) and pressure (21 bar) in ASTM saltwater and LVT 200 oil under full pipe flow, it was found that the corrosion product film became more compact after longer exposure times. After 10 hours, the growth of the film tended to be stable. This implies a highly intensive film growth with a decrease of the film porosity during the first 10 hours of exposure and an equilibrium behavior afterwards.

Figure 5.7.2 shows the average corrosion rates obtained from coupon weight loss measurements. Three coupons were weighed after film removal for each test. The

columns represented the average value for each test condition while the error bars indicated the highest and lowest values among the three measurements. The results confirmed the ER corrosion rate measurements in Figure 5.7.1, showing comparable corrosion rates at the bottom for 15 m/s V_{sg} and 20 m/s V_{sg} , and slightly increased values for the top of the pipe.

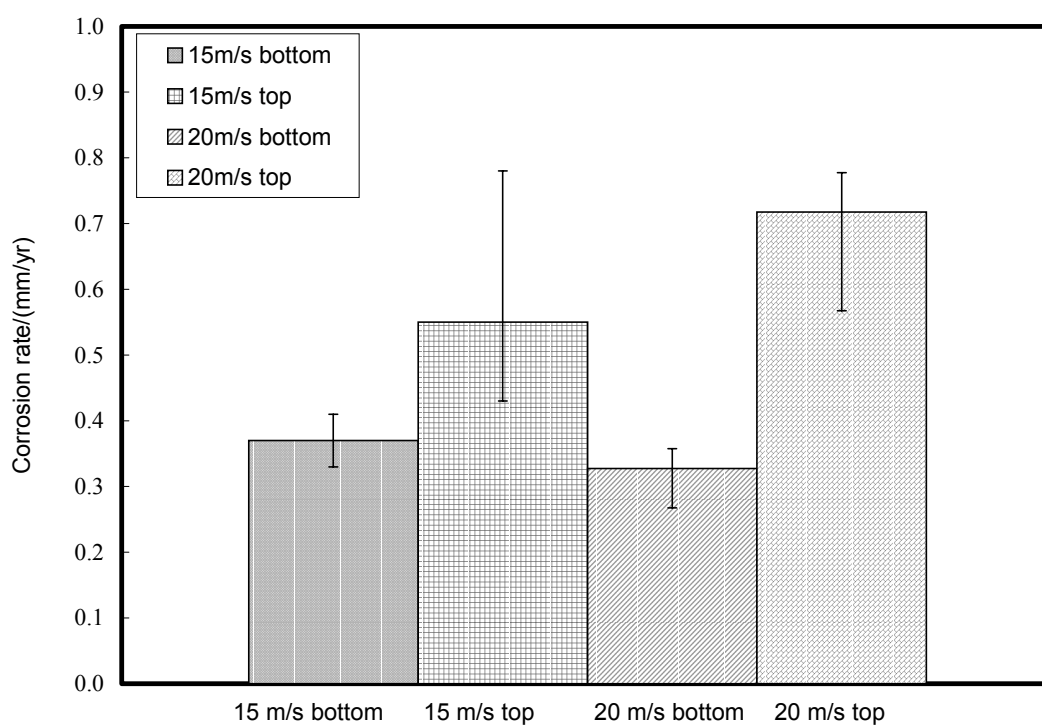


Figure 5.7.2 Average corrosion rate from WL measurement at 80% water cut with $V_{sl} = 0.05$ m/s, $T = 90^{\circ}\text{C}$, and $P = 4.5$ bar ($P_{\text{co}_2} = 3.8$ bar).

It is noticed from Figure 5.7.1 and Figure 5.7.2 that for both test conditions, the corrosion rate at the top was slightly increased compared to the bottom corrosion rate. This was due to different liquid film thickness and velocities in horizontal annular flow,

which resulted in the growth of iron carbonate films with different film properties on the top and bottom of the pipe, as can be seen from Figure 5.7.3.

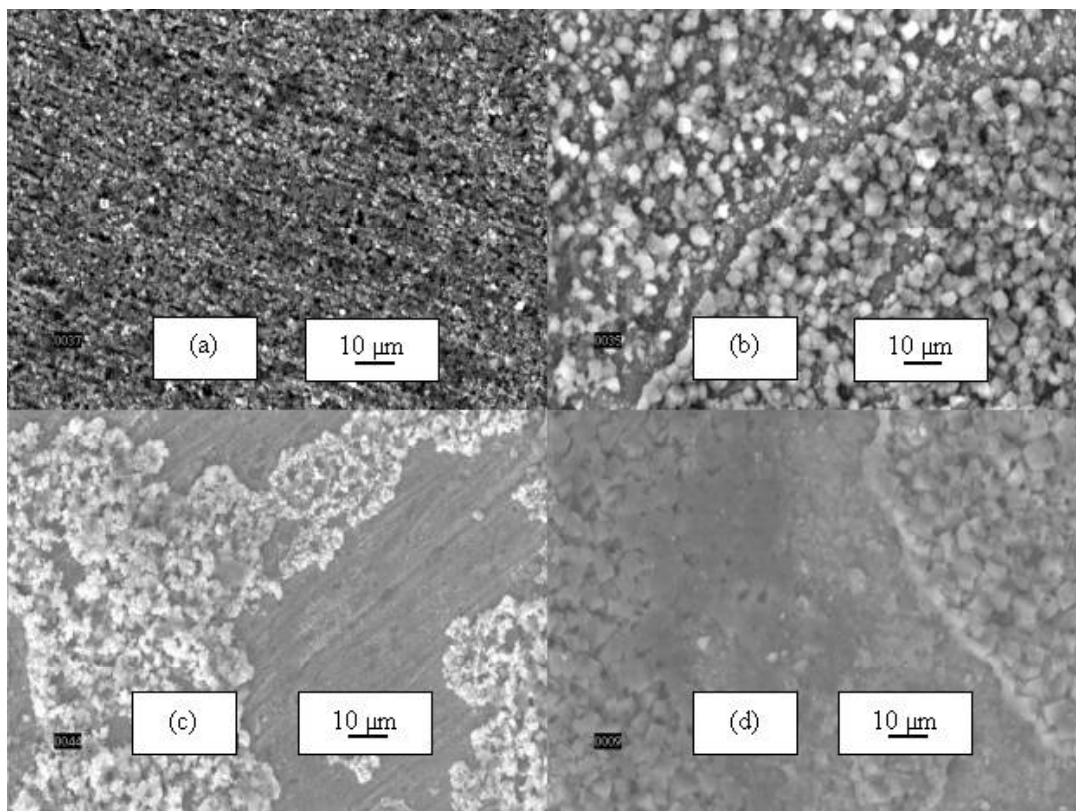


Figure 5.7.3 SEM micrographs for coupons at $V_{sl} = 0.05$ m/s, $T = 90$ °C and $P = 4.5$ bar ($P_{CO_2} = 3.8$ bar). (a) $V_{sg} = 15$ m/s bottom; (b) $V_{sg} = 15$ m/s top; (c) $V_{sg} = 20$ m/s bottom; (d) $V_{sg} = 20$ m/s top.

Compared with the crystals (confirmed as $FeCO_3$ film from XRD analysis) formed on the top coupon ($\sim 3\text{-}4$ μm), a smaller average crystal size ($\sim 1\text{-}2$ μm) can be observed at the bottom, yielding a more compact film structure with decreased porosity. In horizontal annular flow with very low liquid content (0.05 m/s), the liquid film can always cover the bottom of the pipe while the top of the pipe may not get a continuous film all of the time. In addition, the liquid film thickness at the bottom was increased

compared to the top due to gravitational effects, resulting in a lower local film velocity at the bottom of the pipe. Consequently, a more uniform corrosion product film formation and growth at the pipe bottom was facilitated.

At an enhanced gas velocity of 20 m/s, the topography of the film formed on the top specimen became more uneven. The film morphology at the bottom exhibited different plateaus. The raised areas patch together and show a higher porosity and increased surface roughness. The lower plateaus were smoother and appeared to be topographically grown. XRD analysis detected only high intensity iron peaks on the bottom specimen due to the very thin film. Further XPS analysis was applied on the same specimen since XPS can provide elemental and chemical state identification for atoms located at the top atomic layers of the sample investigated (Smith, 1994). Figure 5.7.4 shows Fe 2p, O 1s and C 1s peaks in the XPS spectrum. The atomic ratio of Fe and O was found to be about 1:3, the carbon content was comparably high, most probably due to an insufficient removal of the hydrocarbon phase, resulting in some carbon contamination of the surface of the corrosion product scale.

These results were in accordance with observations reported in the literature (Olsen and Dugstad, 1991, Palacios and Shadley, 1991). At comparable temperatures, the films formed in a CO₂ environment were usually thin (< 30 μm), compact and highly adherent, which was always related to a pronounced reduction of the corrosion rate (Palacios and Shadley, 1991). Once protective scales form at temperatures around 80 °C, they appear very robust and resistive even under severe flow conditions (Olsen and Dugstad, 1991).

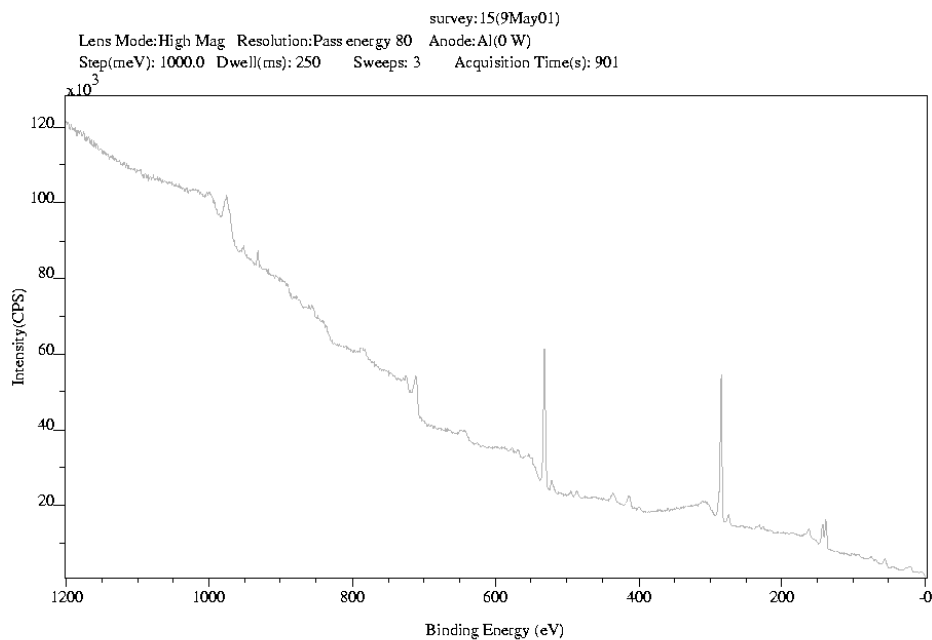


Figure 5.7.4 XPS spectrum for bottom coupons at $V_{sl} = 0.05$ m/s, $V_{sg} = 20$ m/s, $T = 90$ °C and $P = 4.5$ bar ($P_{CO_2} = 3.8$ bar).

Generally, thin, compact films exhibit much higher resistance against flow induced corrosion attack than thick, porous scales. Figure 5.7.5 shows that the iron carbonate film thickness for both top and bottom is less than 10 microns for 15 and 20 m/s V_{sg} and in some areas even as low as about 1 micron. The film exhibited a good adherence to the metal substrate and shows a low porosity, which are the preconditions for high protection. No indications for the initiation of localized corrosion were found for the test conditions investigated. Thus, the observed corrosion rates were low. A slightly higher degree of roughness at a V_{sg} of 20 m/s possibly increases the risk for the initiation of localized attack at extended exposure times, which is intended to be confirmed by further experimental work.

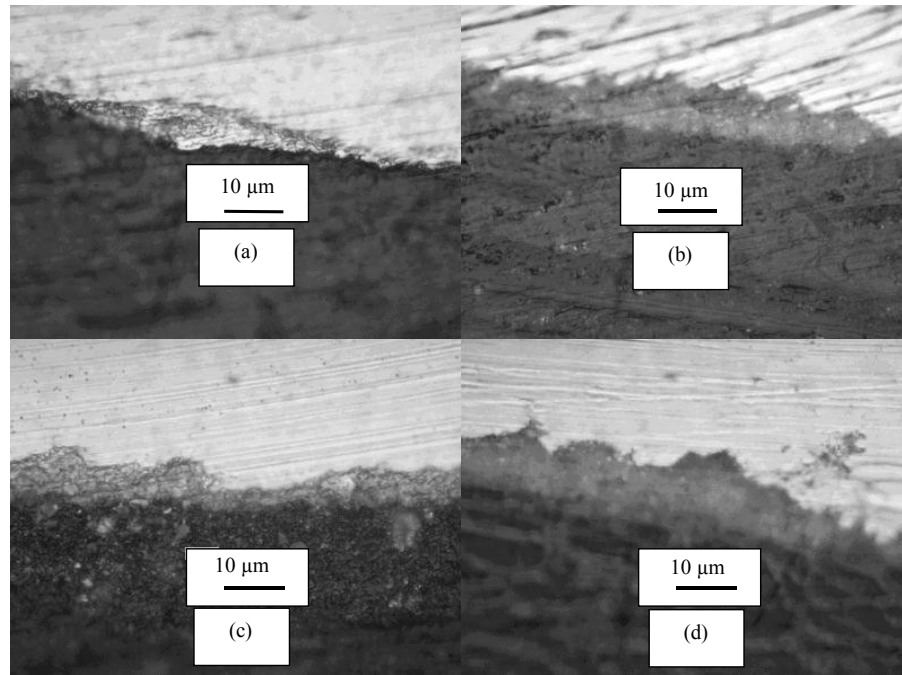


Figure 5.7.5 Cross sections for coupons at $V_{sl} = 0.05$ m/s, $T = 90$ °C and $P = 4.5$ bar ($P_{CO_2} = 3.8$ bar). (a) $V_{sg} = 15$ m/s bottom; (b) $V_{sg} = 15$ m/s top; (c) $V_{sg} = 20$ m/s bottom; (d) $V_{sg} = 20$ m/s top.

5.7.2 Discussion on the Effect of Oil

In experiments with horizontal annular flow under wet gas CO_2 corrosion of plain carbon steel in DI water and a hydrocarbon mixture (80:20 vol.-%) at superficial gas velocities of 15 and 20 m/s and a superficial liquid velocity of 0.05 m/s at 90°C, the stabilized corrosion rate varied between 0.05 and 0.25 mm/yr for at least 50 hours, depending on the gas flow rate and on the position in the pipe. A similar system without an oil phase at a lower gas velocity of 10 m/s and a higher liquid velocity of 0.1 m/s had given a much higher stabilized corrosion rate from 0.49 mm/yr to up to 13 mm/yr for at least 40 hours. The comparison is shown in Figure 5.7.6.

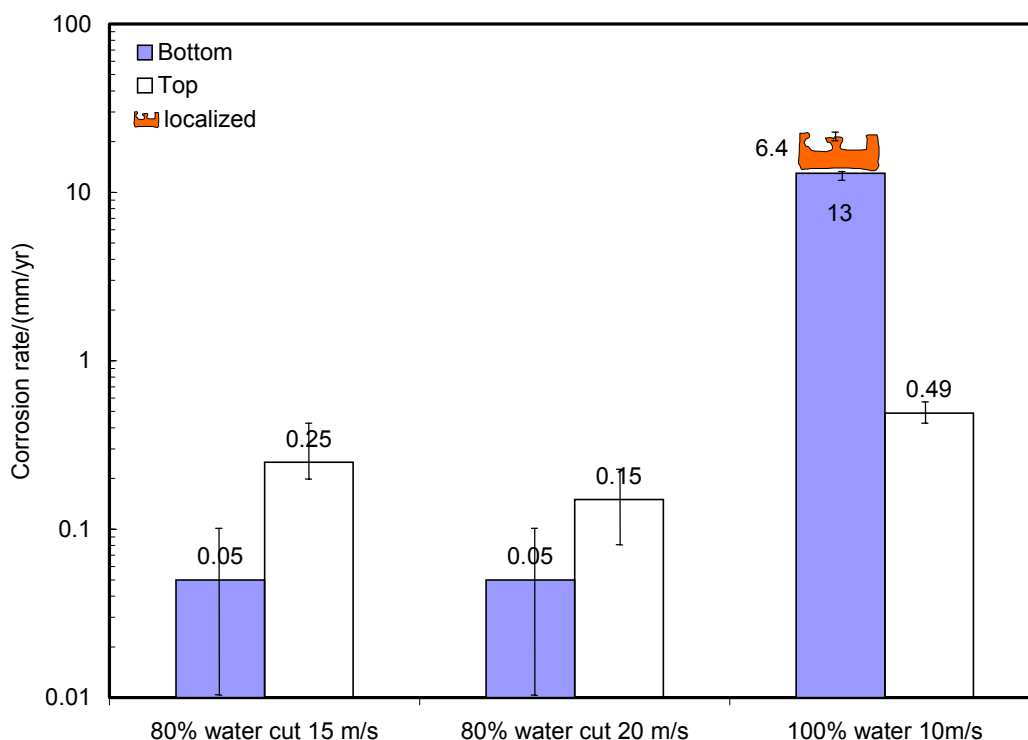


Figure 5.7.6 The effect of oil on the stabilized corrosion rate from ER method in pure water and water/oil system with different velocities at 90°C and P = 4.5 bar ($P_{\text{CO}_2} = 3.8$ bar).

In addition, no localized corrosion was identified in the system with 80% water cut while it did occur in the system without an oil phase. In a 80% water cut environment, the corrosion rate at the top of the pipe was slightly increased compared to the bottom of the pipe due to the local difference of the liquid film thickness in a horizontal annular flow regime, which resulted in the reduction of the protectiveness of the iron carbonate corrosion product scales formed at the top of the pipe. In a pure water system, the gas flow rate was much lower, resulting in formation of stratified flow. The corrosion rate on the top was much smaller than that on the bottom due to the formation of a protective film at low condensation rates.

Therefore, the formation of a thin (< 10 microns) protective iron carbonate layer in 80% water cut systems was responsible for comparably low corrosion rates and protection from localized corrosion even at higher gas transportation capacities. The presence of a hydrocarbon phase exhibits a favorable effect even in non-inhibited wet gas transportation systems allowing acceptable gas flow rates when annular flow was maintained.

CHAPTER 6: PHYSICO-CHEMICAL MODEL DEVELOPMENT

6.1 Introduction

In Chapter 5, the various global parameters affecting the localized corrosion, such as the temperature, pressure, flow, pH, and Cl^- etc. intensively studied over a large range were discussed. In order to understand the effect of individual parameters on localized corrosion, other test parameters had to be kept constant during the experiments to prevent the intertwining effects of the corrosion phenomena. Therefore, the results from each experiment are rather isolated and lose universal applications. To model the localized corrosion in wet gas service and to generalize the results for a practical application in the oil and gas industry, a more intrinsic characteristic that unifies all the experimental findings has to be found.

After reviewing all the tests, it was found that the initially proposed assumptions about occurrence of uniform and localized corrosion have been validated throughout the experiment results. The graphical interpretation of the three assumptions is shown in Figure 6.1.

no film	partially protective film	fully protective film
High uniform attack	Low/high uniform attack	Low uniform attack
No localized attack	Localized attack	No localized attack

Figure 6.1 The graphical illustration of the three hypotheses related to localized corrosion.

The two extreme conditions, result in only uniform corrosion. Localized corrosion may occur in a so-called “gray zone,” where the corrosion product film is formed but cannot offer satisfactory protection. For more practical reasons, knowing the risk of localized corrosion (gray zone) is probably more important than knowing the magnitude of the localized corrosion rate. Hence, the model development will focus on identifying the possibility of occurrence of localized corrosion. Under fixed temperature and pressure conditions, localized corrosion seems to be closely related to the solution properties, such as the iron super saturation level and the scaling tendency. This chapter is dedicated to exploring the link between the localized corrosion and these solution properties.

6.2 Super Saturation (SS) Level And Localized Corrosion

As described in Chapter 2, the iron super saturation level (SS) is defined as follows:

$$SS = \frac{[Fe^{2+}][CO_3^{2-}]}{K_{sp}} \quad (6-1)$$

where, $[Fe^{2+}]$ represents the equilibrium ferrous ion concentration in mol/l, which was experimentally measured in each test; $[CO_3^{2-}]$ represents the equilibrium concentration of carbonate ion in mol/l, which was computationally determined; K_{sp} is the solubility product of iron carbonate, which is a function of temperature and solution ionic strength expressed as (<http://www.nts.no/norsok>):

$$pK_{sp} = 10.13 + 0.0182 * T - 2.44 * I^{0.5} + 0.72 * I \quad (6-2)$$

where, T is the temperature in Celsius and I is the ionic strength in mol/l. The ionic strength is defined by G.N. Lewis as (Daniels and Alberty, 1995):

$$I = \frac{1}{2} \sum_i m_i z_i^2 = \frac{1}{2} (m_1 z_1^2 + m_2 z_2^2 + \dots) \quad (6-3)$$

where m is the species concentration in mol/l, and z is the species charge.

In most of the tests, the solution chemistry changed more or less from the beginning to the end of the test due to iron dissolution. Thus, the super-saturation level at both the beginning and the end of the test were calculated separately for each test. The relationship between the super-saturation level and localized corrosion is plotted in Figure 6.2, Figure 6.3, and Figure 6.4.

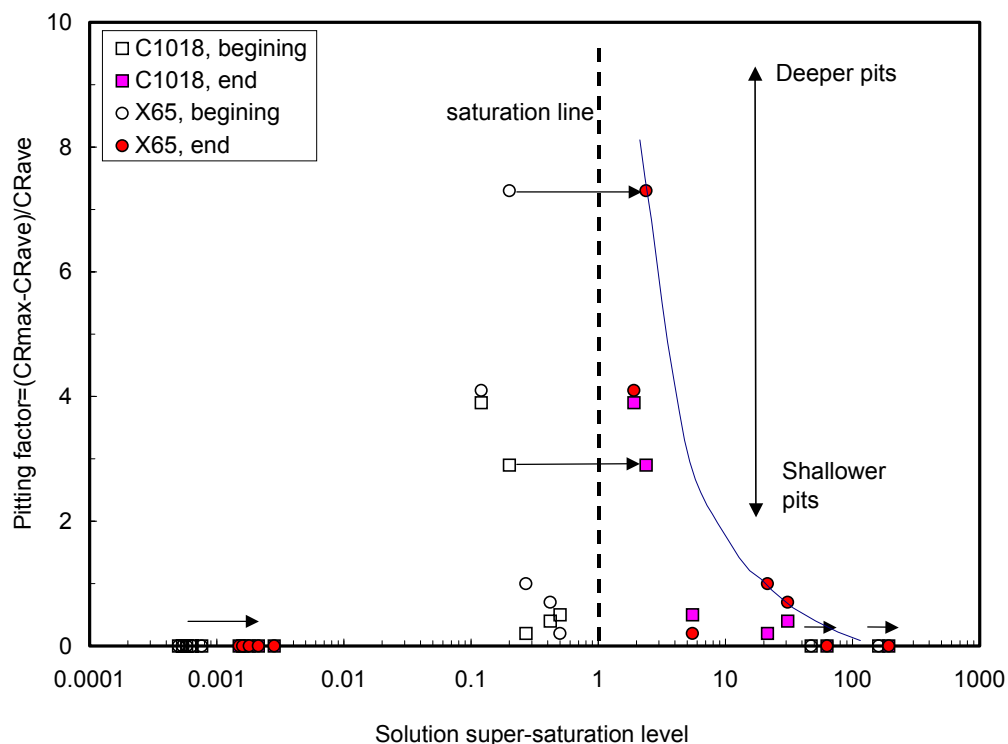


Figure 6.2 The relationship between the super saturation level and the pitting factor for all experiments.

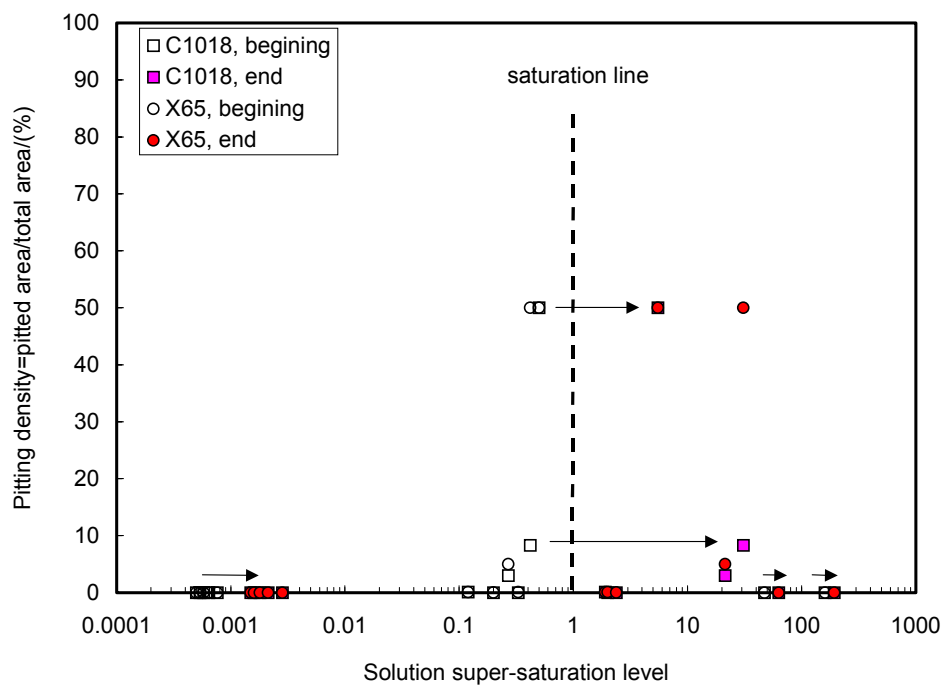


Figure 6.3 The relationship between the super-saturation level and the pitting density for all the experiments.

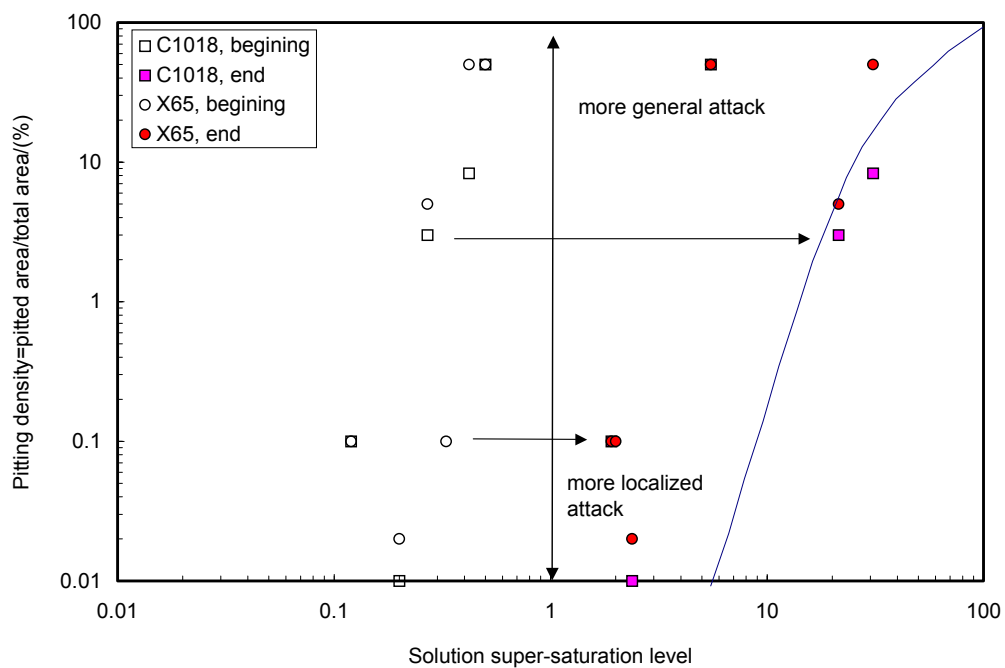


Figure 6.4 The magnified display of Figure 6.3 around the saturation line.

Figure 6.2 shows one way to present localized corrosion by use of the pitting factor. The pitting factor f is redefined as the ratio of the difference between maximum penetration rate and average corrosion rate to the average corrosion rate, which is different from equation (4-7) and illustrated as follows:

$$f = \frac{CR_{\max} - CR_{\text{aver}}}{CR_{\text{aver}}} \quad (6-4)$$

A pitting factor of zero suggests no localized corrosion, while any number above zero indicated the occurrence of localized attack. It is interesting to observe that localized corrosion took place whenever the solution started under saturated and ended up mildly supersaturated. All of the localized corrosion showed a pitting factor less than ten in the experiments. There are two groups of data points, indicated by small arrows in Figure 6.2: when both the beginning and the end of experimental points are either well below the saturation point or well above the saturation point, there was no localized corrosion with a pitting factor of zero. These data represent the 40°C tests and 90°C high pH 6.2 tests, respectively. Both cases interpret the two extreme conditions: either no film was formed or a fully protective film was formed. Thus, the three scenarios in CO₂ corrosion proposed in Figure 6.1 are identifiable in Figure 6.2. The onset of localized attack can then be well correlated with the solution super-saturation level.

In addition, a solid line can be seen in Figure 6.2. This line envelopes a range within which localized corrosion can occur. It also shows that the pitting factor is getting bigger when the super saturation is closer to 1, leading to the poorest protection offered by precipitating film.

Figure 6.3 presents another way to describe the localized corrosion by pitting density, which has been defined in section 5.3 to describe the effect of Cl^- ions on localized corrosion. A pitting density of zero expresses no localized corrosion, while any value above zero indicates the occurrence of localized attack. It is seen that most of the localized attack has the pitting density less than 10% of the total area, which illustrates that the localized attack is genuinely a local phenomena. There are a couple of points with 50% pitting density, which suggests that the localized attack tends to be widespread, suggesting a universally uneven attack.

Figure 6.4 is the magnified display of those points around the saturation line in Figure 6.3. The solid line envelopes a range within which localized corrosion can occur. It also shows that the pitting density gets smaller when the super saturation level is closer to 1, which suggests that the localized corrosion tends to be more “local,” and deeper (see Figure 6.2).

Therefore, the super-saturation level is crucial for localized corrosion from two perspectives: magnitude and density. Close to the saturation point, the material tends to be locally and highly attacked.

Thus the super saturation model for localized corrosion can be summarized:

If $SS \ll 1$ or $SS \gg 1$	uniform corrosion
If $SS \approx 1-3$	localized corrosion possible

6.3 Scaling Tendency (ST) And Localized Corrosion

van Hunnik (1996) and Pots (2000) proposed a “scaling tendency” (ST) concept to describe a protective film formation. It is defined as follows:

$$ST = \frac{PR}{CR} \quad (6-5)$$

where, PR is the iron carbonate precipitation rate and CR is the corrosion rate expressed in the same units. They also found when $ST > \sim 0.5$, a protective film is considered to form. According to the experimental findings in this research, localized corrosion occurred when a non-protective film formed. Therefore, using the same concept, the corrosion rate (initial CR) experimentally measured in mm/yr was compared to the precipitation rate in mm/yr, which was calculated by the following equation:

$$[Fe^{2+}]_{prec} = k_r K_{sp} (SS - 1)(1 - SS^{-1}) \quad (6-6)$$

The physical meaning of each item in above equation has been introduced in equation (2-11).

Notice that the prerequisite for the scale formation is a super-saturated solution. Any under-saturated solution will not lead to film formation, and the scaling tendency should be zero. The result is shown in Figure 6.5 by taking the pitting factor as an example. The pitting factor seems large around a scaling tendency of 1, which corresponds to poorly protective films.

According to Figure 6.5, the scaling tendency model for localized corrosion can be summarized as:

If $ST \gg 3$ or $ST \ll 0.3$	uniform corrosion
If $0.3 < ST < 3$	localized corrosion possible

Hence, the risk of localized corrosion can be predicted through either solution super-saturation level or the scaling tendency.

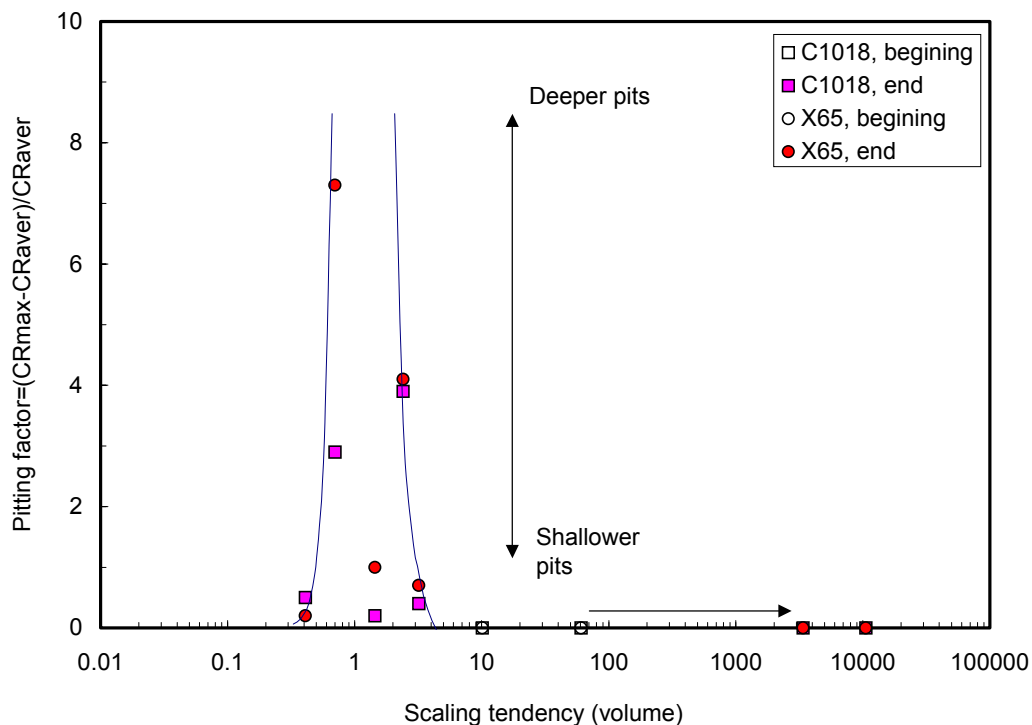


Figure 6.5 The relationship between the scaling tendency and pitting factor for all the experiments.

Since the species concentrations all refer to the bulk water concentration, the above approach can only be applied to the bottom of the line corrosion when the flow is in stratified regime. For top of the line in stratified flow, the Vitse (2002) top of the line corrosion model is recommended to obtain the water chemistry on the top, and then the same principle should apply. In annular flow, the present approach is valid for both the top and the bottom because they have the same water chemistry.

CHAPTER 7: CONCLUSIONS AND RECOMMENDATIONS

7.1 Conclusions

Wet gas corrosion, particularly localized corrosion, has been investigated in a full-scale horizontal pipeline with the presence of a small amount of liquid under natural condensation conditions. Through various corrosion monitoring techniques and surface analysis techniques, the corrosion behavior of two carbon steels has been systematically studied over a large variety of corrosive environments under stratified flow and annular flow conditions. A physico-chemical model has been abstracted to explain the likelihood of localized corrosion for the first time. Based on the test matrix, the research findings through both the experimental work and modeling work include:

Localized corrosion took place only when partially protective films were formed. Under film-free conditions or formation of fully protective films, only uniform corrosion was observed.

Temperature affects the corrosion product film formation and thus localized corrosion. At 40°C, no localized corrosion occurred, and no iron carbonate corrosion product films were formed. At 90°C, corrosion product films can vary significantly: fully protective films resulted in no localized corrosion while partially protective films caused localized attack.

The CO₂ partial pressure played totally different roles with respect to the formation of corrosion product films. Under film-free conditions, uniform corrosion rate increased with the increase in CO₂ partial pressure. With the formation of fully protective

films, the corrosion rate was unresponsive to the change of CO₂ partial pressure within a large range. With partially protective films, the increase in CO₂ partial pressure might have facilitated the formation of more protective films and resulted in less localized attack in both magnitude and pitting density.

Localized corrosion was observed under both Cl⁻ free and Cl⁻ containing solutions. The Cl⁻ concentration affected the localized corrosion through pitting density.

Solution pH was critical to localized corrosion. A pH of 6.2 can inhibit the localized corrosion from occurrence, while a pH (4.5 ~6.0) may trigger localized attack.

The presence of a small amount of hydrocarbon phase exhibited a favorable effect on both uniform and localized corrosion even in non-inhibited environments, allowing acceptable gas flow rates when annular flow was maintained.

The higher gas and liquid flow rate resulted in higher corrosion rates and a higher pitting density when localized corrosion occurred.

Higher pressure, higher gas, and liquid flow rates caused the change of flow regime to annular flow. The corrosion behavior at the top approached that of the bottom when annular flow was maintained. However, stratified flow showed a difference between the corrosion behavior on the bottom and the top. The top of line may suffer localized corrosion as well under high CO₂ partial pressure environment.

X65 was somewhat more resistant to localized corrosion than C1018 in general. However, no systematic advantage of one over the other was observed.

A solution super saturation level and scaling tendency can be used to describe the likelihood of localized corrosion. It was found that localized corrosion took place when

the bulk solution is only slightly above the saturation point or when the bulk scaling tendency was between 0.3 and 3.0.

7.2 Recommendations

Some suggestions for the future work to refine and extend the current research are as follows:

Experiments under controlled pH with different CO₂ partial pressures under film forming conditions. This will help identify whether CO₂ partial pressures can facilitate the formation of corrosion product films and increase the protectiveness. A pH of 5.0 to 5.5 is recommended.

Experiments under controlled pH with different gas flow rates. This will help identify the critical velocity below which localized corrosion would not occur. A pH of 5.2 and 3 m/s V_{sg} are recommended to complement the current research.

Experiments with a small super-saturation solution (SS is just a little bigger than 1) and small under-saturated solution (SS is a little less than 1). This will help to refine the super saturation and scaling tendency models for localized corrosion.

Experiments with acetic acid to identify the effect of acetic acid on localized corrosion.

Experiments with inhibitors to evaluate how effective the inhibitor is to stop localized corrosion.

Develop an electrochemical technique to study the localized corrosion *in situ*.

Develop a 2D/3D mechanistic model to predict the localized corrosion.

REFERENCES

1. Al-Hassan, S., Mishra, B., Olson, D.L., and Salama, M.M., "Effect of Microstructure on Corrosion of Steels in Aqueous Solutions Containing Carbon Dioxide," *Corrosion*, Vol.54, No.6, 1998, p.480.
2. Bhongale, S., "Effect of Pressure, Temperature, and Froude Number on Corrosion Rates in Horizontal Multiphase Slug Flow," Master's thesis, Ohio University, 1995.
3. Brossia, C.S. and Cragolino, G.A., "Effect of Environmental Variables on Localized Corrosion of Carbon Steel," *Corrosion*, Vol.56, No.5, 2000, p.505.
4. Crolet, J.L., Thevenot, N., and Nestic, S., "Role of Conductive Corrosion Products in the Protectiveness of Corrosion Layers," *Corrosion*, Vol.54, No.3, 1998, p.194.
5. Dayalan, E., de Moraes, F.D., Shadley, J.R., Shirazi, S.A., and Ribicki, E.F., *Corrosion/98*, paper no.51, (Houston, TX: NACE International, 1998).
6. Daniels, F, and Alberty, R.A., *Physical Chemistry*, 3rd edition, John Wiley & Sons, Inc., New York, 1996.
7. de Moraes, F., Shadley, J.R., Chen, J., "Characterization of CO₂ Corrosion Product Scales Related to Environmental Conditions," *Corrosion/2000*, Paper No.30.
8. de Waard, C., and Milliams, D.E., "Carbonic Acid Corrosion of Steel," *Corrosion*, 31, No.5, P.197, 1975.
9. de Waard, C., Lotz, U., and Milliams, D. E., "Predictive Model for CO₂ Corrosion Engineering in Wet Natural Gas Pipelines," *Corrosion*, 47, No.12, p.976, 1991.

10. de Waard, C., Lotz, U., "Prediction of CO₂ Corrosion of Carbon Steel," Corrosion/93, paper no. 69, (NACE international, Houston, TX: 1993).
11. de Waard, C., Lotz, U., and Dugstad, A., "Influence of Liquid Flow Velocity on CO₂ Corrosion: A Semi-Empirical Model," Corrosion/95, paper no.128, (NACE international, Houston, TX: 1995)
12. Dugstad, A., Hemmer, H., and Seiersten, M., "Effect of Steel Microstructure on Corrosion Rate and Protective Iron Carbonate Film Formation," *Corrosion*, Vol.57, No.4, 2001, p.369.
13. Dugstad, A, Lunde, L., and Videm, K., "Parametric Study of CO₂ Corrosion of Carbon Steel," Corrosion/94, Paper No.14.
14. Dugstad, A., " The Importance of FeCO₃ Supersaturation on the CO₂ Corrosion of Carbon Steels," Corrosion/92, Paper No.14.
15. Fu, S-L, Bluth, M.J., " Study of Sweet Corrosion under Flowing Brine and/or Hydrocarbon Conditions," Corrosion/94, Paper No.31.
16. Gunaltun, Y. M., "Combining Research and Filed Data for Corrosion Rate Prediction" Corrosion/1996, paper no.27, (Houston, TX: NACE International, 1996).
17. Gunaltun, Y.M., "Corrosion in Oil and Gas Production Systems," 1997.
18. Gunaltun, Y.M., Private Communication, 2001.

19. Gunaltun, Y.M. and Belghazi, A., "Control of Top of Line Corrosion by Chemical Treatment," Corrosion/2001, paper no. 33, (Houston, TX: NACE International, 2001).
20. Gunaltun, Y.M., Supriyatman, D., Achmad, J., "Top of line corrosion in multiphase gas lines, A case history," Corrosion/99, Paper No. 36.
21. Gunaltun, Y. M., and Larrey D, "Correlation of cases of top of line corrosion with calculated water condensation rates," Corrosion/2000. Paper No.71.
22. Hara, T., Asahi, H., Suehiro, Y., and Kaneta, H., "Effect of Flow Velocity on Carbon Dioxide Corrosion Behavior in Oil and Gas Environments," Corrosion, Vol.56, No.8, 2000, p.861.
23. Heuer, J.K., Stubbins, J.F., "Microstructure Analysis of Coupons Exposed to Carbon Dioxide Corrosion in Multiphase Flow". Corrosion, 54, No.7, p.566, NACE, 1998.
24. Heuer, J.K., Stubbins, J.F., "An XPS Characterization of FeCO₃ films from CO₂ Corrosion," Corrosion Science, 41, No.7, 2000.
25. Hong, T., Advisory Board Meeting, NSF I/UCRC Corrosion In Multiphase System Center, Ohio University, October, 2000.
26. Ikeda, A., Ueda, M., and Mukai, S., "CO₂ behavior of Carbon and Cr Steels," in Advances in CO₂ corrosion, Vol.1 (Houston, TX: NACE, 1984), p.52.
27. Jasinski, R., *Corrosion*, 43, No.4, P.214, 1986.
28. Jones, D.A, *Principles and Prevention of Corrosion*, 2nd edition, Englewood Cliffs, NJ : Prentice Hall ; London : Prentice-Hall International, 1996.

29. Kapusta, S.D., Pots, B.F.M., and Connell, R.A., "Corrosion Management of Wet Gas Pipelines," *Corrosion/99*, paper no.45, (Houston, TX: NACE international, 1999).
30. Kermani, M.B., and Smith, L.M., "A Working Party Report on 'CO₂ Corrosion Control in Oil and Gas Production' Design Considerations", European Federation of Corrosion Publication, No.23, The Institute of Materials, 1997.
31. Lee, A-H., Sun, J-Y, and Jepson, W.P., "Study of Flow Regime Transitions of Oil-Water-Gas Mixtures in Horizontal Pipeline", Proceedings of the Third International Offshore and Polar Engineering Conference, Singapore, Vol. II, 1993, pp.159-164, Publ. International Society of Offshore and Polar Engineers (ISOPE), Golden, CO, 1993.
32. Lide, D., *CRC Handbook of Chemistry and Physics*, 79th edition, 1998-1999.
33. Netic, S. and Lunde, L., "Carbon Dioxide Corrosion of Carbon Steel in Two-phase Flow," *Corrosion*, Vol.50, No.9, 1994, p.717.
34. Netic, S., Postlethwaite, J., and Olsen, S., *Corrosion*, 52 (4), (1996): p.280.
35. Netic, S., Nordsveen, M., Nyborg, R., and Stangeland, A., "A Mechanistic Model for CO₂ Corrosion with Protective Iron Carbonate Films," *Corrosion/2001*, paper no.40, (Houston, TX: NACE International, 2001).
36. Netic, S., Lee, K-L. J., and Ruzic, V., "A Mechanistic Model of Iron Carbonate Film Growth And The Effect on CO₂ Corrosion of Mild Steel," *Corrosion/2002*, paper no.02237, (Houston, TX: NACE International, 2002).

37. Nyborg, R., "Initiation and Growth of Mesa Corrosion Attack During CO₂ Corrosion of Carbon Steel," Corrosion/98, paper no.48, (Houston, TX: NACE International, 1998).
38. Nyborg, R., "Overview of CO₂ Corrosion Models for Wells and Pipelines," Corrosion/2002, paper no.02233, (Houston, TX: NACE International, 2002).
39. Olsen, S. and Dugstad, A., "Corrosion under dewing conditions," Corrosion/91, Paper No. 472.
40. Palacios, C.A and Shadley, J.R., " Characteristics of Corrosion Scales on Steels in a CO₂-saturated NaCl Brine," Corrosion, 47, No.2, P.122, NACE, 1991.
41. Pots, B.F.M., "Mechanistic Models for the Prediction of CO₂ Corrosion Rates under Multi-Phase Flow Conditions," Corrosion/95, paper no.137, (Houston, TX: NACE international, 1995).
42. Pots, B.F.M, and Hendriksen, E.L.J.A. "CO₂ Corrosion Under Scaling Conditions- The Special Case of Top-Of-Line Corrosion in Wet Gas Pipelines," Corrosion/2000, paper no.31, (Houston, TX: NACE International, 2000).
43. Schmitt, G., Mueller, M., Papenfuls, M., "Understanding Localized CO₂ Corrosion of Carbon Steel from Physical Properties of Iron Carbonate Scales," Corrosion/99, Paper No. 38, (Houston, TX: NACE International, 2002).
44. Schmitt, G. and Feinen, S., "Effect of Anions and Cations on The Pit Initiation in CO₂ Corrosion of Iron and Steel," Corrosion/2000, paper no., (Houston, TX: NACE International, 2000).

45. Schmitt, G., Guddle, T., Strobel-Effertz, E., "Fracture Mechanical Properties of CO₂ Corrosion Product Scales and Their Relation to Localized Corrosion," Corrosion/96, Paper No.9, (Houston, TX: NACE International, 1996).
46. Schmitt, G., Bosch, C., and Mueller, M., "A Probabilistic Model for Flow Induced Localized Corrosion," Corrosion/2000, Paper No. 49, (Houston, TX: NACE International, 2000).
47. Schmitt, G., Mueller, M., "Critical Wall Shear Stresses in CO₂ Corrosion of Carbon Steel," Corrosion/99, Paper No.44, (Houston, TX: NACE International, 1999).
48. Shi, H., "A Study of Oil-Water Flows in Large Diameter Horizontal Pipelines," Dissertation, Ohio University, 2001.
49. Smith, G.C., *Surface Analysis by Electron Spectroscopy*, Plenum press, New York and London, 1995, p.5.
50. Sun, Y.H., Advisory Board Meeting, NSF I/UCRC Corrosion In Multiphase System Center, Ohio University, October, 2001.
51. van Hunnkik, E. W. J., Pots, B.F.M., and Hendriksen, E.L.J.A, "The Formation of Protective FeCO₃ Corrosion Product Layers in CO₂ Corrosion," Corrosion/96, paper no.6, (Houston, TX: NACE International, 1996).
52. Vedapuri, D., Kang, C., Dhanabalan, D. and Gopal, M., Corrosion/2000, Paper No. 43.
53. Vitse, F., "Experimental and Theoretical Study of the Phenomena of Corrosion by Carbon Dioxide under Dewing Conditions at the Top of A Horizontal Pipeline in the Presence of Non-Condensable Gas," Dissertation, Ohio University, 2002.

54. Vuppu, A.K., and Jepson, W.P., "Study of Sweet Corrosion in Horizontal Multiphase Carbon Steel Pipelines," Offshore Technology Conference, 1993.
55. Wang, H.W., "CO₂ Corrosion Mechanistic Modeling in Horizontal Slug Flow," Dissertation, Ohio University, 2001.
56. Wang, H.B., "The Study of Corrosion Product and Inhibitor Films in Multiphase Flow," Dissertation, Ohio University, 2001.
57. Xia, Z., Chou, K.C., and Szklarska-Smialowska, Z., "Pitting Corrosion of Carbon Steel in CO₂-Containing NaCl Brine," Corrosion, Vol.45, No.8, p.636,1989.
58. Zhang, R.L., "Mechanistic Modeling of Sweet Corrosion in Horizontal Pipes," Master's Thesis, Ohio University, 1997.

**APPENDIX A: SPECIMEN ETCHING PROCEDURE FOR
MICROSTRUCTURE IDENTIFICATION**

(Summarized from ASTM standard E407—Standard Test Method for Microetching Metals and Alloys)

1. Preparation of the etchant. The etchant composition is 1-5 mL HNO₃ (20 drops/mL) and 100 mL ethanol (95%) or methanol (95%).
2. Preparation of the specimen. They should be freshly polished (see surface treatment of specimen).
3. Immerse the specimen into the etchant for a few seconds to a minute; gentle agitations during etching for more uniform etch.
4. Remove all traces of the etchant by thorough washing (can use D.I. water in order to stop the etching process) and complete drying (can use alcohol) of the specimen before placing it on microscope stage.
5. Place the etched specimen under metallurgical microscope to observe the microstructure and take pictures.

APPENDIX B: EXPERIMENTAL UNCERTAINTY ANALYSIS

B.1 Uncertainty of The Corrosion Rate Measurement Due to The Type of Instrumentation

Various instruments were employed during the experiments to measure the different types of corrosion rate. For instance, the dial box (a data acquisition equipment) was used for uniform corrosion monitoring with ER method; the electrical balance was used for WL measurements with average corrosion rate; the metallurgical microscope was adopted to measure the localized corrosion rate; and the Gamry[®] data acquisition system was used to monitor the instantaneous corrosion rate by LPR. Thus the error introduced by different instruments varied accordingly.

ER Measurements for Uniform Corrosion Rate.

The instrumentation used to measure the corrosion rate was a portable corrosometer (which is often called a “dial box”) as described in Chapter 4. Readings were taken using the dial that has 0-1000 digits representing 0-100% of probe life. The resolution of the instrumentation is 0.5 digits. According to Metal Samples (<http://www.alspi.com>), for a S-5 probe, it has an element thickness of 5 mils and effective probe life of 2.5 mils. This means that the minimum measurable change for the probe is $\frac{2.5 \times 0.5}{1000} \times \frac{1}{1000} \times 2.54 \times 10 = 3.175 \times 10^{-5} \text{ mm}$. In the experiments using this type of probe (which generally had low corrosion rates), the lowest stabilized corrosion rate measured was above 0.02 mm/yr for 150 hours. Thus the minimum metal loss measured

during the experiment was around $\frac{0.02}{365 \times 24} \times 150 = 3.425 \times 10^{-4} \text{ mm}$. Thus the relative

error ε due to the sensitivity of the dial box is:

$$\varepsilon_1 = \frac{3.175 \times 10^{-5}}{3.425 \times 10^{-4}} = 9.3\% \quad (\text{B-1})$$

Very often, the ER measurements were integrated with time to give an average value during the entire experiment. The lowest average corrosion rate using this type of probe was 0.02 mm/yr for 200 hours. Thus the relative error in this case would be

$$\varepsilon_2 = \frac{3.175 \times 10^{-5}}{\frac{0.02}{365 \times 24} \times 200} = 7.0\% \quad (\text{B-2})$$

The temperature and pressure effects on the measurement were unknown and not provided by Metal Samples. But it is estimated that the error due to this two parameters would be smaller than the resolution of the dial box.

From above analysis, one can understand that the relative error due to the dial box would change with the experiments and the way data was presented. It is also related to the test duration, probe size, and the actual corrosion rate. The example given above represents the highest error and the errors in all the other experiments were smaller than 9.3%.

Weight Loss Measurements for Average Corrosion Rate.

The digital balance was employed to weigh the specimen before and after the test (after removal of corrosion product film). The minimum reading on the balance is 0.0001 gram. The minimum metal loss during the experiment was 0.0082 gram, thus the relative error due to the sensitivity of the electrical balance was 1.2%. Once again, the smaller

weight loss (which means the lower corrosion rate) would cause larger errors due to the instrumentation. For every measurement, the error would be different according to the corrosion rate. However, they are all less than 1.2%.

MM Measurements for Localized Corrosion Rate.

A metallurgical microscope was used to measure the localized corrosion rate by rotating the fine focus knob. The minimum reading of the scale on the knob is 1 μm , which means the minimum measurable change in depth is 1 μm . The lowest localized penetration depth experimentally measured was 16 μm . Thus the relative error due to this instrumentation is 6.25%. The same as all the other instruments, the error depends on the corrosion rate. However, 6.25% is the highest error among all the experiments due to the use of metallurgical microscope.

B.2 Uncertainty of The Corrosion Rate Measurements Due to The Measurement Technique

ER Technique.

Essentially, the ER technique is to obtain the corrosion rate through the resistance change of a probe element, which relates to the loss of the element thickness. The sensing element of an ER probe can be represented in Figure B.1 .

The electrical resistance of the sensing element is given by:

$$R = \frac{\rho \times L}{h \times \delta} \quad (\text{B-3})$$

where, R is the electrical resistance (Ohm), ρ is the electrical resistivity (Ohm.m), L is the sensor length (m), h is the sensor thickness (m), and δ is the sensor width (m).

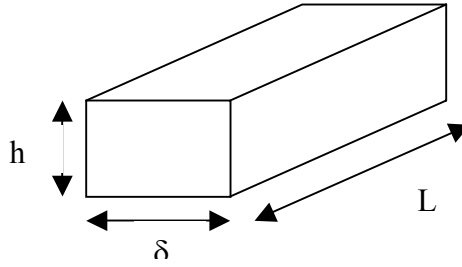


Figure B.1 ER sensing element.

The corrosion rate is obtained from the metal loss:

$$CR = 1000 \times \frac{\Delta h}{\Delta t} \quad (\text{B-4})$$

CR is expressed in mm/yr, and the time interval Δt is expressed in years. Combining equation (B-3) and (B-4), one obtains:

$$CR = \frac{1000 \times L}{\Delta t \times \delta} \times \Delta \left(\frac{\rho}{R} \right) \quad (\text{B-5})$$

The resistivity and the resistance are dependent on temperature. The other system variables, such as pressure, pH, flow, solution composition, do not affect these two variables in a significant manner. L and δ are not significantly affected by the change of temperature (linear expansion coefficient of CS 1020 is around $1.17 \times 10^{-5}/^{\circ}\text{C}$ (Lide, 1998-1999)) or other system parameters. Thus the absolute uncertainty in the measurement of the corrosion rate as a result of uncertainties in the system variables can be expressed as follow:

$$\frac{\delta(CR)}{CR} = \left[\frac{\partial(CR)}{\partial T} \right] \frac{\delta T}{CR} \quad (\text{B-6})$$

According to equation (B-5):

$$\frac{\delta(CR)}{CR} = 2 \times \left[\frac{\partial(CR)}{\partial \rho} \times \frac{\partial(\rho)}{\partial T} + \frac{\partial(CR)}{\partial R} \times \frac{\partial(R)}{\partial T} \right] \frac{\delta T}{CR} \quad (B-7)$$

The dependence of ρ on T , and R on T ($^{\circ}\text{K}$) are obtained from the literature (Vitse, 2002, Lide, 1998-1999):

$$\rho = 6.01 \times 10^{-10} \times T - 7.97 \times 10^{-8} \quad (B-8)$$

$$\frac{1}{R} \frac{\partial R}{\partial T} = 0.004 \quad (B-9)$$

According to equation (B-5):

$$\frac{\partial(CR)}{\partial \rho} = \frac{1000 \times L}{\Delta t \times \delta \times R} \quad (B-10)$$

$$\frac{\partial(CR)}{\partial R} = \frac{1000 \times L \times \rho}{\Delta t \times \delta} \times \left(-\frac{1}{R^2} \right) \quad (B-11)$$

Substitute equations (B-8) through (B-11) into equation (B-7) and simplified, one can finally obtain the following equation:

$$\frac{\delta(CR)}{CR} = \frac{2000 \times h}{\Delta t} \times \left(\frac{6.01 \times 10^{-10}}{6.01 \times 10^{-10} \times T - 7.97 \times 10^{-8}} - 0.004 \right) \times \frac{\delta T}{CR} \quad (B-12)$$

During the experiment, the temperature variation was $\pm 2^{\circ}\text{C}$, the element thickness for a S-5 probe is 5 mils, which is equivalent to 1.27×10^{-4} mm. Therefore,

$$\frac{\delta(CR)}{CR} = \pm \frac{0.508}{\Delta t \times CR} \times \left(\frac{6.01 \times 10^{-10}}{6.01 \times 10^{-10} \times T - 7.97 \times 10^{-8}} - 0.004 \right) \quad (B-13)$$

For a 200 hours experiment at 90°C with corrosion rate of 0.02 mm/yr, the relative error on the corrosion rate is 37.9%. This will change with each experiment according to the corrosion rate, test duration, probe type etc.

LPR technique.

The factors that affect the accuracy of the LPR corrosion rate measurement include temperature, applied current, applied potential, and the working electrode area. According to Chapter 4, the corrosion rate can be written as:

$$CR = 3.27i_{corr} \frac{E}{D} = 11.63i_{corr} \quad (\text{B-14})$$

where corrosion rate (CR) is expressed in mm/yr, and i_{corr} is in $\mu\text{A}/\text{cm}^2$. Equation (4-4) expressed the current density as:

$$i_{corr} = \frac{\beta_a \beta_c}{2.303(\beta_a + \beta_c)} \times \frac{1}{R_p} \quad (\text{B-15})$$

Substituting (B-15) into (B-14) yields:

$$CR = 5.05 \frac{\beta_a \beta_c}{\beta_a + \beta_c} \times \frac{1}{R_p} \quad (\text{B-16})$$

where, the anodic and cathodic Tafel constants β_a and β_c (in V) are the function of temperature. They can be expressed as:

$$\beta_a = \frac{2.303RT}{\alpha_a nF} \quad (\text{B-17})$$

$$\beta_c = \frac{2.303RT}{\alpha_c nF} \quad (\text{B-18})$$

where,

T is the absolute temperature in K. R is the universal gas constant as 8.314 J/mol K. α_a and α_c are the symmetry factors for anodic and cathodic reaction. The values of α are typically close to 0.5. n is the number of electrons exchanged in the reaction in mole. F is Farady's constant as 96,500 coulombs/equivalent.

Since β_a and β_c are only dependent on temperature and vary linearly with temperature, they can be rewritten as the following equations:

$$\beta_a = \beta_{a0} + m_1 T \quad (\text{B-19})$$

$$\beta_c = \beta_{c0} + m_2 T \quad (\text{B-20})$$

where β_{a0} and β_{c0} are the base anodic and cathodic Tafel constant at a suitable reference temperature. The slope m_1 and m_2 can be easily obtained by plotting equation (B-17) and (B-18). The values are $m_1 = 0.2$ mV/K and $m_2 = -0.2$ mV/K separately (Rihan, 2001).

In equation (B-16), R_p can be expressed as follows:

$$R_p = \frac{dE}{di_{app}} \quad (\text{B-21})$$

where, i_{app} is the applied current density in A/cm².

$$i_{app} = \frac{I_{app}}{a} \quad (\text{B-22})$$

where, I_{app} is the applied current in A, and a is the working electrode area in cm².

Substitute equation (B-19) through (B-22) into equation (B-16) yields:

$$CR = 5.05 \frac{(\beta_{a0} + m_1 T)(\beta_{c0} + m_2 T)}{\beta_{a0} + \beta_{c0} + (m_1 + m_2)T} \times \frac{\Delta I_{app}}{\Delta E \Delta a} \quad (\text{B-23})$$

Which can then be written in the following form:

$$CR = 5.05 (\beta_{a0} + m_1 T) (\beta_{c0} + m_2 T) [\beta_{a0} + \beta_{c0} + (m_1 + m_2)T]^{-1} (\Delta E)^{-1} (\Delta I) (\Delta a)^{-1} \quad (\text{B-24})$$

The sensitivity of small changes in the corrosion rate to small changes in each variable is expressed by taking the partial derivatives of the corrosion rate with respect to each variable. The errors in β_{a0} , β_{c0} , m_1 , and m_2 are assumed to be negligible. Thus, the

absolute uncertainty in the measurement of the corrosion rate as a result of uncertainties in the system variables can be expressed as follows:

$$\frac{\delta(CR)}{CR} = \left[\frac{\partial(CR)}{\partial T} \right] \frac{\delta T}{CR} + 2 \left[\frac{\partial(CR)}{\partial E} \right] \frac{\delta E}{CR} + 2 \left[\frac{\partial(CR)}{\partial I_{app}} \right] \frac{\delta I_{app}}{CR} + 2 \left[\frac{\partial(CR)}{\partial a} \right] \frac{\delta a}{CR} \quad (B-25)$$

Derive the partial derivatives of each item above according to equation (B-24) and then substitute into (B-25), the following equation can be eventually derived:

$$\frac{\delta(CR)}{CR} = \left(\frac{m_1}{\beta_a} + \frac{m_2}{\beta_c} \right) \delta T - \frac{2}{E} \delta E + \frac{2}{I_{app}} \delta I_{app} - \frac{2}{a} \delta a \quad (B-26)$$

Therefore, the corrosion rate uncertainty above can be considered to be an overall uncertainty through the experiment for LPR technique. It considers the uncertainties due to environmental parameter (temperature), due to the instrumentation and the technique (potential and applied current), and due to the working electrode surface area. The contribution of each item in (B-26) to the corrosion rate uncertainty measurements is discussed as follows:

Temperature

The temperature during the experiment was maintained at $90^\circ\text{C} \pm 2^\circ\text{C}$, thus $\delta T = 2$. Since the LPR technique was only applied during the 90°C experiments, $\beta_a = 48.7$ mV and $\beta_c = 143.7$ mV were used. Thus the first item on the right side of (B-26) is:

$$\left(\frac{m_1}{\beta_a} + \frac{m_2}{\beta_c} \right) \delta T = \left(\frac{0.2}{48.7} + \frac{-0.2}{143.7} \right) \times 2 = 5.43 \times 10^{-3} \quad (B-27)$$

Potential

According to Gamry, the DC accuracy in voltage measurement is $\pm 0.3\%$ range ± 1 mV. During the experiment, the applied potential was ± 5 mV over the open circuit

potential. Thus the uncertainty in the potential would be $\delta E = 1.03mV$. The second item determination in equation (B-26) is different for the measurements before and after corrosion product film formation. Before the corrosion product film formation, the R_p was determined over the entire applied potential since it agreed with the linear relationship between the potential and current, as shown in Figure B.2. Thus the applied range and the actual range used to analyze the R_p are the same as 10 mV. The absolute uncertainty of the second item in equation (B-26) can be described as:

$$\frac{2}{E} \delta E = \frac{2}{10} \times 1.03 = 0.206 \quad (\text{B-28})$$

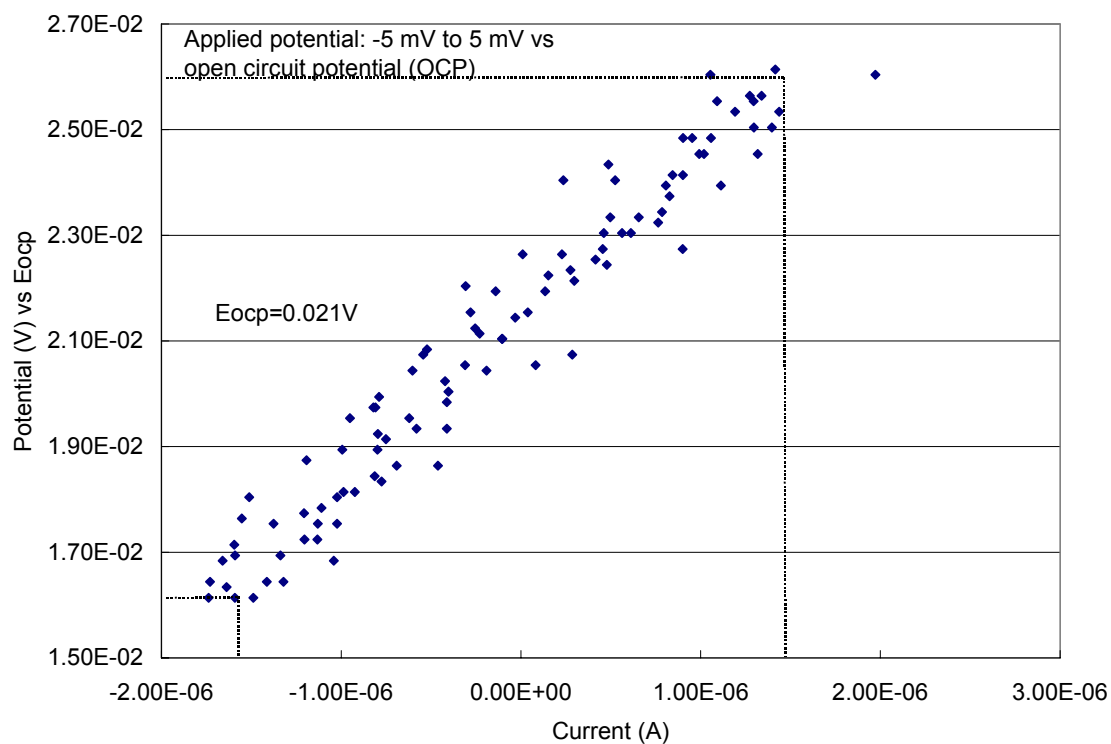


Figure B.2 A typical linear polarization curve obtained in experiments before film formation.

However, this was changed after the corrosion product film formation on the electrode surface since the linear relationship did not exist over the entire applied potential, as indicated in Figure B.3. The actual potential used to get the R_p was only taken from the linear region, which was in a 6 mV range. Thus the absolute uncertainty after the film formation is:

$$\frac{2}{E} \delta E = \frac{2}{6} \times 1.03 = 0.343 \quad (\text{B-29})$$

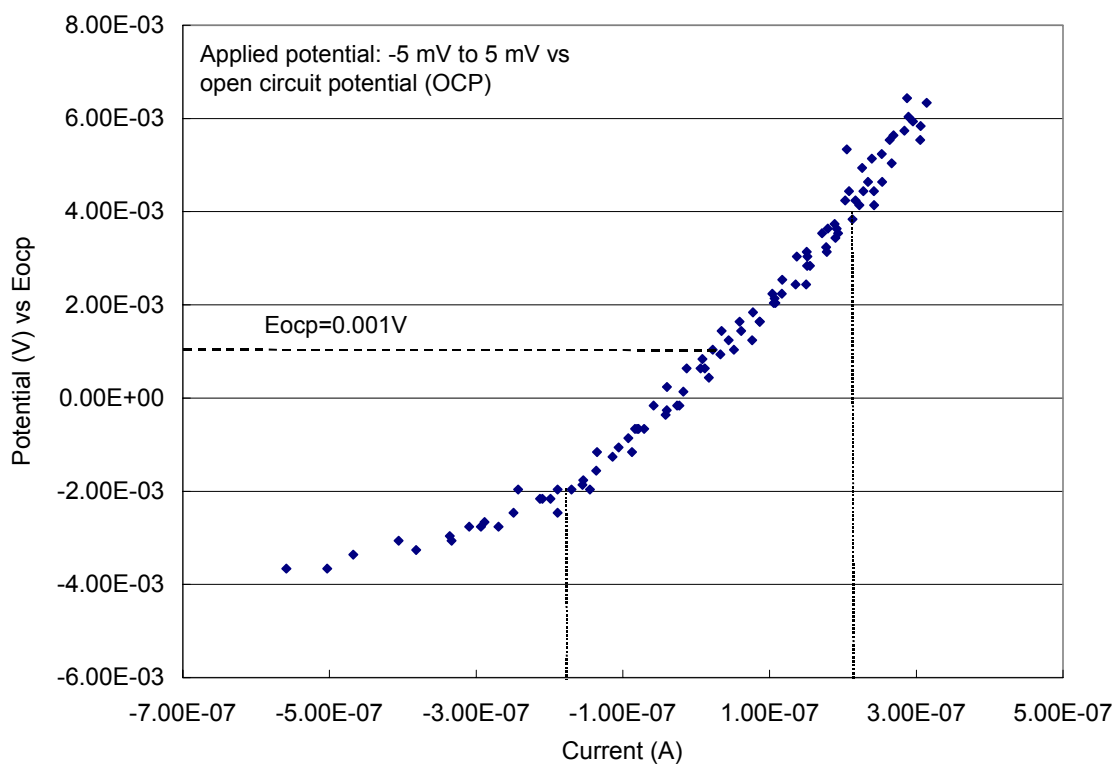


Figure B.3 A typical non-linear polarization curve obtained in experiments after film formation.

Since most of the time the LPR data was presented as a time averaged value, the error due to the potential measurement should be somewhere in between with and without film formation.

Current

According to Gamry, the DC accuracy in current measurement is $\pm 0.3\%$ range ± 50 pA. The current range varied from experiment to experiment, it also varied from the beginning to the end during one experiment because of the change in corrosion rate. Take the same experiment as an example as discussed in the potential section, before film formation (Figure B.2), the actual measured current is the same as the applied current range, which was $3.0e-06$ A. Thus the uncertainty in the current was $\delta I_{app} = 9 \times 10^{-9}$ A.

The absolute uncertainty of the third item in equation (B-26) can be described as:

$$\frac{2}{I_{app}} \delta I_{app} = \frac{2}{3.0e-06} \times 9 \times 10^{-9} = 6.0 \times 10^{-3} \quad (\text{B-30})$$

After the film formation (Figure B.3), the applied current was $8.9E-07$ A, while the actual measured current was $4.0E-07$ A. Thus the uncertainty in the current was $\delta I_{app} = 8.9 \times 10^{-7} \times 0.3\% + 50 \times 10^{-12} = 2.72 \times 10^{-10}$ A. The absolute uncertainty of the third item in equation (B-26) after the film formation can be expressed as:

$$\frac{2}{I_{app}} \delta I_{app} = \frac{2}{4.0e-07} \times 2.72 \times 10^{-10} = 1.36 \times 10^{-3} \quad (\text{B-31})$$

If the time averaged corrosion rate was used, then the error should be somewhere in between (B-30) and (B-31).

Electrode Area

The uncertainty of the area was estimated to be 0.003 cm². The total working electrode surface area was 0.95 cm². Therefore, the absolute uncertainty for the fourth item on the right side of equation (B-26) is:

$$\frac{2}{a}\delta a = \frac{2}{0.95} \times 0.003 = 6.32 \times 10^{-3} \quad (\text{B-32})$$

Thus the uncertainties on the corrosion rate measurement from LPR technique for the given specified experiment is expressed as:

$$\frac{\delta(CR)}{CR} = \pm \left(5.43 \times 10^{-3} - \frac{0.206 + 0.343}{2} + \frac{6.0 \times 10^{-3} + 1.36 \times 10^{-3}}{2} - 6.32 \times 10^{-3} \right) = \pm 27.2\%$$

From above equation, one can conclude that in the LPR measurement, the uncertainty in the potential is the major source for the error in corrosion rate.

B.3 Overall Uncertainty On The Corrosion Rate Measurements

ER Technique.

The total uncertainty on the corrosion rate measurements for ER technique should include two sources: one was from the instrumentation (dial box) or data acquisition system; another was from the technique itself based on the metal loss theory. Thus for the given experiment example in B.1 and B.2, the overall uncertainty for the ER measurement should be: 7.0%+37.9% = 44.9%. This number would vary according to the different experiment.

LPR Technique.

The method introduced in B.2 for the LPR technique has included various sources, from the environmental factor to the data acquisition system, as well as to the probe that was actually exposed to the test environment. Thus it can be considered as an overall uncertainty for this technique.